Design and Analysis of Axial Aspirated Compressor Stages

by

Ali A. Merchant

B.S., University of Tennessee, Knoxville (1994)
S.M., Massachusetts Institute of Technology (1996)

Submitted to the
Department of Aeronautics and Astronautics
in partial fulfillment of the requirements
for the degree of

Doctor of Philosophy

at the

MASSACHUSETTS INSTITUTE OF TECHNOLOGY

June 1999

Author _____
Department of Aeronautics and Astronautics
June 30, 1999

Certified by _____
Mark Drela
Thesis Supervisor, Associate Professor of Aeronautics and Astronautics

Certified by _____
Jack L. Kerrebrock
Professor of Aeronautics and Astronautics

Certified by _____
Jaime Peraire
Professor of Aeronautics and Astronautics

Accepted by _____
Jaime Peraire
Professor of Aeronautics and Astronautics
Chairman, Department Graduate Committee

Design and Analysis of Axial Aspirated Compressor Stages

by

Ali A. Merchant

Submitted to the Department of Aeronautics and Astronautics
on June 30, 1999, in partial fulfillment of the
requirements for the degree of
Doctor of Philosophy

Abstract

The pressure ratio of axial compressor stages can be significantly increased by controlling the development of blade and endwall boundary layers in regions of adverse pressure gradient by means of boundary layer suction. This concept is validated and demonstrated through the design and analysis of two unique aspirated compressor stages: a low-speed stage with a design pressure ratio of 1.6 at a tip speed of 750 ft/s, and a high-speed stage with a design pressure ratio of 3.5 at a tip speed of 1500 ft/s.

The aspirated compressor stages were designed using a new procedure which is a synthesis of low speed and high speed blade design techniques combined with a flexible inverse design method which enabled precise independent control over the shape of the blade suction and pressure surfaces. Integration of the boundary layer suction calculation into the overall design process is an essential ingredient of the new procedure. The blade design system consists of two axisymmetric through-flow codes coupled with a quasi three-dimensional viscous cascade plane code with inverse design capability. Validation of the completed designs were carried out with three-dimensional Euler and Navier-Stokes calculations.

A single spanwise slot on the blade suction surface is used to bleed the boundary layer. The suction mass flow requirement for the low-speed and high-speed stages are 1% and 4% of the inlet mass flow, respectively. Additional suction between 1-2% is also required on the compressor endwalls near shock impingement locations. The rotor is modeled with a tip shroud to eliminate tip clearance effects and to discharge the suction flow radially from the flowpath.

Three-dimensional viscous evaluation of the designs showed good agreement with the quasi three-dimensional design intent, except in the endwall regions. The suction requirements predicted by the quasi three-dimensional calculation were confirmed by the three-dimensional viscous calculations. The three-dimensional viscous analysis predicted a peak pressure ratio of 1.59 at an isentropic efficiency of 89% for the low-speed stage, and a peak pressure ratio of 3.68 at an isentropic efficiency of 94% for the high-speed rotor.

Thesis Chairman: Mark Drela
Associate Professor of Aeronautics and Astronautics

Acknowledgments

I would like to thank my thesis advisor Prof. Mark Drela for suggesting the aspirated compressor project as a thesis topic, for his guidance and contribution to this research, for allowing me the freedom to explore areas not closely related to my research topic, and for the finer things like teaching me the art of airfoil design, introduction to cappucino, roller blades, etc. Special thanks to Prof. Jack Kerrebrock for his guidance, constant encouragement, and for his confidence in my work. Thanks to Prof. Jaime Peraire, CFD guru, for access to FELISA and help with modifications to the code. I would also like to thank Prof. Carlos Cesnik for participating as a minor advisor.

Many thanks to Bob Haimes for providing uninterrupted awesome computing power, some career guidance, and weekly 7:00 am squash lessons.

Thanks to John Adamczyk for his valuable input to the design process and also for providing the 3-D viscous solutions. Thanks to Mark Celestina and Rick Mulac for carrying out the many 3-D viscous runs. Thanks also to Vivek Saxena and Wes Lord for their contributions to the designs and for the 3-D viscous solutions.

Thanks to Tolulope "so you think you know how to ... huh" Okusanya, Imran "Dingpo" IHaq, Bilal Mughal, Chris Van "Boobiyan" Sch., Ed Piekos who almost converted me to a vegan, Alex Budge, David "Darth Maul" Venditi, Joe "Maverick" Alescio, Brian Schuler, and other friends in CASL/FDRL and GTL for making this a wonderful and memorable experience.

Thanks a ton to Rob Scholten for proof-reading my thesis, and to Cliff "Doka" Wenn for the superb Chinese food and many squash games.

I thank my grandparents with all my heart for all their hard work. My grandfather M.P. Merchant whose achievements and actions have been a constant source of inspiration to me.

Contents

List of Figures

List of Tables

Nomenclature

c	blade chord
s	blade pitch
t/c	blade thickness ratio
x, y, z	cartesian coordinate directions
r, θ	radial, circumferential directions
m'	meridional arc length coordinate
$\vec{n}$	unit normal
N_b	number of blades per blade row
σ	blade chord to pitch ratio
Ω	angular speed
$\vec{V}$	absolute velocity
$\vec{W}$	relative velocity
U_b	blade speed
α, β	absolute, relative flow angles
η	efficiency
ψ	blade loading parameter
ϕ	flow coefficient
ω	loss coefficient
D	blade diffusion factor
AVR	axial velocity ratio
AVDR	axial velocity density ratio
B	axisymmetric area blockage
c_p, c_v	specific heats
γ	c_p/c_v
ρ	density
e, E	internal energy, total internal energy
T	temperature
T_w	adiabatic wall temperature
S	entropy

p	pressure
h, H	enthalpy, stagnation enthalpy
a	speed of sound
M	Mach number
I	rothalpy
C_p	pressure coefficient
s, η	shear layer coordinates
θ	momentum thickness
θ^*	kinetic energy thickness
δ^*	displacement thickness
δ	boundary layer thickness
τ	shear stress
C_m	suction mass flow coefficient
C_D	dissipation coefficient
C_f	skin friction coefficient
C_τ	shear stress coefficient
C_w	suction slot shear stress coefficient
H	shape parameter
H_k	kinematic shape parameter
H^*	kinetic energy shape parameter
Re_c	chord based Reynolds number
Re_θ	momentum thickness Reynolds number
$\rho_w v_w$	suction mass flux

Subscripts

e	boundary layer edge
inl, out	inlet, outlet
b	blade

0	stagnation
1	rotor inlet, suction slot upstream station
2	rotor exit / stator inlet
3	stator exit
stg	stage
rot	rotor
sta	stator
tip	blade tip
i	index
w	wall
suct	suction

Chapter 1

Introduction

1.1 Motivation & Background

Performance of compressor stages is measured in terms of pressure ratio and efficiency at a given blade speed. Higher pressure ratios per stage are desirable to reduce the total number of stages required to achieve a certain pressure ratio within an engine. This in turn leads to more compact and lighter engines with much reduced complexity. Improvement in efficiency reduces the energy input into the stage, or alternatively, more work can be extracted from the fluid being compressed. This has an impact on the thrust specific fuel consumption which is an important driving factor in the design of engines.

A compressor stage is composed of a rotating blade row, or rotor, which does work on a fluid followed by a stationary blade row, or stator, which recovers the kinetic energy from the swirling fluid leaving the rotor converting it into static pressure rise. By its very nature a compressor decelerates the flow, thus the maximum pressure ratio at a given tip speed is limited by the effects of viscosity. The adverse pressure gradient across the stage may lead to separation of the viscous boundary layers on the blades and the flowpath enclosing the blades resulting in a loss in pressure ratio, decrease in efficiency, and possibly stall or surge of the stage. Thus, if boundary layer growth on the blades and the flowpath can be controlled, separation can be delayed and higher stage pressure ratio, or work output, can

be achieved.

Attempts at increasing pressure ratio have focused mainly on increasing tip speed and improving blade shapes to deal with the harsher transonic and supersonic flow conditions. The most notable design is the low aspect ratio stage designed by Wennerstrom in 1971 [58]. The stage achieved a peak pressure ratio of 1.95 and peak isentropic efficiency of 90% at 1500 ft/s. This design set a new standard and direction for future development of high speed stages. Following the Wennerstrom design, no significant improvements in pressure ratio have been made in conventional high-speed stages. The low aspect ratio transonic rotors studied by Law and Wadia [31] in the 90's have shown pressure ratios below 2 and isentropic efficiencies in the neighborhood of 85%.

Along with the development of conventional compressor stages, many unconventional approaches to increasing pressure ratio have been attempted. Once again, the most notable contribution is the use of splitter vanes by Wennerstrom [59]. This initial attempt was not very successful, but with improvements in design and analysis methods splitter vanes have been applied successfully to achieve higher pressure ratios by Sehra [55] and recently by Allied Signal [45] where a stage pressure ratio of 3.5 was achieved at 1800 ft/s. Other approaches such as vortex generators, slotted blades, and tandem blades have also been studied and are surveyed by Wennerstrom [61].

Boundary layer control by suction has found limited use as a method of improving compressor performance. One difficulty is implementing this scheme on rotating blade rows, and in general the mechanical complexity of a compressor has deterred its use. A review of boundary layer suction applied in turbomachinery is given by Reijnen [41] which indicates that the potential for improving compressor performance by suction had been recognized early on, and research in applying suction through slots on rotor and stator blades can be traced back to 1950. A notable success is the experiment of Loughery et al. [34] where blowing and suction were used on high lift stator blades. Their results indicate that a substantial improvement in stator exit turning angle and isentropic efficiency were achieved with the use of suction. They also observed that suction was a more effective method of controlling the boundary layer than blowing.

The design of blade shapes have also evolved with the demand for better performance and improvements in design and analysis methods. Early subsonic blades were chosen from profile families such as the NACA series to meet thickness and turning requirements. With increase in blade tip speeds into the transonic regime, these were followed by the double circular arc blades, and by multiple circular arc blades in the supersonic regime where more control was required over the blade shape. These profile families were later followed by supersonic blades designed to achieve a specific wave pattern in the supersonic region with a simple wedge shaped subsonic pressure recovery [53, 4]. Arbitrary camber line shapes were used with introduction of methods to calculate the meridional flow [60]. The ARL-SL19 supersonic compressor cascade is an example of an arbitrary camber line design which shows advanced features such as pre-compression in the forward supersonic region [54]. In high-speed blade design, the arbitrary camber line with prescribed thickness distribution are used to this day, and improvements in computational methods and introduction of inverse design have only served as a means of better controlling the shape of the camber line. In contrast, in the low-speed regime the potential of utilizing inverse design methods have been recognized as shown in a study by Starken [49]. This can be attributed to the larger turning requirements which place a greater demand on the detailed design of the blade shape. Controlled diffusion cascades of Hobbs and Weingold [19] are an example of this next generation of transonic cascades where detailed design of the blade shape allows virtually shockless supercritical flow along with large subsonic pressure recovery and turning.

1.2 Previous Aspirated Compressor Research at MIT

The potential for improving axial compressor performance by using boundary layer control was recognized in 1980 by Kerrebrock. He made the astute observation [26] that boundary layer suction at shock locations, similar to external precompression supersonic engine inlets, and blade shapes tailored to optimize the viscous flow could lead to substantial improvements in compressor performance. This sparked the aspirated compressor program at MIT.

An experimental investigation of the use of boundary layer control on a rotating blade row was carried out at MIT by Reijnen [41]. Five blades of an existing rotor designed to achieve a pressure ratio of 1.6 at a tip speed of 1200 ft/s were modified with suction scoops to bleed the boundary layer at the shock impingement location. The experiment was conducted in the MIT Blowdown Compressor Facility [25]. Little difference was observed in the performance at design conditions, but at lower mass flow the modified blades showed an increase in turning and higher static pressure ratio. This improvement was attributed to thinner boundary layers due to suction. Another observation was the delay in the eventual stall of the rotor.

A study of fan pressure ratio and bypass ratio of an engine, and a subsequent design of a fan with a pressure ratio of 2 at a tip speed of 1000 ft/s was carried out by Smilg [47]. The transonic cascade design and analysis code MISES was used to design the blade shapes. The suction model in this study was unreliable and predicted mass flow requirements as high as 8% of the inlet mass flow. As a result the blade sections were not adequately designed and in some cases converged solutions of the MISES streamsurface calculations were not obtained.

A preliminary design of a stage achieving a pressure ratio of 3 at a tip speed of 1500 ft/s was carried out by Ziminsky [66] using MISES. The suction requirement for the rotor was 2.5%, except at the hub, and approximately 3.5% for the stator. It is interesting to note the lower suction requirement compared to the fan design by Smilg despite the higher blade loading and tip speed. Similar solution convergence problems were encountered in this design study resulting in insufficient blade shapes to build a three-dimensional geometry.

Recently, new results were presented on a family of aspirated compressor designs by Kerrebrock et al [27] which clearly indicated the substantial increase in stage work that could be realized with aspiration, and also presented a systematic blade design methodology.

1.3 Thesis Objectives

The aspirated compressor research has shown that substantial increases in pressure ratios can be realized with aspiration and justified the need to further refine the preliminary designs. Issues such as blade loading limits, suction requirement, and feasible blade geometries also needed to be explored.

The primary objective of this thesis was to develop complete aspirated compressor stage designs, with suction as an integral component, which can be manufactured and experimentally tested. The compressor stage designs addressed in this thesis represent two distinct flow regimes: a low-speed fan stage with subsonic blade speed and a high-speed core compressor or fan stage with supersonic blade speed. The low-speed fan stage is designed to achieve a pressure ratio of 1.6 at a tip speed of 750 ft/s. This represents a substantial decrease in blade speed from conventional fans which produce the same pressure ratio at tip speeds greater than 1200 ft/s. Some important advantages of lowering the tip speed are: (1) a considerable reduction in flow field complexity, i.e. weak or no shocks, (2) reduction in structural stress in the blades, and (3) reduction in noise. The high-speed stage is designed to achieve a pressure ratio of 3.5 at a tip speed of 1500 ft/s. This design represents a substantial increase in pressure ratio over conventional compressor stages which achieve a pressure ratio between 2 and 2.3 at the same blade speed. In the high-speed regime, stage pressure ratio is limited by the blade speed due to structural integrity and due to the shock strength which induces boundary layer separation. Thus, the high-speed aspirated stage represents a significant advance in the maximum pressure ratio that can be achieved in a single stage at 1500 ft/s.

The unusually high blade loading of aspirated compressor stages required a fresh look at the blade design system as well as the design philosophy. In contrast to traditional design systems which rely on the axisymmetric streamline curvature method, the design system employed in this thesis uses the quasi 3-D blade to blade code MISES [65] coupled with a through-flow code. The quasi 3-D code is used to design and analyze blade sections which are stacked to form the 3-D blade. The inviscid-viscous formulation and inverse design features in MISES provide unprecedented flexibility in designing the blade shapes. A robust

suction model is included in the boundary layer formulation to make the suction calculation an integral part of the blade design process. MISES requires streamsurface and flow condition inputs which are supplied by two through-flow solvers. In contrast to streamline curvature methods, the through-flow solvers used in this thesis so the complete axisymmetric Euler equations providing more accurate meridional streamline variation in the flowpath as well as within the blade rows. The 3-D blade geometries were analyzed using an inviscid solver based on the unstructured finite element code FELISA [39], and viscous analyses of the completed geometries were carried out using the APNASA [3] code by Adamczyk and Celestina at NASA Glen research center.

1.4 Thesis Organization

Chapter 2 introduces a simplified compressor stage analysis where equations relating important parameters characterizing the performance of compressors are derived and examined in a parameter study. Chapter 3 takes a closer look at the effects of boundary layer suction, suction mass flow requirement, and the impact of suction on stage isentropic efficiency. In Chapter 4, the suite of computational tools comprising the design system are described along with the overall stage design procedure. Chapter 5 presents a detailed description of the aspirated blade design methodology. Chapters 6 and 7 present detailed results of the low-speed and high-speed stage analyses. Finally, conclusions and recommendations are addressed in Chapter 8. A stability analysis of an isolated compressor stage is presented in Appendix A.

Chapter 2

Preliminary Design Study

The application of boundary layer control to increase blade loading opens a new range of design possibilities which have until now been impractical due to limitations imposed by viscous effects. In this regard, a parametric analysis of a compressor stage is essential in order to efficiently examine this larger space for feasible designs and identify possible limitations early in the design process. In this chapter a cascade plane approach is used to derive simple kinematic and thermodynamic relationships involving parameters such as blade loading and blade speed which determine pressure ratio. The link with viscous affects is established through the diffusion factor concept which is also adapted to blades with boundary layer suction. A parameter study is presented which examines the new limits set by the use of boundary layer suction.

2.1 Compressor Stage Analysis

A cascade plane view of a compressor stage is shown in Figure 2-1. This corresponds to an unwrapped streamsurface intersecting the blade rows at some radius along the flowpath. The axial direction x is the arc length along the streamsurface and θ is the circumferential direction. The flow is assumed to be steady and adiabatic in the frames of reference relative to the rotor and stator, respectively.

The relation between the absolute and the relative velocities is given by

$$\vec{V} = \vec{W} + \vec{\Omega} \times \vec{r}$$

$$V_x = W_x \tag{2.1}$$

$$V_\theta = W_\theta + \Omega r$$

where Ωr is the rotor blade speed. The absolute and relative flow angles are denoted by α and β, respectively. The flow enters the stage axially where the rotor increases the stagnation enthalpy by imparting angular momentum to the flow followed by the stator where the flow is returned to the axial direction. The stagnation enthalpy rise, or stagnation

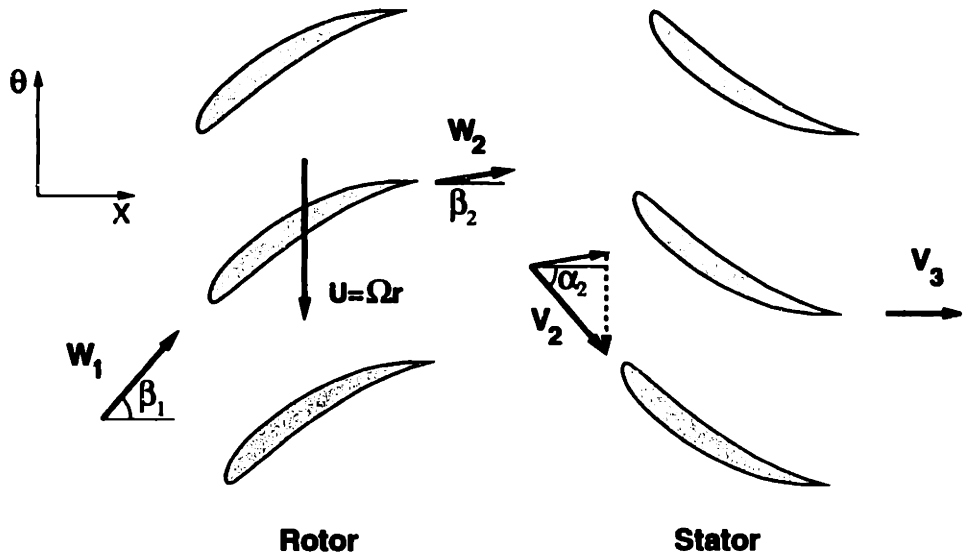

Figure 2-1: Cascade plane view of a compressor stage.

temperature rise assuming a calorically perfect gas, is given by the Euler turbine equation which is simply a statement of the conservation of angular momentum and energy.

$$\Delta H = \Omega \Delta(rV_\theta)$$

$$\frac{T_{03}}{T_{01}} = 1 + \frac{\Omega \Delta(rV_\theta)}{H_{01}} \tag{2.2}$$

The corresponding stagnation pressure rise can be obtained using isentropic relations

$$\begin{aligned} \frac{p_{03}}{p_{01}} &= \left[1 + \eta_{stg}(\gamma - 1)M_{b0}^2\psi\right]^{\frac{\gamma}{\gamma-1}} \\ \eta_{stg} &= \frac{T_{03s} - T_{01}}{T_{03} - T_{01}} \\ M_{b0} &= \frac{U_b}{a_{01}} \\ \psi &= \frac{\Delta H}{U_b^2} \end{aligned} \tag{2.3}$$

where η_{stg} is the stage isentropic efficiency, M_{b0} is the blade Mach number based on the inlet stagnation speed of sound, and ψ is the blade loading parameter measuring the fraction of the blade energy imparted to the fluid. Equation (2.3) shows that the stage pressure ratio is primarily a function of the blade speed and loading. Since the blade loading is limited by viscous effects, achieving higher pressure ratios by increasing blade speed is the only practical alternative for conventional compressors.

Increasing the blade loading requires larger turning and deceleration of the flow through the rotor. Knowledge of the rotor relative exit flow angle is important for design purposes as it is a measure of the blade loading and geometric camber. The rotor exit relative flow angle can be related to the blade loading parameter by equation (2.2) and velocity-flow angle relations.

$$\tan\beta_2 = \left(\frac{r_2}{r_{tip}}\right)\left[1 - \psi\left(\frac{r_{tip}}{r_2}\right)^2\right]\frac{1}{\mathrm{AVR}\phi} \tag{2.4}$$

AVR is the axial velocity ratio V_{x2}/V_{x1}, and ϕ is the flow coefficient V_{x1}/U_b. For simplicity, free vortex flow is assumed and all the parameters are based on rotor tip values making the exit angle a function of the radius r_2. Increasing the blade loading may result in the flow turning past the axial direction. This increases the stator inlet Mach number increasing shock loss and also impacts the stability of the compressor by decreasing the slope of the pressure rise characteristic.

From the argument presented above it follows that the stator inlet Mach number is an essential design parameter. An estimate of the stator inlet Mach number can be obtained

by combining equations (2.2), (2.4), and isentropic relations to give

$$M_{stat} = \sqrt{\frac{(M_{x0}\,\mathrm{AVR})^2 + (M_{b0}\,\psi)^2}{1 + M_{b0}^2\psi\left(\gamma - 1 - \frac{1}{2}\psi\right) - \frac{1}{2}\left(M_{x0}\mathrm{AVR}\right)^2}} \tag{2.5}$$

where M_{x0} is the axial Mach number based on the inlet stagnation speed of sound. The important parameters which affect the stator Mach number are the blade loading and blade speed.

The above equations are sufficient to establish flow angles through the stage but provide no indication of the blade boundary layer behavior and viscous losses. The diffusion factor, first introduced by Lieblin [32], correlates the viscous losses with the deceleration of the flow through the blade passage. The boundary layer on the blade suction surface was recognized as the limiting factor, and the original diffusion factor was defined as the ratio of the peak velocity on the suction surface to the exit velocity. This definition subsequently evolved into a more convenient and widely accepted form based only on inlet and exit quantities.

$$D = 1 - \frac{W_2}{W_1} + \frac{\Delta(rW_\theta)}{2\sigma\bar{r}W_1} \tag{2.6}$$

Here, the relative velocity W is used for a rotor and absolute V for a stator, and σ is the chord to pitch ratio or solidity. The above equation can also be written in a more convenient form in terms of the flow coefficient and blade loading parameter

$$D = 1 - \frac{1}{\sqrt{1+\phi^2}}\left[\mathrm{AVR}\sqrt{(\psi+1)^2+\phi^2} - \frac{\psi}{2\sigma}\right] \tag{2.7}$$

The diffusion factor is correlated with the cascade wake momentum thickness or a loss parameter ($\omega\cos\beta_2/\sigma$), where ω is the total pressure loss coefficient, β_2 is the blade exit angle, and σ is the solidity. Although derived for low-speed cascades, the diffusion factor has been used successfully in the design of high speed blades as well by Wennerstrom [58] and Sehra [55]. A common feature of the diffusion factor correlation is a rapid increase in the losses for diffusion factors approaching 0.6, and is indicative of possible separation of the blade boundary layer. For design purposes, a widely accepted notion is that it is

desirable to keep the diffusion factor well below 0.6.

Boundary layer control will allow larger turning and deceleration of the flow, and the diffusion factor must be adapted to predict a new limit in terms of existing correlations. An estimate of the increase in the diffusion limit for blades with suction can be obtained by drawing an analogy with tandem cascades. Tandem cascades have been used in low and high speed compressors to considerably increase blade loading above that of single blades as described in Gostelow [13]. Assuming that each cascade in a series of tandem cascades is designed to turn and diffuse the flow then it should be possible to achieve a higher pressure rise while maintaining a low enough loading on each individual cascade. Similarly, suction may be implemented through one or more slots on the blade and each segment of the blade between these slots can be designed to turn and diffuse the flow without separation. Thus, each segment will have its own effective diffusion factor. A similar approach has been used by Sehra [55] to extend the diffusion factor correlation to the design of splittered supersonic cascades where an effective diffusion factor is computed based on the combined solidity of the main element and splitter vane. To extend the diffusion factor concept to blades with suction it is convenient to write the total diffusion factor as a sum of smaller increments over the blade surface

$$D_{\text{tot}} = \sum \frac{\Delta W_i}{W_1} + \sum \frac{\Delta (rW_\theta)_i}{2\sigma \bar{r} W_1} \tag{2.8}$$

where $\Delta W_i = W_i - W_{i+1}$. Rearranging the above equation gives

$$D_{\text{tot}} = \sum D_i = \sum \frac{W_i}{W_1} \left(1 - \frac{W_{i+1}}{W_i} + \frac{\Delta (rW_\theta)_i}{2\sigma \bar{r} W_i} \right) . \tag{2.9}$$

The above equation can be used in conjunction with an inviscid velocity distribution to obtain a preliminary estimate of the number of suction slots and possible locations. The approach described above is applied to an example of a supersonic blade with one suction slot located downstream of the passage shock where the boundary layer is likely to separate. A conventional supersonic section with no turning is designed for a typical diffusion factor of 0.5 and velocity ratio across the shock of 0.7. If turning requiring an effective diffusion factor of 0.4 is introduced in the subsonic part of the blade with the aid of suc-

tion, then it should be possible to achieve a total diffusion factor of 0.78 estimated using equation (2.9).

2.2 Parameter Study

The pressure ratio using equation (2.3) is plotted in Figure 2-2 versus blade speed for increasing blade loading parameters, and assumed isentropic efficiency of 90%. The corresponding diffusion factors are plotted in Figure 2-3 versus flow coefficient. Conventional compressor stages have rotor blade loadings between 0.4 and 0.5 so the first curve is a

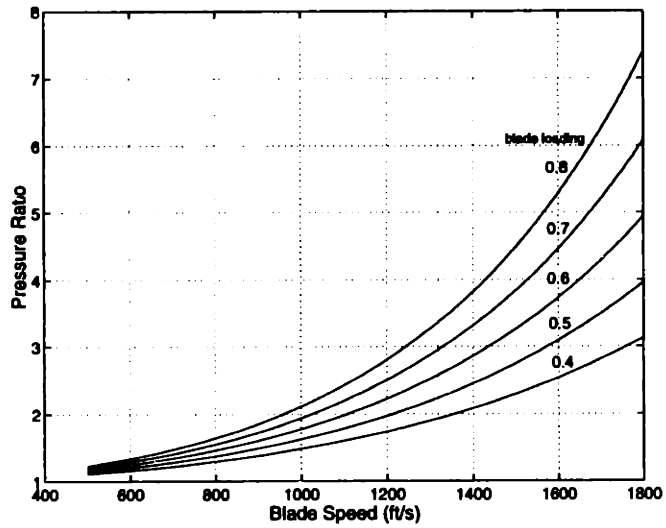

Figure 2-2: Pressure ratio vs. blade speed for various blade loading parameters.

good indicator of the possible pressure ratios at the corresponding tip speeds for conventional compressor designs. At a typical inlet axial Mach number of 0.65, a flow coefficient of 1 is representative of low speed stages with blade speeds below 1000 ft/s, and a flow coefficient of 0.5 for high speed stages with blade speed in the 1500 ft/s range. At tip speeds of 1500 ft/s the typical pressure ratio is 2.2 for a single stage, and from Figure 2-3 it seen that the maximum diffusion factor is around 0.55 for a flow coefficient of 0.5. This is consistent with the Wennerstrom rotor [58] and a family of advanced rotor designs presented in Wadia [57]. As shown earlier, for blades with a single suction slot the diffusion factor

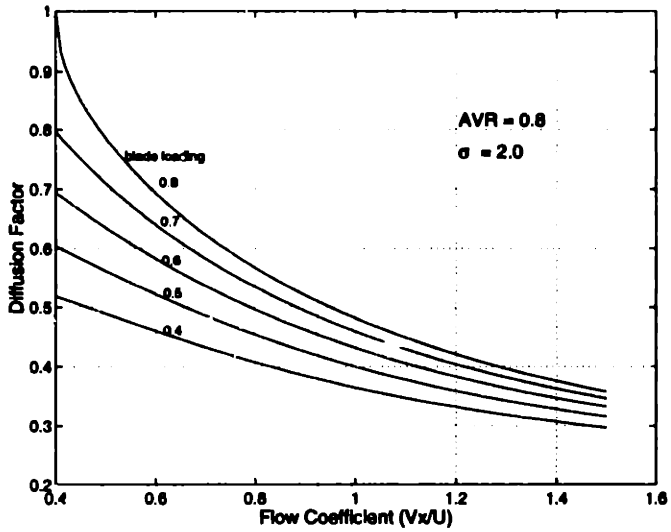

Figure 2-3: Diffusion factor vs. flow coefficient for various blade loading parameters.

limit is raised to approximately 0.78 which suggests that a blade loading of at least 0.7 may be achieved without encountering high losses. Figure 2-2 shows that pressure ratios close to 4 can be achieved at 1500 ft/s and 4.5 at a slightly higher 1600 ft/s tip speed for a blade loading of 0.7. An interesting observation in Figure 2-3 is that the diffusion factor decreases quite rapidly with flow coefficient, which implies lower blade speeds or higher inlet mass flow. This suggests that higher blade loading, and consequently higher pressure ratios, could also be achieved by lowering the blade speed while maintaining the same diffusion factor. Some advantages of lowering the blade speed are smaller shock losses due to lower Mach numbers and lower structural stresses in the blade.

The rotor relative exit flow angle along the span is plotted in Figure 2-4 for different flow coefficients based on tip values for a typical AVR of 1, tip blade loading parameter of 0.7, constant work along the span, and no inlet swirl. The radius at which the flow is turned past the axial direction is $r_{\text{tip}}\sqrt{\psi}$ and can be altered only by adding swirl upstream of the rotor. For typical hub exit radius of 0.65, Figure 2-4 shows that the flow will be turned past axial around mid-span, and large negative flow angles of $-20°$ to $-40°$ will occur near the hub. Turning the flow past the axial direction will decrease the slope of the static pressure rise characteristic and may result in static instability of the stage. A detailed analyses of

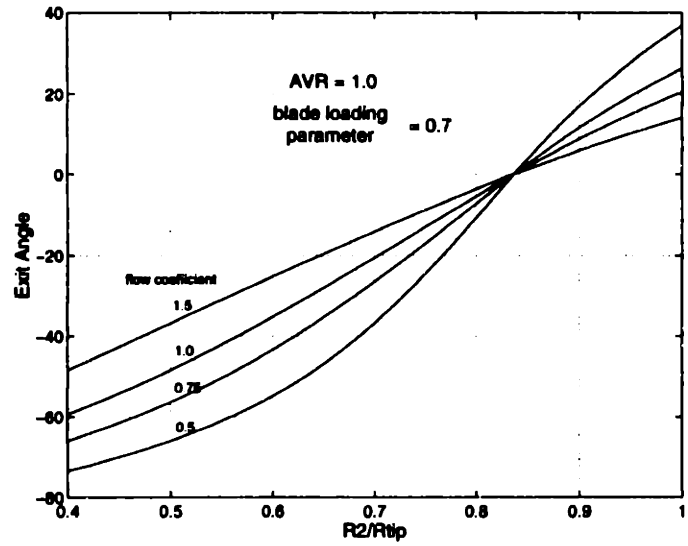

Figure 2-4: Relative exit angle vs. exit radius for various flow coefficients.

the effect of negative exit angles on stage stability is addressed in Appendix A. The effect of the flow coefficient on the exit angle is interesting because of its effect on the slope of these curves. At lower flow coefficients the change in β_2 with radius increases indicating a large twist in the blade from hub to tip which may impact structural requirements. Also at a flow coefficient of 0.5, the total turning at the tip could be as high as 30°, compared to $2° - 5°$ in conventional compressors.

Figure 2-5 shows the variation of stator inlet Mach number with blade loading parameter at an AVR of 1 and inlet axial Mach number of 0.65. The stator Mach number increases with increasing blade loading and also shows a rapid increase with blade relative Mach number. For a blade loading parameter of 0.7 the stator inlet Mach number could be as high as 1.3 for a blade speed of 1500 ft/s. An increase in the axial velocity ratio will also increase the stator Mach number. These curves also show that lowering blade speed and simultaneously increasing blade loading to maintain a given pressure ratio will lower the stator inlet Mach number.

In summary, the following conclusions can be drawn from the parameter study:

1. The the diffusion factor limit can be raised from 0.6 used on conventional blades to

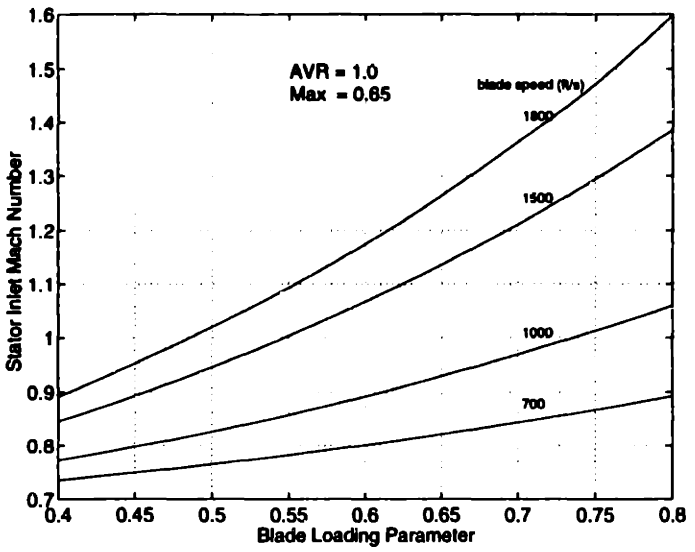

Figure 2-5: Stator inlet Mach number vs. blade loading parameter for various blade speeds.

2. If diffusion factors as high as 0.75 can be achieved with suction, then the blade loading can be increased at least by a factor of two.

3. The use of suction is attractive in both low and high tip speed applications.

4. Higher blade loading parameters result in negative rotor exit angles which impose design limitations at the hub. Static stability may be affected, and larger spanwise twist in the blade could impose design limitations in order to meet structural requirements.

5. Supersonic stator inlet Mach numbers are inevitable as blade loading and blade speed are increased.

Chapter 3

Boundary Layer Suction

The feasibility of using boundary layer suction to increase blade loading rests on the effectiveness of suction in controlling the development of the boundary layer and the amount of suction mass flow required. The effectiveness in controlling the boundary layer growth will ultimately determine the increase in blade loading and consequently the improvement in pressure rise that can be achieved. This chapter examines the suction mass flow requirement followed by an analysis of the effect of suction on the boundary layer development. The impact of discharging the suction fluid radially outward through the rotor tip on stage isentropic efficiency is examined, and a brief summary of a preliminary systems study of integrating an aspirated compressor into an engine is presented .

Boundary layer suction can be implemented through a porous surface, a single or series of flush slots, or a forward-facing scoop on the blade surface. Suction through porous or perforated surfaces finds application mainly in laminar flow control where suction is required over a significant area of the blade surface. Porous surfaces are generally difficult to manufacture and maintain and would impose a larger thickness requirement if used on compressor blades. Where suction is used to control separation, and maintaining laminar flow is not an issue, slots and scoops are preferred. Boundary layer scoops are very efficient when operating at design mass flow because the dynamic pressure of the incoming boundary layer can be recovered with minimal disturbance to the external in-

viscid flow. Their performance will deteriorate rapidly at off-design conditions resulting in a large loss due to separation and mixing at the lip of the scoop [52]. In this respect, a flush slot is a suitable alternative as it is almost insensitive to changes in mass flow rate when properly designed as observed experimentally by Pierpont [40]. Suction on the aspirated compressor designs presented in this thesis is applied through flush slots; a decision based on mechanical simplicity and fabrication constraints. In the analysis presented in this chapter, and in the remainder of this thesis, a flush slot is implied and the details of the slot geometry such as inclination to the surface are considered outside the scope of the modeling assumptions in this thesis.

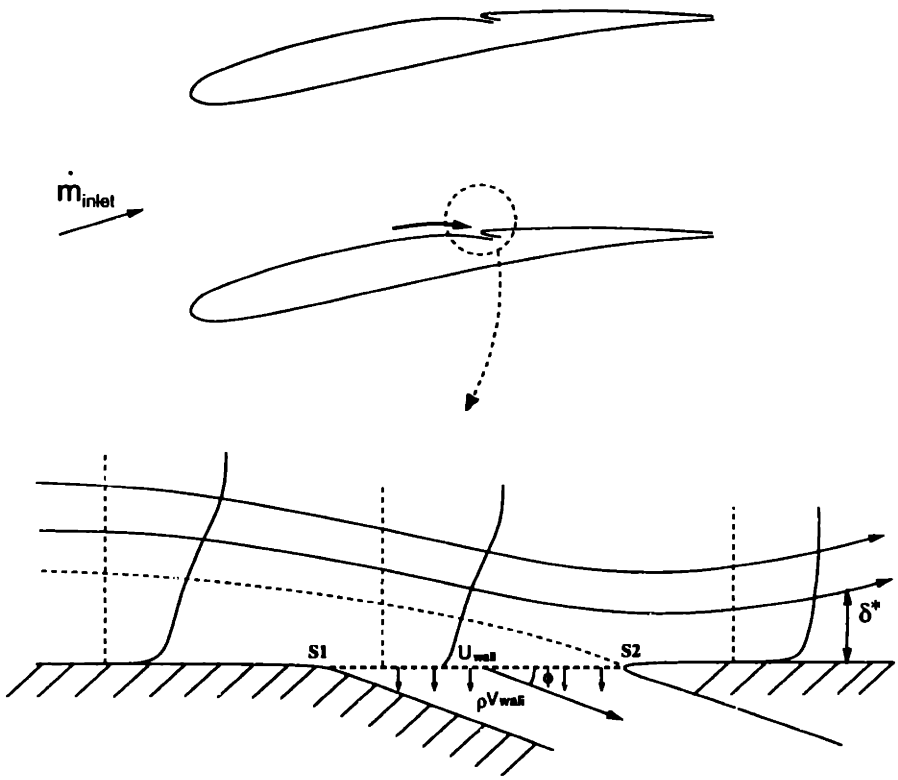

Figure 3-1: Schematic of a flush suction slot.

3.1 Suction Mass Flow Requirement

The mass flow removed from the boundary layer by suction is quantified in terms of a fraction of the inlet flow into a cascade

$$C_m = -\frac{1}{\dot{m}_{\text{inl}}} \int_{s_1}^{s_2} \rho_w v_w ds \tag{3.1}$$

where s_1 and s_2 define the length of the slot and $\rho_w v_w$ is the normal mass flux into the slot. A convenient measure of the suction mass flow is the displacement length associated with the suction mass defect defined as

$$\delta^*_{\text{suct}} = -\int_{s_1}^{s_2} \frac{\rho_w v_w}{\rho_e u_e} ds \ . \tag{3.2}$$

The suction coefficient C_m can now be expressed in terms of δ^*_{suct} and boundary layer parameters upstream of the slot

$$C_m = \left(\frac{\delta^*_{\text{suct}}}{\delta^*_1}\right) \left(\frac{Re_{\theta 1}}{Re_c}\right) H_1 \sigma \tag{3.3}$$

where δ^*_1 is the upstream displacement thickness, $Re_{\theta 1}$ is the upstream momentum thickness Reynolds number, Re_c is the freestream Reynolds number based on blade chord, H_1 is the boundary layer shape parameter, and σ is the cascade solidity.

The ratio $(\delta^*_{\text{suct}}/\delta^*_1)$ is an intrinsic measure of the effectiveness of suction in decreasing the momentum thickness and displacement thickness by a certain fraction. Experiments on boundary layer suction at subsonic speeds by Pierpont [40], and supersonic speeds by Syberg [52] and Loughery [34], indicate that the $(\delta^*_{\text{suct}}/\delta^*_1)$ typically is between 1 and 2 which suggests that $(\delta^*_{\text{suct}}/\delta^*_1)$ will vary little regardless of the application. This implies that the suction coefficient will depend strongly on the condition of the boundary layer upstream of the slot, reflected by $Re_{\theta 1}$ and H_1 in equation (3.3). The suction requirement will also increase with solidity or blade count assuming a constant blade chord.

It is instructive to estimate the magnitude of C_m for a typical cascade.

$$\begin{aligned}
\frac{\delta^*_{\text{suct}}}{\delta^*_1} &\simeq 1.0 \\
Re_{\theta 1} &\simeq 1200 \\
Re_c &\simeq 2.0 \times 10^6 \\
H_1 &\simeq 2.0 \\
\sigma &\simeq 1.5 \\
C_m &= 0.0018
\end{aligned}$$

This example shows that suction coefficients are expected to be on the order of a few percent of the inlet mass flow which is an important factor in determining the feasibility of applying aspiration to compressors.

3.2 Effects of Boundary Layer Suction

The effect of boundary layer suction can be divided into a local effect, where the boundary layer is modified by the suction slot, and the effect of that change on the downstream development of the boundary layer. These two effects can be examined by applying the integral momentum equation first across the suction slot and then downstream of the slot up to the blade trailing edge. Incompressible flow is assumed in the following analysis for simplicity since the conclusions will apply in a relative sense to the compressible case.

3.2.1 Effect of the Suction Slot

Referring to Figure 3-1, the integral momentum equation derived with the effect of transpiration is

$$\frac{d\theta}{ds} + (2+H)\frac{\theta}{u_e}\frac{du_e}{ds} = \frac{C_w}{2} + \frac{\rho_w v_w}{\rho_e u_e}\left(1 - \frac{u_w}{u_e}\right) \tag{3.4}$$

where C_w is a shear stress coefficient evaluated along the slot inlet, $\rho_w v_w$ is the normal mass flux into the slot, and u_w is the streamwise boundary layer velocity at the entrance to the slot. The usual definitions of δ^* and θ hold, but the velocity at the wall is no longer zero. In the case of suction through a porous wall with a no-slip boundary condition, C_w will revert to its usual definition of skin friction, and $u_w = 0$. Equation (3.4) can be written in a differential logarithmic form

$$d(\ln\theta) = \frac{C_w}{2\theta}\,ds - (2+H)\,d(\ln u_e) + H\frac{\rho_w v_w}{\rho_e u_e}\left(1 - \frac{u_w}{u_e}\right)\frac{ds}{\delta^*} \tag{3.5}$$

and integrated across the slot to provide an estimate of the momentum thickness change across the slot

$$\frac{\Delta\theta}{\theta_1} \simeq 1 - \left(\frac{u_{e2}}{u_{e1}}\right)^{-(2+H)} \exp\left(-H\,\frac{\delta^*_{\text{suct}}}{\delta^*}\left(1 - \frac{u_w}{u_e}\right)\right). \tag{3.6}$$

The contribution from C_w can be neglected since the slot width is small. The quantities outside the differentials H, δ^*, and u_w are now averages across the slot. An interesting result is that the contribution of suction to momentum thickness change resides in the exponential term which will decay rapidly as the amount of suction is increased, and u_w will simultaneously approach u_e. Also for strong suction u_{e2} will approach zero as the external streamline is drawn towards the stagnation point at the downstream lip of the slot. Hence, the effectiveness of suction will diminish as $(\delta^*_{\text{suct}}/\delta^*)$ is increased. The localized effect of the suction slot and the strong effect of $(\delta^*_{\text{suct}}/\delta^*)$ on the boundary layer have been confirmed in a systematic experiment by Pierpont [40]. The experiment showed that the change in the boundary layer parameters across the slot depended only on $(\delta^*_{\text{suct}}/\delta^*)$ for a slot with rounded edges and maximum effectiveness in controlling the boundary layer was obtained for $(\delta^*_{\text{suct}}/\delta^*) \sim 1$.

3.2.2 Downstream Development

The effect of boundary layer suction on the downstream development of the boundary layer is examined by stepping back and considering only the momentum thickness change

$\Delta\theta_2$ regardless of its origin. Two limiting cases can be identified depending on the flow situation.

A) Strongly-attached flow:

$$\begin{aligned} \frac{d\theta}{ds} &\simeq \frac{C_f}{2} \\ \theta(s) &\simeq \theta_2 + \int_{s_2}^{s} \frac{C_f}{2}\, ds \\ \Delta\theta(s) &\simeq \Delta\theta_2 \end{aligned} \tag{3.7}$$

B) Nearly-separated flow:

$$\begin{aligned} \frac{d\theta}{ds} &\simeq -(2+H)\frac{\theta}{u_e}\frac{du_e}{ds} \\ \theta(s) &\simeq \theta_2 \exp\left[\int_{s_2}^{s} -(2+H)\frac{1}{u_e}\frac{du_e}{ds}\, ds\right] \\ \Delta\theta(s) &\simeq \Delta\theta_2 \exp\left[\int_{s_2}^{s} -(2+H)\frac{1}{u_e}\frac{du_e}{ds}\, ds\right] \end{aligned} \tag{3.8}$$

Equation (3.7) makes the assumption that turbulent C_f depends weakly on Re_θ, and H does not change much. The exponential factor in (3.8) will change with θ_2 since $H(s)$ will change, but this factor remains large. The significant distinction here is that in the attached-flow case A, $\Delta\theta_2$ persists mostly without change downstream as indicated in Figure 3-2, while in the nearly-separated flow case B it is "magnified" by the exponential factor, which in applications can easily exceed 10 near the trailing edge. Thus a large amount of control over the downstream boundary layer thickness can be exercised by removing only a very small amount of mass flow in the appropriate location. In the strongly-attached flow case A the change is not magnified and suction is counterproductive since the $\Delta\theta$ (loss) decrease is more than offset by pumping power required. Case A also puts an upper limit on the desired amount of suction in any situation, since once the flow is firmly attached, increasing suction further will have little effect on the flow.

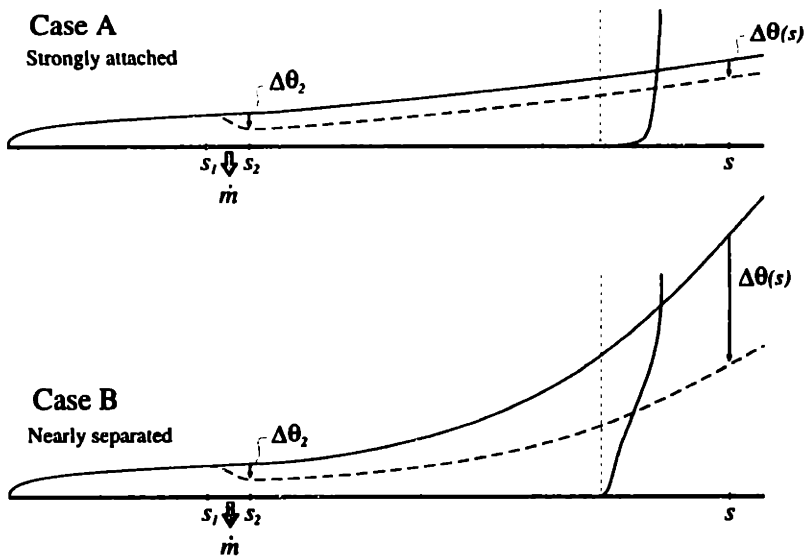

Figure 3-2: Effect of suction on boundary layer growth.

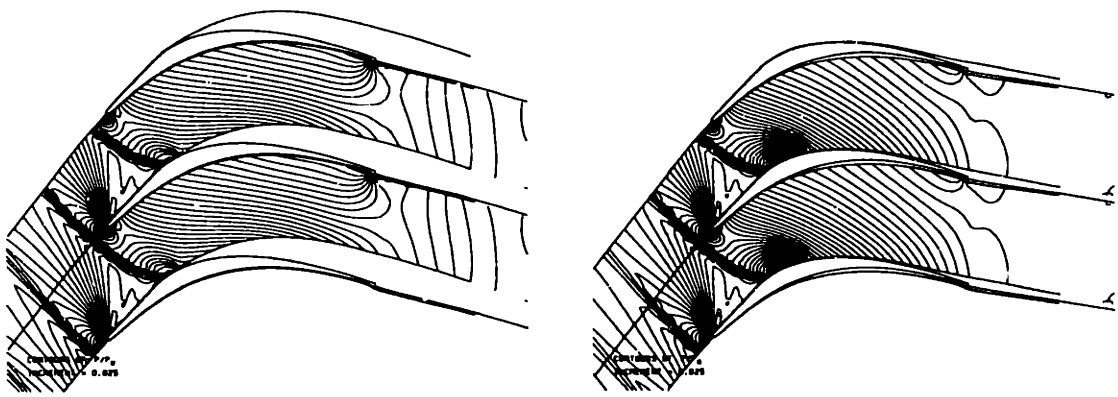

(a) Without Suction

(b) With Suction

Figure 3-3: Compressor cascade with and without suction. Inlet Mach number and flow angle are imposed.

For the greatest control authority with the least amount of mass removal, the best location to apply suction is at the start of a strong pressure-recovery region, since the exponential magnification is then the greatest over the downstream part of the flow. Of course, some degree of control is still obtained at different locations. This feature is important in that the "optimum" location is likely to change with different operating conditions (e.g. with different shock locations). Control is still possible, although somewhat more suction mass flow may be required to achieve a given effect.

To illustrate these points Figure 3-3 shows a compressor cascade with high turning at supersonic relative inlet Mach number with and without suction, but with identical blade shapes in both cases. With suction the boundary layer remains attached whereas without suction, the boundary layer separates immediately after the shock. The overall loss ω increases by a factor of 3 and the viscous loss increases by a factor of 10. The suction mass flow is 2% of the inlet mass flow. The effects of meridional streamline curvature have been neglected in this calculation.

3.3 Suction Power Requirement

3.3.1 Idealized Study

Bleeding the boundary layer requires work and the total pressure recovery of the fluid at the location of discharge outside the flowpath of the engine will determine its usefulness, for example, within a secondary flow network of the engine. If such utilization of the fluid is possible then the impact of boundary layer suction on the engine efficiency can be offset, at least to some extent.

In the case of the stator, the suction fluid will be discharged at a high enough total pressure to be utilized elsewhere in the engine. For a stationary blade row the ideal power required to return the boundary layer removed by suction to freestream conditions will be proportional to the suction mass flow and the kinetic energy deficit upstream of the slot similar to the case of an isolated airfoil [35].

In a thermodynamic context, Kerrebrock [28] has shown that approximately 0.17% increase in isentropic efficiency per percent suction mass flow can be realized at bleed Mach numbers above 0.5, and the efficiency increment increases with relative Mach number. This increase in efficiency can be attributed to the compression work that is saved by removing the high entropy boundary layer from the core flow.

In the case of the rotor, the suction fluid can be removed from the tip or the hub. Removing the flow from the hub will allow recovery of the angular momentum, but this option may

not be possible in the initial compressor stages because of the relatively low discharge pressure. Removing the suction fluid from the tip may carry a penalty if the fluid is discharged at blade speed and recovery of that energy is not feasible. The penalty of removing the suction flow from the rotor tip can be assessed by comparing the total temperature rise of the core flow to that of the suction flow.

The total temperature rise for a stage with suction can obtained by applying mass and energy conservation across the stage.

$$\begin{aligned} \dot{m}_{\text{inl}}\Delta T_{0\text{stage}} &= (\dot{m}_{\text{inl}} - \dot{m}_{\text{rot}} - \dot{m}_{\text{sta}})\,(T_{03} - T_{01}) \\ &+ \dot{m}_{\text{rot}}\,(T_{0\text{rot}} - T_{01}) + \dot{m}_{\text{sta}}\,(T_{03} - T_{01}) \end{aligned} \tag{3.9}$$

where $\dot{m}_{\text{inl}}$ is the stage inlet mass flow, $\dot{m}_{\text{rot}}$ and $\dot{m}_{\text{sta}}$ are the suction mass flow required by the rotor and stator, respectively. $T_{0\text{rot}}$ is the total temperature at the location where the suction mass flow leaves the rotor, and $(T_{03} - T_{01})$ is the temperature rise of the core flow. The suction mass flows can be written as fractions of $\dot{m}_{\text{inl}}$ giving

$$\Delta T_{0stage} = (1 - C_{m\text{rot}})\,(T_{03} - T_{01}) + C_{m\text{rot}}\,(T_{0\text{rot}} - T_{01}) \tag{3.10}$$

where $C_{m\text{rot}} = \dot{m}_{\text{rot}}/\dot{m}_{\text{inl}}$. This can be rearranged to give the ratio of the total temperature rise of the core to that of the stage for radial discharge of the suction flow

$$\frac{\Delta T_{0\text{core}}}{\Delta T_{0\text{stage}}} = \frac{1}{1 + C_{m\text{rot}}\left(\frac{1}{\psi} - 1\right)} \tag{3.11}$$

where $\psi = (\Delta H/U_b^2)$ is the blade loading parameter.

Equation (3.11) is plotted in Figure 3-4 as an efficiency ratio for various blade loading parameters. The efficiency ratio improves with increasing blade loading which is expected since the tangential velocity deficit between the suction flow and the core flow will decrease. A higher blade loading parameter can be achieved at low blade speeds for a given pressure ratio since the diffusion factor is lower which suggest that the penalty of remov-

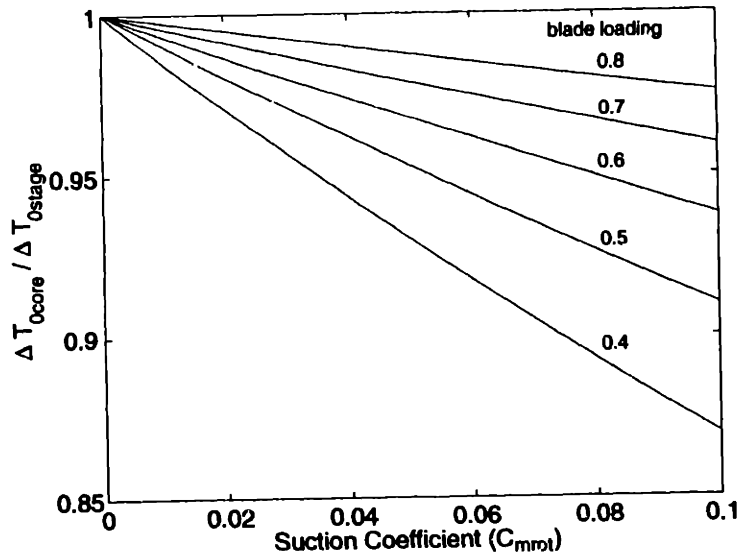

Figure 3-4: Variation of efficiency ratio with suction coefficient for various blade loading parameters. Assumes radial discharge of suction flow.

ing the suction mass flow from the tip will be lower for low tip speed designs.

3.3.2 Systems Study

A preliminary systems study of integrating the high-speed stage into an engine was performed by Allied Signal [45] and Pratt & Whitney [37]. These studies include the effect of suction discussed above and also provide preliminary assessment of other system effects. Both studies indicate that the suction mass flow requirement and management of the suction flow are the primary driving factors which determine feasibility of using aspiration due to their effect on overall engine efficiency. The impact of reducing engine weight, manufacturing, and life cycle cost have also been included in the study.

Chapter 4

Design System and Methodology

This chapter describes the suite of design and analysis codes, and the manner in which they were utilized to design the compressor stages. The through-flow calculations were carried out using two codes: the first code is based on solving the axisymmetric Euler equations on a fixed grid, similar to the approach of Hirsch [18] and Damle [6]. The second code named MTFLOW uses a streamline grid approach based on the ISES formulation [10] and is currently being developed by Drela. The axisymmetric Euler code was used exclusively for analysis purposes once the blade geometry was available after one design iteration. The blade geometry was decomposed into camber line and thickness and used as input to the axisymmetric Euler code which served as a comparison to the MTFLOW solution calculated using only prescribed swirl. The effect of endwall boundary layers, spanwise mixing, and non-axisymmetric effects which require additional modeling and empirical input were not included in either code. The quasi 3-D calculations were carried out using the inviscid-viscous interacting cascade code MISES. The blade sections forming the three dimensional blade geometry were analyzed and designed using this code. Three-dimensional inviscid analyses of the blade geometries were carried out using a modified version of the external aerodynamic unstructured grid Euler solver FELISA, and the three dimensional viscous analyses were performed by researchers at NASA Glenn Research Center using the APNASA code.

The coordinate system and flowfield non-dimensionalization are described first followed by a statement of the three-dimensional Euler equations in a rotating frame of reference which are the basis of the through-flow and three-dimensional inviscid codes. This is followed by descriptions of the different solvers comprising the design system. Finally, the overall stage design methodology is presented.

4.1 Coordinate System

Both Cartesian and cylindrical coordinate systems have been utilized in the computational modeling presented in this thesis. A cylindrical coordinate system is convenient due to the inherent nature of a turbomachinery flow field, however, a Cartesian system is preferred in some cases due its generality. Figure 4-1 illustrates these coordinate systems. The axis of the compressor flowpath is aligned with the x coordinate axis with the flow direction

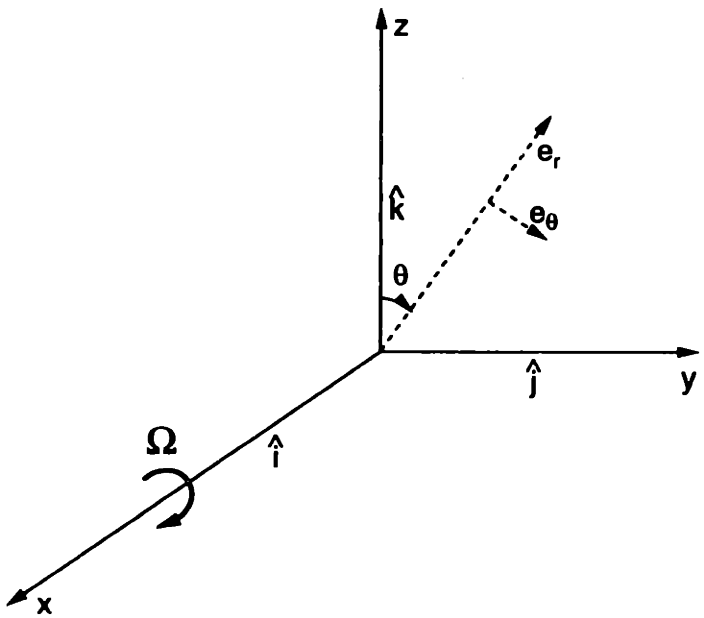

Figure 4-1: Cartesian and cylindrical coordinate systems.

corresponding to the positive x direction, and the origin of the coordinate system is located at the hub leading edge of the rotor. With reference to Figure 4-1 the following relationships

apply:

$$
\begin{aligned}
y &= r\sin\theta \\
z &= r\cos\theta \\
r &= \sqrt{y^2+z^2} \\
\theta &= \arctan\left(\frac{y}{z}\right) \\
\hat{e}_r &= \frac{y\hat{j}+z\hat{k}}{r} \\
\hat{e}_\theta &= \frac{z\hat{j}-y\hat{k}}{r}
\end{aligned}
$$

The absolute and relative velocities are related by the following

$$
\begin{aligned}
\vec{V} &= \vec{W}+\vec{\Omega}\times\vec{r} \qquad (4.1) \\
\vec{\Omega}\times\vec{r} &= \Omega r\,\hat{e}_\theta \\
\vec{\Omega} &= -\Omega\hat{i}
\end{aligned}
$$

where Ω is the blade angular velocity. The Cartesian and cylindrical velocity components are related by the transformation

$$
\begin{Bmatrix} V_x \\ V_r \\ V_\theta \end{Bmatrix} = \begin{bmatrix} 1 & 0 & 0 \\ 0 & \hat{y} & \hat{z} \\ 0 & \hat{z} & -\hat{y} \end{bmatrix} \begin{Bmatrix} V_x \\ V_y \\ V_z \end{Bmatrix} \qquad (4.2)
$$

where $\hat{y}$ and $\hat{z}$ are the coordinate directions normalized by r.

4.2 Reference Quantities

A non-dimensional form of the governing equations is preferable so that the numerical implementation is simpler, the possibility of an error due to inconsistent units is eliminated, and transfer of data and geometry across codes becomes an easier task. The inlet stagnation density and speed of sound are selected as reference quantities and are set to unity. Once a reference Mach number is specified then all the static quantities and velocities can be calculated using isentropic relations. The reference length used to non-dimensionalize the geometry is the rotor inlet tip radius. The primary and derived reference quantities are presented below.

$$\rho_{0\text{inl}} = 1 \qquad a_{0\text{inl}} = 1 \qquad L_{\text{ref}} = R_{\text{tip}} = 1$$

$$\begin{aligned} p_{0\text{inl}} &= \left(\rho_{0\text{inl}} a_{0\text{inl}}^2\right)/\gamma &&= 1/\gamma \\ H_{\text{inl}} &= a_{0\text{inl}}^2/(\gamma - 1) &&= 1/(\gamma - 1) \\ s_{\text{inl}} &= p_{0\text{inl}}/\rho_{0\text{inl}}^{\gamma} &&= 1/\gamma \\ \gamma &= c_p/c_v \end{aligned}$$

The wheel speed of rotating blade rows is specified in terms of a Mach number based on inlet stagnation speed of sound and reference length

$$\Omega = \frac{a_{0\text{inl}} M_{b0}}{L_{\text{ref}}}$$

where M_{b0} can be calculated from the actual blade speed and stagnation speed of sound based on standard or other appropriate inlet conditions.

4.3 Governing Equations

The Euler equations in a Cartesian coordinate system rotating at a constant speed Ω can be expressed as

$$\frac{\partial \vec{U}}{\partial t} + \frac{\partial \vec{F}}{\partial x} + \frac{\partial \vec{G}}{\partial y} + \frac{\partial \vec{H}}{\partial z} = \rho \vec{Q} \tag{4.3}$$

where $\vec{U}$ is the state vector, $\vec{F}$, $\vec{G}$, and $\vec{H}$ are the flux vectors, and $\vec{Q}$ is the source term of centrifugal and Coriolis forces.

$$\vec{U} = \begin{pmatrix} \rho \\ \rho W_x \\ \rho W_y \\ \rho W_z \\ \rho E \end{pmatrix}, \vec{F} = \begin{pmatrix} \rho W_x \\ \rho W_x W_x + p \\ \rho W_x W_y \\ \rho W_x W_z \\ \rho W_x I \end{pmatrix}, \vec{G} = \begin{pmatrix} \rho W_y \\ \rho W_y W_x \\ \rho W_y W_y + p \\ \rho W_y W_z \\ \rho W_y I \end{pmatrix}, \vec{H} = \begin{pmatrix} \rho W_z \\ \rho W_z W_x \\ \rho W_z W_y \\ \rho W_z W_z + p \\ \rho W_z I \end{pmatrix}$$

$$\vec{Q} = -\left(2\vec{\Omega} \times \vec{W}\right) - \left(\vec{\Omega} \times \vec{\Omega} \times \vec{r}\right) = \begin{pmatrix} 0 \\ 0 \\ \Omega^2 y - 2\Omega W_z \\ \Omega^2 z + 2\Omega W_y \\ 0 \end{pmatrix} \tag{4.4}$$

The total rotary internal energy is given by

$$E = e + \frac{1}{2}(W_x^2 + W_y^2 + W_z^2) - \frac{1}{2}\Omega^2 r^2 , \tag{4.5}$$

where $e = c_v T$ is internal energy per unit mass, and c_v is the specific heat at constant volume for a calorically perfect gas. The static pressure is related to the total energy, density,

and velocity components by

$$p = (\gamma - 1)\rho\left(E - \frac{1}{2}(W_x^2 + W_y^2 + W_z^2) + \frac{1}{2}\Omega^2 r^2\right) , \tag{4.6}$$

where the perfect gas assumption and constant specific heat ratio $\gamma = c_p/c_v$ have been applied. The rothalpy, or rotary stagnation enthalpy, is given by

$$I = E + \frac{p}{\rho} , \tag{4.7}$$

and is related to absolute stagnation enthalpy H through the equation

$$I = H - \vec{V} \cdot \left(\vec{\Omega} \times \vec{r}\right) . \tag{4.8}$$

The Euler equations need to be supplemented with appropriate boundary conditions at solid walls and at the domain farfield. At a solid wall, the relative velocity component, or alternatively the mass flux, normal to the wall must be zero. For turbomachinery flowfields, the farfield corresponds to the inlet and outlet planes of the flowpath containing the blade rows of interest. The appropriate boundary conditions at the inlet and exit are based on the propagation velocities of the characteristics, or Riemann invariants, derived from the characteristic from of the Euler equations. A detailed treatment of farfield boundary conditions can be found in Hirsch [17] and Giles [12].

4.4 Through-Flow Analysis

4.4.1 Axisymmetric Euler Solver

4.4.1.1 Governing Equations

The steady axisymmetric Euler equations can be derived by density averaging equations (4.3) and (4.4) in the circumferential direction after discarding the time derivative, as described by Hirsch [18]. The circumferential and density averages for any quantity A can

be defined as

$$\begin{aligned}\overline{A} &= \frac{1}{\theta_2-\theta_1}\int_{\theta_1}^{\theta_2} A d\theta \\ \hat{A} &= \frac{\overline{\rho A}}{\overline{\rho}} = \frac{\int_{\theta_1}^{\theta_2} \rho A d\theta}{\int_{\theta_1}^{\theta_2} \rho d\theta}\end{aligned} \tag{4.9}$$

where $\theta_2-\theta_1$ is a function of x and r, and covers the angular extent of the passage including the blade thickness and displacement effect of viscous boundary layers.

Applying this to the continuity equation gives

$$\frac{\partial}{\partial r}\left(rB\bar{\rho}\hat{V}_r\right) + \frac{\partial}{\partial x}\left(rB\bar{\rho}\hat{V}_x\right) = 0\,. \tag{4.10}$$

The fractional reduction in flow area $B(x,r)$, or blockage, arising from the blade thickness and boundary layer displacement thickness is defined as

$$B = 1 - \frac{t+\delta^*}{(2\pi r)/N_b} \tag{4.11}$$

where t is the blade thickness, δ^* is the total displacement thickness in the blade passage, and N_b is the number of blades. Similarly, the averaged momentum and energy equations are

$$\begin{aligned}\frac{\partial}{\partial r}\left(rB\bar{\rho}\hat{V}_r\hat{V}_r\right) + \frac{\partial}{\partial x}\left(rB\bar{\rho}\hat{V}_x\hat{V}_r\right) + \frac{\partial}{\partial r}\left(rB\hat{p}\right) &= rB(\hat{p}+\rho V_\theta^2) + r\hat{p}\frac{\partial B}{\partial r} \\ &+ \vec{F}_b\cdot n_{br}\end{aligned} \tag{4.12}$$

$$\frac{\partial}{\partial r}\left(rB\bar{\rho}\hat{V}_r\hat{V}_\theta\right) + \frac{\partial}{\partial x}\left(rB\bar{\rho}\hat{V}_x\hat{V}_\theta\right) + B\bar{\rho}\hat{V}_r\hat{V}_\theta = \vec{F}_b\cdot n_{b\theta} \tag{4.13}$$

$$\frac{\partial}{\partial r}\left(rB\bar{\rho}\hat{V}_r\hat{V}_x\right) + \frac{\partial}{\partial x}\left(rB\bar{\rho}\hat{V}_x\hat{V}_x\right) + \frac{\partial}{\partial x}\left(rB\hat{p}\right) = r\hat{p}\frac{\partial B}{\partial r} + \vec{F}_b\cdot n_{bx} \tag{4.14}$$

$$\frac{\partial}{\partial r}\left(rB\bar{\rho}\hat{V}_r\hat{H}\right) + \frac{\partial}{\partial x}\left(rB\bar{\rho}\hat{V}_x\hat{H}\right) = \Omega r\left(\vec{F}_b\cdot\vec{\hat{V}}\right)\,. \tag{4.15}$$

The static pressure $\hat{p}$ is defined in terms of the absolute stagnation enthalpy $\hat{H}$ and velocity $\vec{\hat{V}}$. The blade force $\vec{F}_b$ includes the effect of pressure and viscous shear stresses, and $\vec{n}_b$ is a unit vector normal to the blade camber line. The axisymmetric equations are solved in the absolute frame of reference, and rotating or stationary blade rows are distinguished by the magnitude of the blade angular velocity Ω.

4.4.1.2 Blade Forces

The forces due to the presence of a blade row are composed of a pressure force acting normal to the blade surface and viscous shear force acting tangential to the blade surface. The effect of blade thickness is reflected in the blockage term but the blade force term is non-zero when swirl is introduced into the flow due to blade camber. The pressure force can be determined once the blade camber line or alternatively the swirl distribution is known. The shear force requires empirical input and was not implemented. The equation of the blade camber surface and normal are

$$\alpha = \theta - f(r,x) \tag{4.16}$$

$$\vec{n}_b = \frac{\nabla\alpha}{|\nabla\alpha|} . \tag{4.17}$$

Since the pressure force acts normal to the camber surface it can be expressed as

$$\vec{F}_b = |\vec{F}_b|\nabla\alpha \tag{4.18}$$

which can be substituted in the circumferential momentum equation (4.13) to solve for the magnitude of the blade force.

$$|\vec{F}_b| = \frac{1}{r}\nabla\cdot\left(rB\bar{\rho}\vec{\hat{V}}(r\hat{V}_\theta)\right) . \tag{4.19}$$

4.4.1.3 Boundary Conditions

The solid wall boundary condition $\vec{V} \cdot \vec{n}_w$ is applied along the flowpath profiles where $\vec{n}_w$ is the unit normal to the flowpath. This is replaced by $\vec{W} \cdot \vec{n}_b$ on the blade camber surface, where $\vec{n}_b$ is the unit normal to the camber surface defined in (4.17), and $\vec{W}$ is the relative velocity. The boundary condition on the blade camber line can be used to solve

$$r\hat{V}_\theta = r^2 \left(\Omega + \hat{V}_r \frac{\partial f}{\partial r} + \hat{V}_x \frac{\partial f}{\partial x} \right) \tag{4.20}$$

for the blade camber line $f(r, x)$ when the swirl $\hat{V}_\theta$ is prescribed.

4.4.1.4 Numerical Implementation

The governing equations are discretized in conservative form using a finite-volume approach with a Van Leer flux vector splitting scheme [56] on a structured grid. Second order spatial accuracy is achieved by linear extrapolation of the solution from neighboring cells. Flux limiting was not required due to subsonic through-flow Mach numbers. The discrete equations were solved using a global Newton method with SPARSKIT routines [42] and GMRES [43] to handle the linear matrix solve.

4.4.2 MTFLOW

4.4.2.1 Code Description

In MTFLOW, only the momentum equations are discretized in a strong conservative form on a meridional streamline grid. The streamwise momentum equation has the form

$$dp + \rho q dq + \frac{\rho V_\theta}{r} \left[d(rV_\theta) - V_\theta dr \right] + p d(\Delta S) - \rho d(\Delta H_b) = 0 \tag{4.21}$$

where q is the meridional velocity $\sqrt{V_x^2 + V_r^2}$, and the differentials $d()$ are taken along a streamline. The normal momentum is used to impose pressure continuity along neighbor-

ing streamlines. The stage work is defined as

$$\Delta H_b \equiv \int \Omega \, d(rV_\theta) \tag{4.22}$$

where rV_θ is prescribed and Ω is non-zero for rotating blade rows. The entropy is defined as

$$S \equiv \ln\left[\frac{(h/h_{\text{inl}})^{\gamma/(\gamma-1)}}{p/p_{\text{inl}}}\right] \tag{4.23}$$

so that $S_{\text{inl}} = \ln(1) = 0$ by definition, and ΔS is the prescribed entropy variation along a streamline. The differential energy equation is not solved but instead the total enthalpy H is explicitly prescribed at every point in the flowfield using the relation

$$H = h_{\text{inl}} + \tfrac{1}{2}q_{\text{inl}}^2 + \Delta H_q + \Delta H_b \tag{4.24}$$

where ΔH_q may be due to heat addition. The total enthalpy is related to the static enthalpy and all velocity components as follows.

$$H \equiv h + \tfrac{1}{2}V_z^2 + \tfrac{1}{2}V_r^2 + \tfrac{1}{2}V_\theta^2 = h + \tfrac{1}{2}q^2 + \tfrac{1}{2}V_\theta^2 \tag{4.25}$$

With these definitions, the streamwise momentum equation (4.21) above can be manipulated into an entropy-convection equation with the imposed source terms due to heat addition and adiabatic loss.

$$-p\,dS + p\,d(\Delta S) + \rho\,d(\Delta H_q) = 0 \tag{4.26}$$

Equation (4.26) can optionally replace the momentum equation (4.21) in all or part of the flowfield, and preferable since it eliminates the generation of spurious entropy due to numerical errors. Finally, continuity is enforced by prescribing equal mass fractions of the total mass flow in each streamtube. The meridional speed q can be solved from

$$q = \frac{\dot{m}}{\rho A B} \tag{4.27}$$

where A is the cross-sectional thickness of the streamtube, and B is the blockage defined in (4.11) which acts to restricts the flow area.

The discrete equations described above are arranged in a form where the unknowns are the change in density and streamline positions, and the non-linear system is solved using a global Newton method. A particular advantage of this approach is that the streamline positions are simultaneously calculated as part of the solution and no explicit iteration is required to update the streamline positions as in traditional streamline curvature codes making MTFLOW computationally inexpensive and extremely robust.

4.4.2.2 Parameter and Geometry I/O

The geometry input requires the flowpath definition which includes profiles of the hub and casing. The meridional projection of all the blade rows in the flowpath are also required to determine the axial extent of the prescribed distributions. The wheel speed is specified for each blade row along with the number of blades per blade row. The circulation rV_θ, blockage B, and adiabatic loss ΔS are specified as spanwise profiles along the trailing edge of a blade row, and an assumed mode shape is used to determine the variation within the blade row. The prescribed quantities, which are a function of the meridional blade geometry, are transferred on to the corresponding streamlines which intersect the blade during the grid generation phase.

The geometric output from MTFLOW consist of streamline thickness and position in the meridional plane. A streamline, or a group of streamlines, within specified axial limits, for example on either side of a blade row, are output in terms the total streamtube thickness $b(m')$, average and radial position $r(m')$ where m' is the meridional arc length along the streamtube. Radial profiles of flow conditions such as absolute and relative Mach numbers, flow angles, and wheel speed in the relative frame can also be extracted from any point in the flow field.

4.5 MISES

4.5.1 Code Description

MISES is a quasi 3-D design and analysis code for turbomachinery cascades. The steady two dimensional Euler equations obtained by projecting the 3-D equations on an axisymmetric streamsurface of varying radius and thickness are solved. The equations discretized on a streamline grid in conservative form are used to represent the inviscid flow field. The formulation is similar to MTFLOW and also has the option of replacing the standard momentum equation by the entropy convection equation. The viscous effects on the cascade surface and in the wake are modeled by a two-equation integral boundary layer formulation coupled to the inviscid flow field by the displacement thickness concept. Closure of the boundary layer equations is achieved through relations for the skin friction, dissipation, and energy thickness derived from a two parameter family of velocity profiles. In addition, the laminar formulation uses an e^9 and bypass transition models, and the turbulent formulation includes a shear stress lag equation to model upstream history effects of non-equilibrium boundary layers. The fully-coupled system of non-linear equations is solved simultaneously by a global Newton-Raphson method. Further details of the code are given in [64] and [65].

The streamline based formulation of the code is well suited for inverse design methods. The interactive inverse design capabilities of the code are summarized in the table below. In the mixed-inverse mode, the desired blade surface pressure distribution is prescribed

Method	Geometry Description	Solution Method
Mixed-Inverse	Pointwise (arbitrary shape)	require $p(s) = p_{\text{spec}} + \ldots$
Modal-Inverse	Surface-normal displacement modes	minimize $\int (p - p_{\text{spec}})^2 \, ds$

Table 4.1: Inverse Design Features

over a segment of the blade. The prescribed pressure constraint is satisfied by perturbing the blade shape locally on a node by node basis over the target segment. The constraint

of preserving camber or thickness of the blade in the target segment can also be imposed. The mixed-inverse method is useful in eliminating local aerodynamic defects in the blade shapes. The modal-inverse on the other hand matches the target pressure in a least-squares sense. The change in the blade shape is defined in terms normal displacement amplitudes and suitable mode shapes. A least squares procedure is used to drive the mode amplitudes until the difference between the specified pressure distribution and computed pressure distribution is minimized.

4.5.2 Suction Model

The suction model developed for the multi-element code MSES [35] was implemented in MISES. Three aspects of the integral boundary layer formulation were modified to model the effects of suction. Accounting for the suction mass flux leads to additional terms in the integral momentum equation and kinetic energy equation. The compressible forms used in MISES are given below.

$$\frac{d\theta}{ds} + (2 + H - M_e^2)\frac{\theta}{u_e}\frac{du_e}{ds} = \frac{C_f}{2} + \frac{\rho_w v_w}{\rho_e u_e} \tag{4.28}$$

$$\theta\frac{dH^*}{ds} + (2H^{**} + H^*(1 - H))\frac{\theta}{u_e}\frac{du_e}{ds} = \left(2C_D + \frac{\rho_w v_w}{\rho_e u_e}\right) - H^*\left(\frac{C_f}{2} + \frac{\rho_w v_w}{\rho_e u_e}\right) \tag{4.29}$$

The slot is treated as a porous surface with no slip conditions giving only the normal transpiration term.

The turbulent skin friction is modified by the addition of a parametric effect of the transpiration velocity to correctly predict the increase in shear stress near the wall.

$$C_f = C_{f0} - 2\frac{\rho_w v_w}{\rho_e u_e}U_s \tag{4.30}$$

Here, C_{f0} is the skin friction coefficient without suction, $\rho_w v_w/\rho_e u_e$ is the transpiration term, and U_s is a turbulent wake layer slip velocity. It is interesting to note that the effect of adding $(\rho_w v_w/\rho_e u_e)U_s$ to the skin friction is identical to assuming a non-zero velocity tangential to the slot, and in this case the tangential velocity u_w is the same as U_s. The

turbulent dissipation relation used in the code consists of contributions from the inner and outer layer

$$C_D = \frac{C_f}{2} U_s + C_\tau (1 - U_s) \tag{4.31}$$

where C_D is the dissipation coefficient, C_f is the usual skin friction coefficient without suction, and C_τ is a lagged turbulent shear stress coefficient. The contribution from the inner layer appears in the skin friction term. The dissipation relation is conveniently modified for suction by substituting the modified skin friction (4.30) giving

$$C_D = \frac{C_{f0}}{2} U_s - \frac{\rho_w v_w}{\rho_e u_e} U_s^2 + C_\tau (1 - U_s) \, . \tag{4.32}$$

Finally, the viscous-inviscid coupling condition is modified using continuity to include the suction mass flux. The new coupling condition is

$$\Delta n = \delta^* + \frac{1}{\rho_e u_e} \int_0^s \rho_w v_w ds \tag{4.33}$$

where Δn is the displacement of the inviscid surface streamline.

Reference [35] shows comparisons between the predictions of this suction model and experimental data for a variety of low speed and transonic airfoils. Hence, the model is expected to be reliable for applications to low-speed and high-speed cascades.

Suction can be included in a MISES calculation by specifying the location and extent of the suction slot on the blade surface and the magnitude in terms of the suction coefficient C_m. The suction coefficient is converted into the transpiration mass flux $\rho_w v_w$ by expressing $\rho_w v_w$ in terms of an amplitude and mode shape

$$\rho_w v_w = \overline{\rho_w v_w} f(s) \, . \tag{4.34}$$

The mode shape currently implemented and used for the calculations presented in this

thesis is parabolic within the slot and 0 everywhere else.

$$f(s) = \begin{cases} 4\dfrac{(s-s_1)(s_2-s)}{(s_2-s_1)^2} & s_1 \le s \le s_2 \\ 0 & s < s_1 \ , \ s > s_2 \end{cases} \tag{4.35}$$

This expression can be substituted into the definition of the suction coefficient (3.1) to solve for $\overline{\rho_w v_w}$

$$\overline{\rho_w v_w} = -\frac{C_m \dot{m}_{\text{inl}}}{\int_{s_1}^{s_2} f(s)\, ds} \ . \tag{4.36}$$

The slot location and suction coefficient are specified through an input file and can be easily modified by the user.

An example of a MISES grid is shown in Figure 4-2. The surface streamline displaced due to the presence of the boundary layer and the localized effect of suction on the external inviscid stream are also seen.

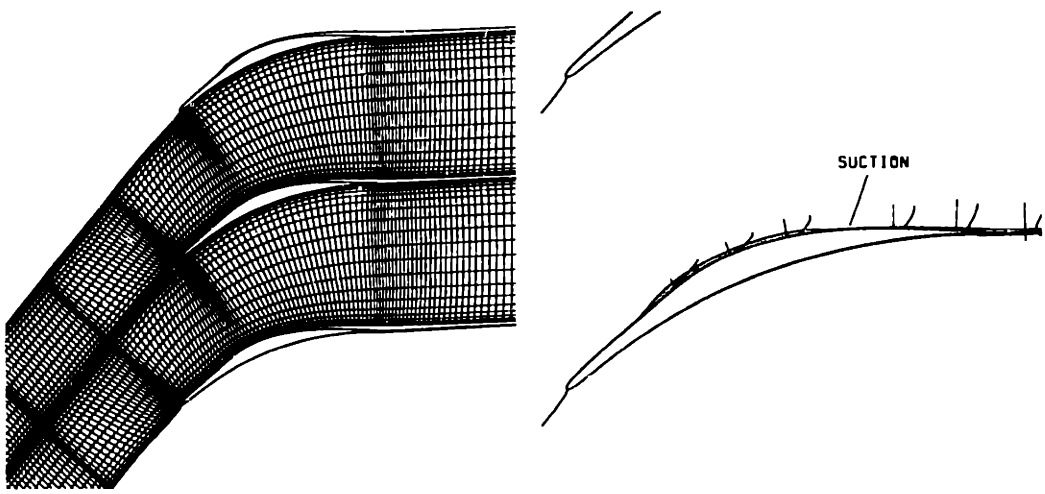

(a) Grid (b) Effect of suction on inviscid streamline

Figure 4-2: Example of a MISES grid.

4.5.3 Parameter and Geometry I/O

The two-dimensional blade section is defined in the standard $m' - \theta$ streamsurface coordinate system. The variation of streamsurface radius and thickness are needed in order to capture the quasi 3-D effects are specified as functions of m'.

The required flow conditions will depend on the type of boundary conditions imposed in the calculation. As MISES was used in conjunction with the through-flow codes, the inlet and exit conditions were taken from the axial limits of the streamlines extracted from the through-flow calculation. For subsonic relative flow, the relative Mach number and flow angle are imposed and for supersonic relative flow the inlet swirl and exit pressure are imposed. In addition, there are leading edge and trailing edge Kutta conditions which are unique to the streamline formulation of the code. Additional adiabatic loss increment can also be specified if required.

The output from the MISES calculation is the blade to blade flow field from which important exit quantities such as Mach number, flow angles, pressure rise, blockage, shock and viscous losses can be obtained by a suitable averaging procedure. These can serve as inputs to the through-flow calculation. The blade geometry in Cartesian coordinates can be obtained from the $m' - \theta$ definition and streamsurface information.

4.6 Three-Dimensional Inviscid Analysis

An extension of the three-dimensional unstructured grid code FELISA developed by Peraire [39, 38] was used to calculate three-dimensional flow solutions for the compressor designs. FELISA is a finite-element based code which solves the conservative Euler equations on unstructured tetrahedral grids. The equations are spatially discretized by an approximate variational formulation with explicit addition of a matrix form of artificial viscosity. The solution is advanced in time using a multi-stage time stepping scheme.

To allow calculation of flow through rotating blade rows the Euler equations have to be expressed in a relative frame of reference rotating with the blade rows. The flow is only

calculated in one blade passage with periodic boundary conditions. The inflow boundary condition was modified to allow specification of arbitrary total pressure, total temperature, and flow angle profiles. The outflow boundary condition was modified to allow specification of exit pressure and radial equilibrium is used to set the radial pressure profile. The implementation of artificial viscosity was also modified to allow solid body rotation of the flow without excessive dissipation. The modifications and extension to the code are described in detail below.

4.6.1 Modified Euler Equations

The initial implementation of the Euler equations (4.4) detailed above led to unsatisfactory solutions for a simple test case of rotating flow in a circular duct with uniform axial absolute velocity. Deceleration of the axial velocity was observed from inlet to exit of the duct along with deceleration of the relative rotating flow. The cause was traced to conservation errors due to discretization of the source terms, excessive numerical dissipation due to gradients in the relative flow, and boundary conditions on the walls of the duct.

The problem was circumvented by deriving an alternate form of the momentum equations where the relative velocity in the state vector is replaced with the absolute velocity.

$$\frac{\partial}{\partial t}\rho\left(\vec{V}-\vec{\Omega}\times\vec{r}\right)+\nabla\cdot\left(\rho\vec{W}\left(\vec{V}-\vec{\Omega}\times\vec{r}\right)\right)+\nabla p=-\left(2\rho\,\vec{\Omega}\times\vec{W}\right)-\left(\rho\vec{\Omega}\times\vec{\Omega}\times\vec{r}\right)$$

After simplifying the above equation, the final equivalent form of the Euler equations are:

$$\begin{aligned}\frac{\partial\rho}{\partial t}+\nabla\cdot\left(\rho\vec{W}\right) &= 0\\ \frac{\partial\left(\rho\vec{V}\right)}{\partial t}+\nabla\cdot\left(\rho\vec{W}\vec{V}\right)+\nabla p &= -\rho\vec{\Omega}\times\vec{V}\\ \frac{\partial\left(\rho E\right)}{\partial t}+\nabla\cdot\left(\rho\vec{W}I\right) &= 0.\end{aligned} \tag{4.37}$$

Note that the state vector now has absolute velocities and the relative velocity only appears in the convection term. The Coriolis force is in terms of the absolute velocity and vanishes

when $\vec{V} \equiv 0$, and the centrifugal force term is completely eliminated. This is equivalent to subtracting a solution corresponding to steady solid body rotation of the relative flow from the momentum equations, and since the absolute velocity field $\vec{V} \equiv 0$, the momentum equations are not affected. The discrete equations are derived by applying the Galerkin method to the weak variational form of the equations and finally rearranged in a form suitable for implementation in an edge based data structure.

4.6.2 Artificial Dissipation

The central Galerkin spatial discretization of the equations is unstable and requires the addition of an explicit artificial viscosity term. The FELISA formulation employs a dissipation which separately upwinds the convective and pressure fluxes using the edge normal Mach number to determine the proper domain of influence. The upwinded flux term can be expressed as

$$\mathcal{F}_e = F(U_1) + F(U_2) - f_1(M_e)a_e\Delta U^c - f_2(M_e)\Delta U^p \tag{4.38}$$

where U_1 and U_2 are the edge node state vectors, f_1 and f_2 are blending functions, and ΔU^c and ΔU^p are left and right state vector differences of the convective and pressure components of the state vector. In order to be consistent with the modifications made to the governing equations, the convective vector in the dissipation uses the absolute velocity $\vec{V}$, whereas M_e, and consequently the domain of dependence, is based on the relative velocity $\vec{W}$. Thus, the ΔU^c contribution to the momentum equations vanishes when there are no gradients in the absolute velocity field.

4.6.3 Boundary Conditions

The solid wall boundary condition enforces zero normal flow through the wall and is applied by eliminating the velocity component normal to the wall. For rotating blade rows this condition is expressed as

$$\vec{W} \cdot \vec{n_w} = 0 \,,$$

where $\hat{n_w}$ the unit vector normal to the wall. For the hub and casing walls, however, the absolute velocity is used as this condition is prone to numerical errors, especially if the wall normal is not computed accurately.

$$\vec{V} \cdot \vec{n_w} = \left(\vec{W} + \vec{\Omega} \times \vec{r}\right) \cdot \vec{n_w} = 0$$

An equivalent statement of the above condition is that the mass flux through the wall is zero and the only contribution to the momentum residual is due to pressure fluxes.

Inflow and outflow boundary condition are applied by using Roe's approximate Riemann solver to determine the nodal flux normal to the boundary.

$$F_i^n = \frac{1}{2}\left(F^n(U_i) + F^n(U_{\text{spec}})\right) - |\mathbf{A}\left(U_i, U_{\text{spec}}\right)|\left(U_{\text{spec}} - U_i\right) \tag{4.39}$$

where U_{spec} is the vector of specified inflow or outflow conditions, and $|\mathbf{A}\left(U_i, U_{\text{spec}}\right)|$ is Roe matrix evaluated in the direction normal to the boundary. Profiles of total enthalpy, entropy, axial and radial flow angles are specified at the inflow boundary. The exit pressure at the hub is prescribed at the outflow boundary and spanwise variation of the pressure is calculated using radial equilibrium condition

$$\Delta p \simeq \left(\frac{\rho v_\theta^2}{r}\right) \Delta r \tag{4.40}$$

where the swirl velocity from the most recent update of the solution is used. The pressure is set by sweeping in the spanwise direction starting from the hub.

Periodic boundary conditions are applied by summing the residuals of corresponding nodes on the periodic surface. This step is carried out once the residual vector is calculated over the entire domain but before the source term is added. The momentum residuals have

to be rotated by the pitch angle. The residuals on the left periodic surface are

$$\begin{pmatrix} R_\rho \\ R_x \\ R_y \\ R_z \\ R_E \end{pmatrix}_{\text{left}} = \begin{pmatrix} R_\rho \\ R_x \\ R_y \\ R_z \\ R_E \end{pmatrix}_{\text{left}} + \begin{bmatrix} 1 & 0 & 0 & 0 & 0 \\ 0 & 1 & 0 & 0 & 0 \\ 0 & 0 & \cos(\theta_P) & \sin(\theta_P) & 0 \\ 0 & 0 & \sin(\theta_P) & \cos(\theta_P) & 0 \\ 0 & 0 & 0 & 0 & 1 \end{bmatrix} \begin{pmatrix} R_\rho \\ R_x \\ R_y \\ R_z \\ R_E \end{pmatrix}_{\text{right}} \tag{4.41}$$

$$\text{where} \qquad \theta_P = \frac{2\pi}{\#\text{ of blades}}$$

Similarly, for the right periodic fluxes $-\theta_P$ is used in the transformation. The cell volumes associated with the periodic nodes have to be added, and the individual cell volumes are replaced by the total cell volume.

4.7 Three-Dimensional Viscous Analysis

The viscous calculations presented in this thesis were carried out using the APNASA code by Adamczyk and Celestina. The Reynolds averaged Navier-Stokes equations are discretized using a finite volume approach on structured hexahedral cells using a cell centered scheme. The two-equation standard $k-\epsilon$ model of Launder and Spalding is used to estimate the eddy viscosity. This is a high Reynolds number model which requires the use of wall functions at solid surfaces and is valid from the outer region of a turbulent boundary layer to the beginning of the log-layer. The dissipation scheme is a blend of second and fourth difference smoothing operators patterned after the model developed by Jameson, and a pressure switch is used at shocks and stagnation points to introduce stronger smoothing. The spatially discretized equations are marched in time using an explicit 4-stage Runge-Kutta algorithm. Boundary conditions at the inflow and outflow are

applied using Riemann conditions and solid wall conditions on the blade and casing. The mesh used is an H-type generated by applying a series of cubic spline fits to the geometry data of the flowpath and blade. Further details of the code can be found in Celestina [3]. The code uses a multi-stage model developed by Adamczyk [1] referred to as the average passage flow model to interact the blade rows at various stages in the flowpath.

4.8 Design Methodology

The overall stage design process is illustrated in Figure 4-3. The initialization of the de-

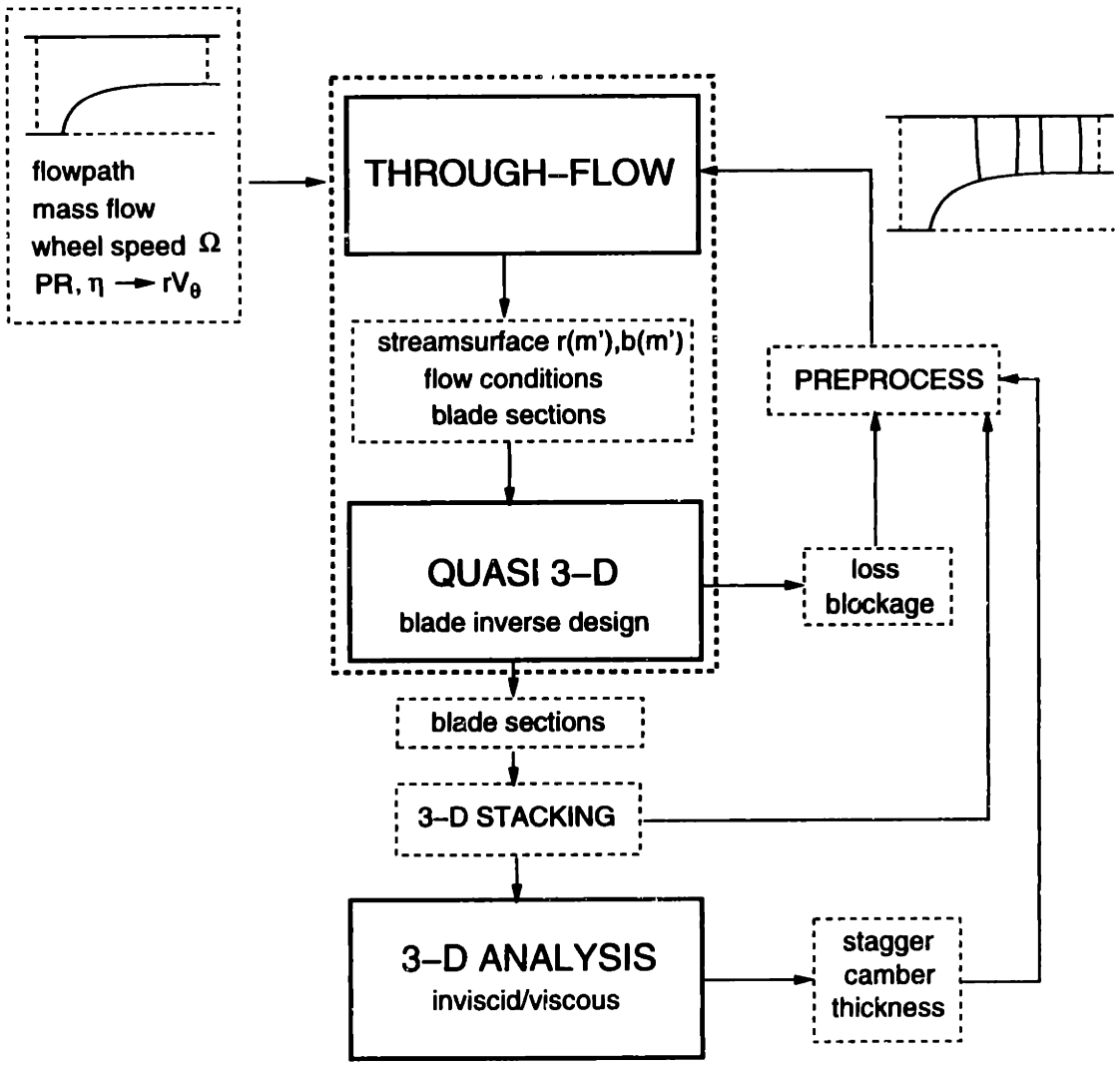

Figure 4-3: Design Data Flow

sign process begins with the specification of the flowpath, inlet mass flow, wheel speed, and work distribution which is calculated from the desired pressure ratio and assumed isentropic efficiency.

A relatively simple approach was used to construct the flowpath. The hub profile has a parabolic shape upstream of the rotor and is blended by matching the slope of the rotor ramp angle at the rotor leading edge. The hub section across the rotor is linear and is defined by a length depending on the rotor chord and ramp angle. The ramp angle is specified to maintain an axial velocity density ratio AVDR close to or greater than one. As this depends on the through-flow calculation the ramp angle may undergo some changes in the initial design cycles. The hub profile radius at the stator exit is also specified to maintain a reasonable AVDR across the stator. The profile from the linear ramp region

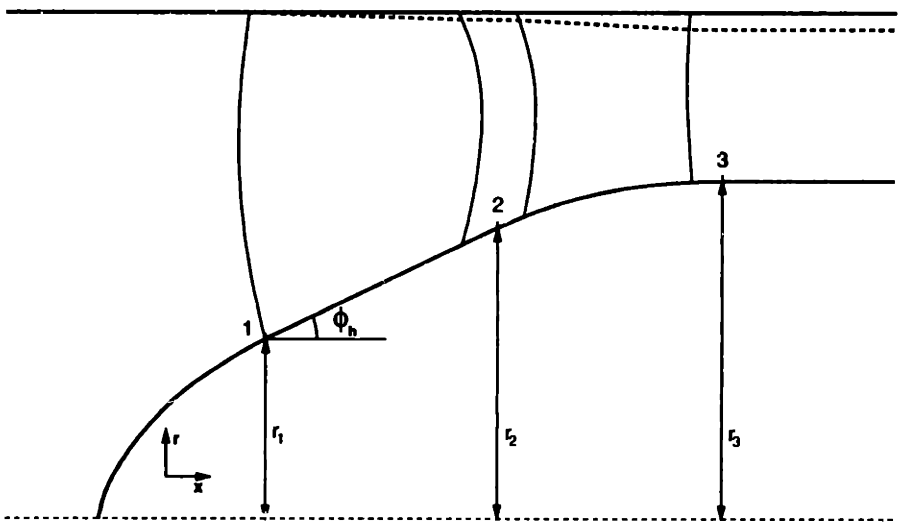

Figure 4-4: Flowpath Construction

is smoothly blended with a constant radius section downstream of the stator. The initial casing flowpath is specified as a constant radius section along the entire flowpath. A contraction across the rotor or stator can be specified with a linear profile across the contraction blended with the remaining flowpath to eliminate discontinuities in the slope of the profile. The flowpath construction is illustrated in Figure 4-4. The three locations and radii defining the hub profile are shown and the possible contraction of the tip profile is indicated by the dotted line.

The initial mass flow is specified as a design requirement, or alternatively could be determined as an outcome of the design process. In the later case, the mass flow could be specified to achieve reasonable flow angles and diffusion factors along the span and mainly at the tip section. This choice could be based on cascade data or preliminary velocity triangles at the hub, mid-span, and tip sections. The wheel speed is fixed at a specified value as a design requirement. The constant radial work distribution is initially calculated using the energy equation with the specified pressure ratio, assumed stage efficiency, and no inlet swirl.

$$\Delta r V_\theta = \frac{1}{\eta_{\text{stg}} M_{b0}} \left(\text{PR}^{\frac{\gamma-1}{\gamma}} - 1 \right)$$

Here, the reference quantities $a_{0\text{inl}} = 1$ and $R_{\text{tip}} = 1$ have been used. The swirl input $\Delta r V_\theta$ is adjusted during the design process as better estimates of efficiency/loss are available.

The through-flow calculation is executed with the inputs described above. In this early transient stage only the hub, mid-span, and tip streamlines are extracted. These are used in the quasi 3-D code to design blade shapes which are then stacked to give the three-dimensional geometry. It was found that including more than three streamlines early in the design phase led to excessive spanwise wiggles in the geometry. A meridional projection of the blade is supplied to the through-flow calculation to begin the next iteration. Now the meridional picture is somewhat well defined and rotor-stator spacing is adjusted to the to meet instrumentation requirements or some other constraints. The flowpath may also be redesigned to accommodate changes in axial length of the rotor and stator. The next through-flow calculation is performed and the new streamlines and flow conditions are extracted. This time additional streamlines between the hub and mid-span and mid-span and tip are used to give a total of 5 streamlines. The streamlines are used to extract blade section cuts from the three dimensional geometry and are converted into $m' - \theta$ coordinates. After redesign of the sections in MISES, a stacking of the new blade sections is used to update the three-dimensional geometry. The blockage and loss are now included in the information supplied to the through-flow solver. The process is repeated until convergence to a suitable geometry and agreement between the through-flow solution and quasi 3-D solutions is achieved. More streamlines may also be added into the design loop,

but 10 streamlines proved to be adequate for the designs presented in this thesis.

The three-dimensional codes were outside the main design loop described above. The inviscid calculation was used to examine the spanwise variation in the shock location. Radial profiles of swirl, static pressure rise, and total pressure rise were also compared with quasi 3-D sections. Comparison of the incidence angles with the quasi 3-D calculation proved to be a valuable output from the 3-D calculation, and this information was used to directly modify the stagger angle of the blade sections in the 3-D stacking.

The 3-D viscous calculation was also used in a similar manner. In addition, the viscous calculation provided valuable information on the 3-D effects due to the boundary layer and also confirmation of the suction requirement predicted by the quasi 3-D calculation. Impact of endwall boundary layers on the design was also obtained and suitable modifications were made in the quasi 3-D calculations. In addition the flow field between the rotor and stator provided a more realistic picture of the flow angles, loss, and blockage. These were used to improve the estimate of blockage use in the through-flow calculation. The suction location and suction quantity at the different locations on the flowpath were determined iteratively in the 3-D viscous calculation.

Chapter 5

Blade Section Design

Pressure rise in conventional compressor blades is achieved either by subsonic turning or deceleration of the flow through a shock but rarely a combination of both. Aspirated blades introduce the possibility of combining these two mechanisms to achieve a significantly higher pressure rise than conventional blades. The design of such blades is a much more challenging task since the performance of the high speed and low speed regions of the blade are more strongly coupled compared to conventional blades.

The design philosophy employed in this thesis is termed Blade Loading Management. This is further composed of two components: shock management and boundary layer management. The shock structure and strength can be manipulated by varying geometric parameters such as pitch in two dimensions, sweep and lean in three-dimensions [57],

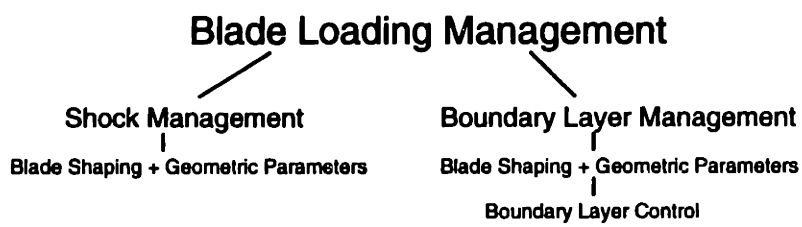

and by blade shaping. Boundary layer management is accomplished primarily by blade shaping and is assisted by control techniques such as suction or blowing. The distinction between shock and boundary layer management is made on the basis of the importance of

each of these as the driving factors in the design process in different speed regimes.

In the conventional design approach there is little interaction between shock management and boundary layer management concepts. Supersonic blades are designed primarily with the shock structure as the driving factor since there is minimal flow turning, and the blade geometry is very simple. This is also reflected in the design methods which exclusively use camber line manipulation, with the thickness distribution fixed by structural requirements. On the other hand, in the design of low-speed and supercritical blades achieving acceptable boundary layer behavior is the driving factor, and inverse design methods which directly manipulate the blade shape are preferred.

Integrating shock and boundary layer management is an essential ingredient in the aspirated blade designs presented in this thesis. Chapter 5 details how a blade is divided into six regions, each region shaped to meet certain design criteria. The geometric parameters characterizing a blade section are presented next followed by a description of the blade design procedure. Finally, The design features corresponding to the different regions of the blade are analyzed.

5.1 Geometric Parameters

The two-dimensional geometric parameters characterizing a blades are shown in Figure 5-1. The blade spacing or pitch is denoted by $s = 2\pi r/N_b$, where N_b is the number of blades. The leading edge radius r_{le} is the inverse of the curvature at the location defined as the leading edge. The chord line connects the leading edge and trailing edge points. The camber line is the average $\overline{y}$, and the thickness is the difference in the pressure and suction surface $\overline{y}$ defined in the chord-aligned coordinate system. The stagger ξ is the angle of the chord line with respect to the axial direction. The angle between the tangents of the suction and pressure surface at the trailing edge, θ_{te}, is also a useful parameter. A negative θ_{te} produces an open trailing edge which has been termed "diverging trailing edge" by Henne [16].

Although the location of the trailing edge is clear, the location of the leading edge in an

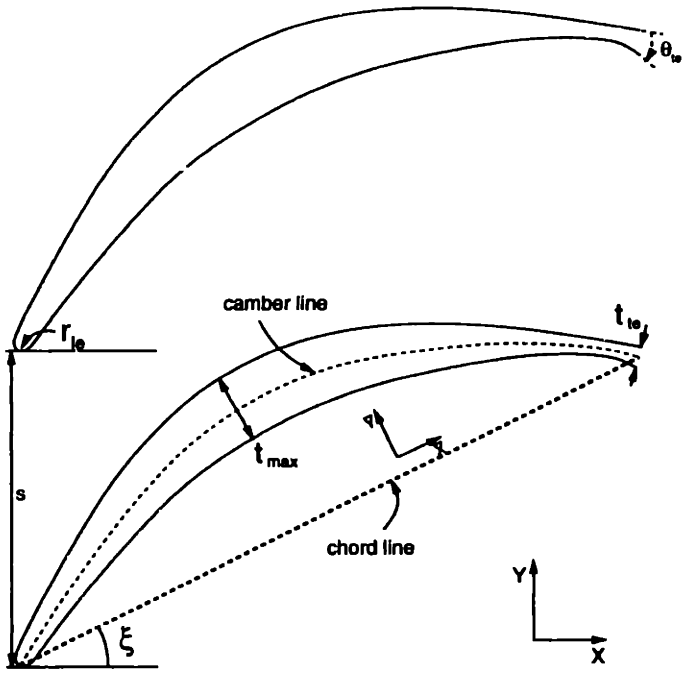

Figure 5-1: Blade profile geometric parameters.

arbitrary blade section is not clearly defined. One approach, the one used in this thesis, is that the leading edge point is the location where the tangent to the blade surface is perpendicular to the chord line. Another possible definition is the leading edge coincides with the location of maximum curvature. Neither of these are satisfactory for blades with large leading radii and camber and when the transition from the leading edge region to the rest of the blade is gradual.

5.2 Design Procedure

The design procedure is initiated with a seed geometry which undergoes gross parameter changes followed by an inviscid design and finally viscous design with the effects of boundary layer suction.

5.2.1 Initial Geometry

The initial blade geometry could be chosen in any number of ways. A blade section could be selected from a profile family or constructed using a suitable camber line and thickness distribution. The important considerations in the initial design phase are adjusting the stagger so that the prescribed flow angle is matched, adjusting the camber line to meet exit angle requirement, and adjusting solidity to meet estimated blade loading requirements. The initial geometry could also be obtained from a specified intersection of an existing three-dimensional geometry.

5.2.2 Inviscid Design

The inviscid design involves a piecewise modification of the inviscid pressure distribution of the initial geometry using the mixed-inverse design method in MISES. This is an intuitive process and relies on the experience of the designer. The two templates that characterize the prescribed pressure distribution for aspirated blades are illustrated in Figure

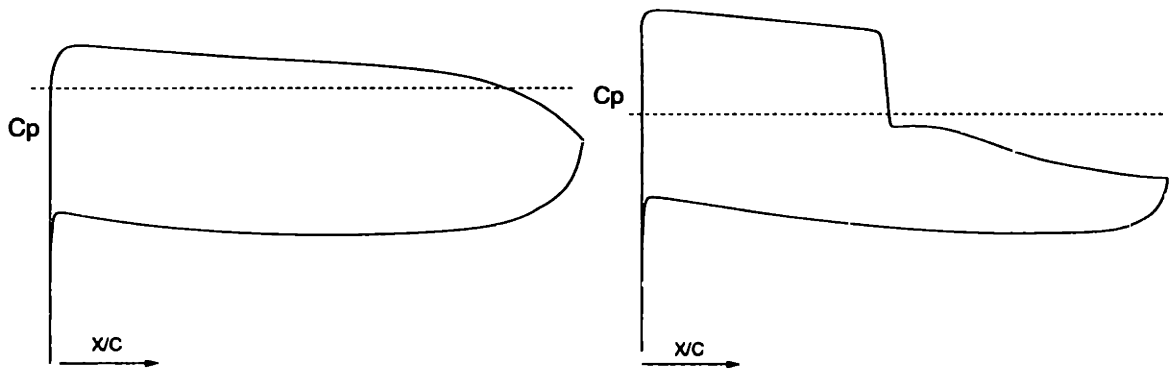

(a) Subsonic/Shockless Supercritical **(b)** Supersonic

Figure 5-2: Inverse design pressure templates

5-2. The dashed line indicates sonic condition. The subsonic/supercritical pressure distribution shows a smooth transition from stagnation point to the suction and pressure sides. A mild pressure gradient extends over most of the suction side followed by a relatively short pressure recovery region. The pressure side shows a uniform loading over the en-

tire side. The supersonic template also shows a smooth transition near the leading edge though the transition may be smaller depending on the leading edge radius. The suction surface has a weak pre-compression followed by the passage shock. Downstream or the shock the pressure is decreased to form a small plateau to allow the boundary layer to recover, and this is also where suction is applied. This is followed by the pressure recovery region. The pressure side has an adverse pressure gradient up to mid-chord followed by an almost constant pressure section up to the minimum thickness location just before the diverging trailing edge. The pressure distribution is closed by a strong acceleration of the flow at the diverging trailing edge. The pressure side may also have a shock if the blade is choked.

The geometric parameters such as stagger, maximum thickness, and camber are also fine tuned simultaneously. Inverse design is not a black-box procedure and very often produces blade shapes that have local kinks and wiggles. An example of this is specifying a pressure distribution which forces the shape across a shock. The resultant geometry will have a kink where compression and expansion waves are generated to satisfy the specified pressure distribution. Although the design point may show an acceptable pressure distribution, the off-design performance will most often be unacceptable, and direct geometry manipulation may be required to smooth out local features. The XFOIL program [7] was used to carry out direct modification of the blade shape.

5.2.3 Viscous Design

The viscous calculation is performed using the geometry from the inviscid design. The first step is to locate the suction slot and adjust the suction mass flow to obtain acceptable boundary layer behavior. At this point the suction mass flow may be high and will undergo refinement as the blade shape evolves. If the boundary layer is found to separate then the inviscid pressure distribution has to be redesigned. The inverse design routine will fail when applied to a region with a separated boundary layer. The procedure for viscous design is the same as the inviscid procedure described above. The inverse design cycles are combined with direct geometry design to clean up kinks and wiggles.

5.3 Design Features

5.3.1 Leading Edge

The motivation for focusing on the design of the leading edge region is that a poorly designed leading edge will result in large spikes in the pressure distribution which will adversely affect the downstream development of the boundary resulting in higher losses and smaller useful incidence range. In recent years more attention has been given to the leading edge in the context of controlled diffusion blading due to better blade representation and improved inverse design methods [50, 49]. However, this change has mainly affected blade design in the transonic inlet Mach number range and has not yet penetrated design procedures for supersonic blades where leading edge circles are used to close the thickness distribution [62].

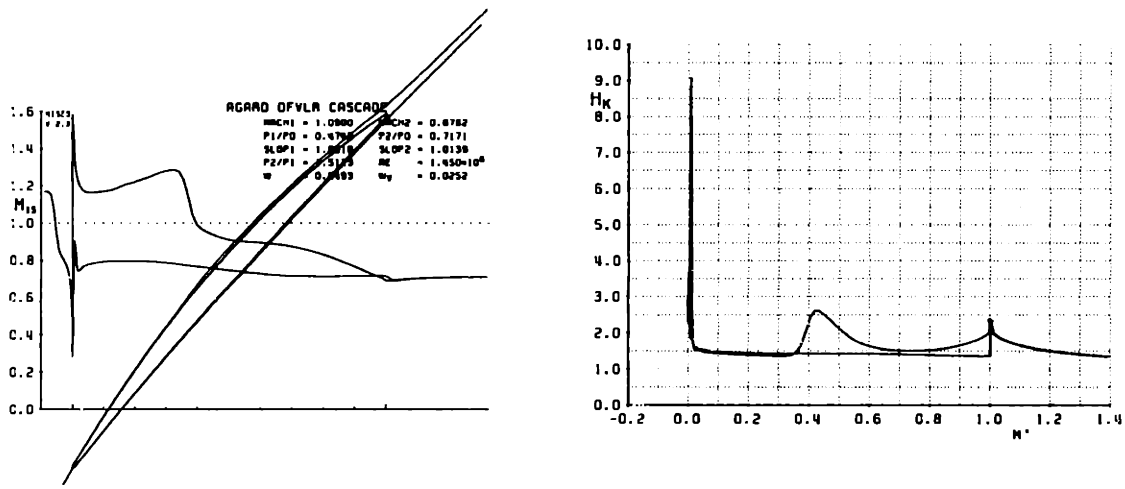

(a) Isentropic Mach Number

(b) Shape Parameter

Figure 5-3: Original DFVLR Cascade

The conventional leading edge design is illustrated with a DFVLR rotor cascade [15]. The cascade corresponds to a 45% span section from a rotor designed with multiple circular arc blades for a pressure ratio of 1.51 at a tip Mach number of 1.38. The cascade design Mach number and inlet angle are 1.09 and 58.5°, respectively. The original cascade has a circular

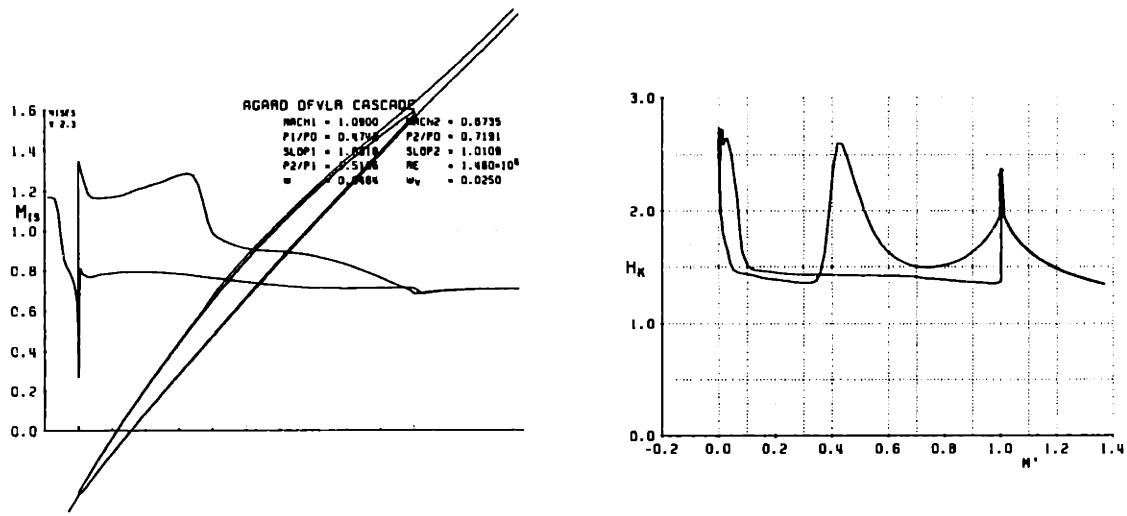

(a) Isentropic Mach Number

(b) Shape Parameter

Figure 5-4: Redesigned DFVLR Cascade

leading edge.

Figure 5-3 shows the isentropic Mach number distribution and corresponding boundary layer shape parameter distribution for the original cascade. A large spike in the Mach number is seen on the suction side near the leading edge and a relatively smaller one on the pressure surface. The suction surface spike can be alleviated by decreasing the inlet angle but this will exacerbate the spike on the pressure surface. The shape parameter on the pressure side also indicates separation near the leading edge. In contrast, Figure 5-4 shows the cascade redesigned with the present technique where the spike on the pressure surface has been virtually eliminated and the spike on the suction is considerably reduced. In fact, the spike on the suction side can also be completely eliminated. The shape parameter distribution also shows a significant improvement near the leading edge, and the separation bubble near the leading edge has been eliminated.

Figure 5-5 provides a closer view of the leading edge region of the original and redesigned cascades. The blending of the leading edge circle with the rest of the profile and a small increase in the thickness near the leading edge are clearly seen. In this case the blending

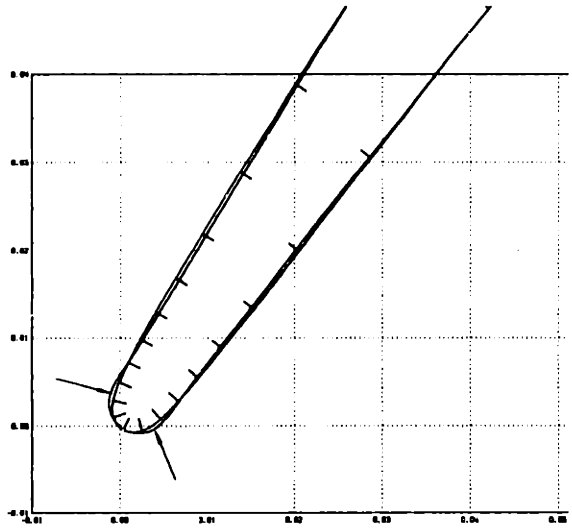

Figure 5-5: DFVLR Cascade redesigned leading edge. Arrows indicate original geometry with a circular leading edge.

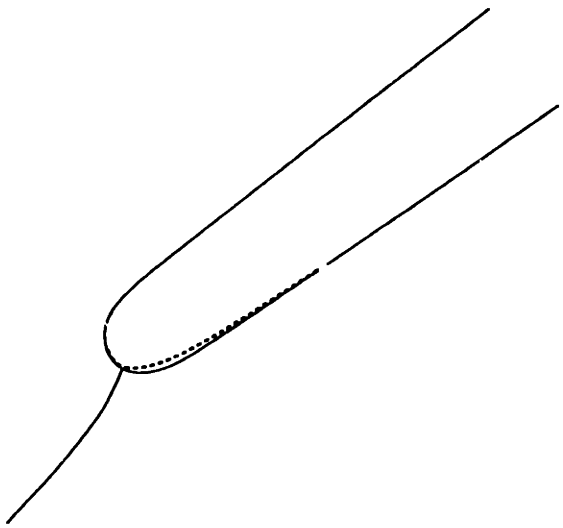

Figure 5-6: Pressure side leading edge blending. Dotted line is the blended shape after redesign.

is almost symmetric but in most cases where cascades operate with positive incidence blending on the pressure surface is more pronounced. This is schematically shown in Figure 5-6. Hence, the criterion for acceptable leading edge design is a smooth transition of the flow from the stagnation point to the suction and pressure surfaces.

One other aspect which must be considered is the thickness or radius of the leading edge. This must decrease in a systematic manner with increasing inlet Mach number to avoid

excessive shock loss due to leading edge bluntness. Leading edge shock loss models, such as the popular one presented by Koch and Smith [29], indicate that the loss scales as $t_{le}M_{in}^2$, but with a blended leading edge the shape of the leading edge must also be a factor. In the present approach, loss due to the leading edge thickness was directly available from the MISES calculation and was used to guide the design of the leading edge thickness. In general, the aspirated cascades were designed with much thicker leading edges than conventional blades due to the precise control over the leading edge shape.

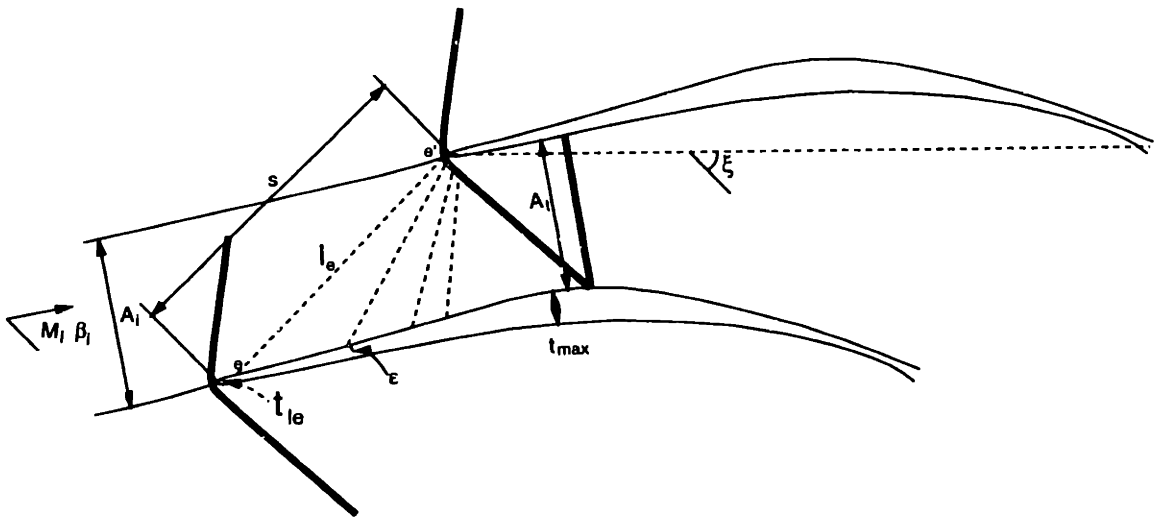

Figure 5-7: Flow features of a supersonic cascade

5.3.2 Entrance and Pre-compression

The entrance and pre-compression region of a supersonic cascade are illustrated in Figure 5-7. In supersonic cascade terminology, the entrance region is defined as the blade length from the leading edge to the first captured Mach wave indicated by $e - e'$ in the Figure. For choked blades, the blade surface tangent and Mach number at e are primarily responsible for determining the inlet flow angle through the unique incidence condition. This can be expressed using the Prandtl-Meyer angle along the left-running characteristic, assuming

isentropic expansion,

$$\begin{aligned} \nu(M_i) + \beta_i &= \nu(M_e) + \beta_e = \text{const.} \\ \Rightarrow \beta_i &= \nu(M_e) - \nu(M_i) + \beta_e \end{aligned} \tag{5.1}$$

where ν is the Prandtl-Meyer angle and M_e is the surface Mach number at e. For a flat plate cascade, the inlet angle will be equal to the stagger angle, but for finite leading edge radius and thickness, the inlet angle will be greater than the stagger angle. This has been shown in parametric studies of the entrance region using simple isentropic wave models of Levine [33] and Starken [48]. More sophisticated models which include shock losses and rotationality, such as that of York and Woodward [63], predict higher inlet flow angles. Since the stagger angle is fixed, increase in the inlet flow angle translates to an increase in operating incidence of the cascade. The larger the incidence of the cascade the more sensitive it is to area changes due to blockage and ultimately decreases the useful operating range of the blade. Clearly, the criterion for achieving a reasonable entrance region design is to minimize the deviation of the inlet flow angle from the stagger angle.

The Mach number and flow angle at the inlet are provided by the through-flow calculation, and the design of the entrance region and the blade stagger angle have to be perturbed so that the calculated flow angle which is determined by the unique incidence condition matches the inlet angle provided by the through-flow calculation. The geometric parameters that can be varied are the leading edge thickness, the angle between the suction and pressure surfaces, and the local camber angle. The minimum leading edge thickness is constrained by the structural requirements, and for the same resaon the suction and pressure surfaces near the leading edge must at least be parallel. Some degree of control over the inlet angle can be obtained by adding negative camber in the entrance region as shown in Figure 5-8 which has the effect of decreasing β_e. Once the geometry of the entrance region is fixed then further changes in the inlet flow angle can only be made by changing the stagger angle. Another important consideration is the transition from the leading edge to the blade suction surface indicated by the arc in Figure 5-8. As the inlet Mach number is increased, point e will move forward forcing a smaller leading edge radius or smaller

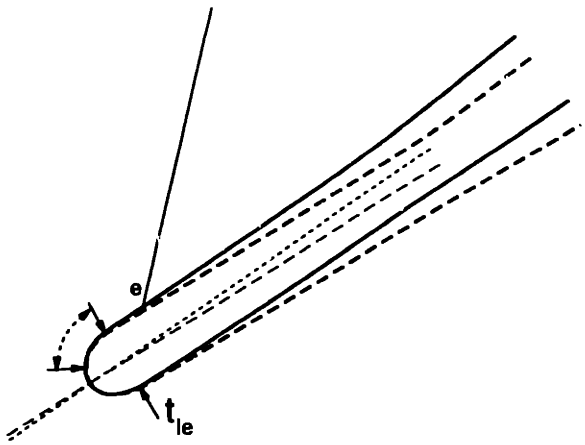

Figure 5-8: Details of leading edge and entrance region. Dotted line shows entrance region with negative camber.

blade thickness.

Finally, it is interesting to examine the effect of blade pitch on the inlet angle. By applying continuity between the inlet and $e - e'$ the following relation is obtained:

$$\sin\beta_i = \left(\frac{l_e}{s}\right) \sin\alpha_e f(M_i, M_e) \ ,$$

where α_e is the angle between $e-e'$ and the surface tangent at e. The above equation shows that the sensitivity of the inlet angle to changes in M_e and β_e will increase with decreasing pitch s. This is an important design consideration since the selection of the blade pitch also affects the boundary layer behavior.

Compression of the flow through a series of weak oblique waves can be used to decrease the Mach number entering the passage shock. The weakening of the passage shock is critical to the safe passage of the boundary layer through the shock without separating. The Mach number into the shock will depend on the throat area, and the blade surface is shaped from the entrance region up to the throat to obtain a continuous deceleration of the flow. The pre-shock Mach number can be considerably reduced by increasing the pre-compression approaching the limit of isentropic compression to sonic conditions at the throat. Although this decreases shock losses and improves boundary layer behavior off-design performance is adversely affected and the starting area ratio requirements for

establishing supersonic conditions may not be satisfied. These problems were encountered in the early external pre-compression blades tested by Creagh [4] and Jahnsen [23].

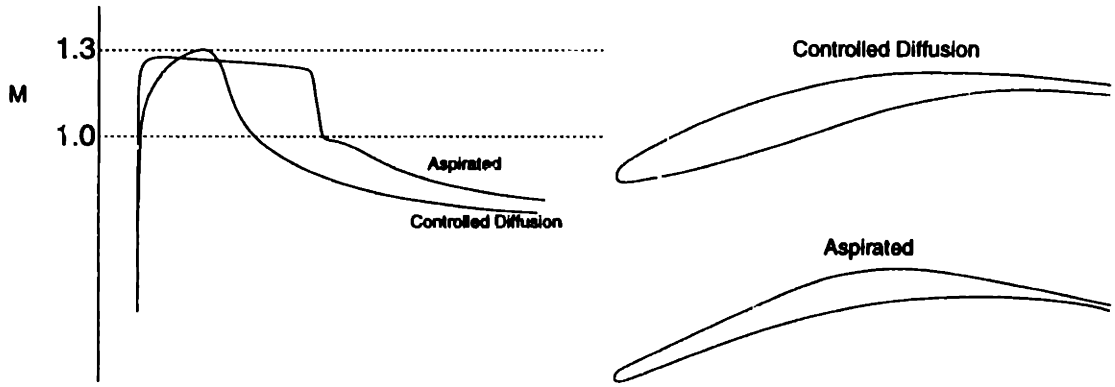

(a) Design Criteria (b) Blade Shapes

Figure 5-9: Comparison of low-speed controlled diffusion and aspirated blade pre-compression design criteria.

An interesting comparison is drawn between the design criteria followed for low-speed supercritical blades and the pre-compression region of aspirated blades in Figure 5-9 along with approximate blade shapes. The controlled diffusion design criteria developed by Hobbs and Weingold [19] have become a standard for low-speed cascades. The maximum suction surface Mach number is below 1.3 followed by a shockless deceleration up to the trailing edge. The drawback of this approach is that the acceleration in the forward portion of the blade could easily develop into a shock at negative incidence. In contrast, the aspirated blade design criterion is to maintain a milder deceleration followed by a weak shock. The blade loading is much more uniform, and the blade will be less sensitive to changes in incidence as well as Mach number. The corresponding difference in the blade shape is seen in the forward portion which is concave, or at best flat, for the aspirated blades versus a convex shape for controlled diffusion, multiple and double circular arc, and other conventional low-speed blades.

The blade maximum thickness is limited by the structural requirements and in the case of aspirated blades also by the area required for suction passages. The location of the maximum thickness has a significant impact on the overall performance of the cascade since

it determines the location of the passage shock at design condition, the curvature of the pre-compression region, and the lengtl. of the subsonic pressure recovery. The optimum location for the maximum thickness used in designs in this thesis is just upstream of the location where the bow shock impinges the suction surface. This point can be located once a preliminary design of the entrance region is completed and the shape of the bow shock is known, as shown in Figure 5-7. The flow behavior at different back pressures is shown in Figure 5-10. At design conditions the bow shock and the passage shock coalesce, but can be differentiated, just downstream of the maximum thickness location, and at peak pres-

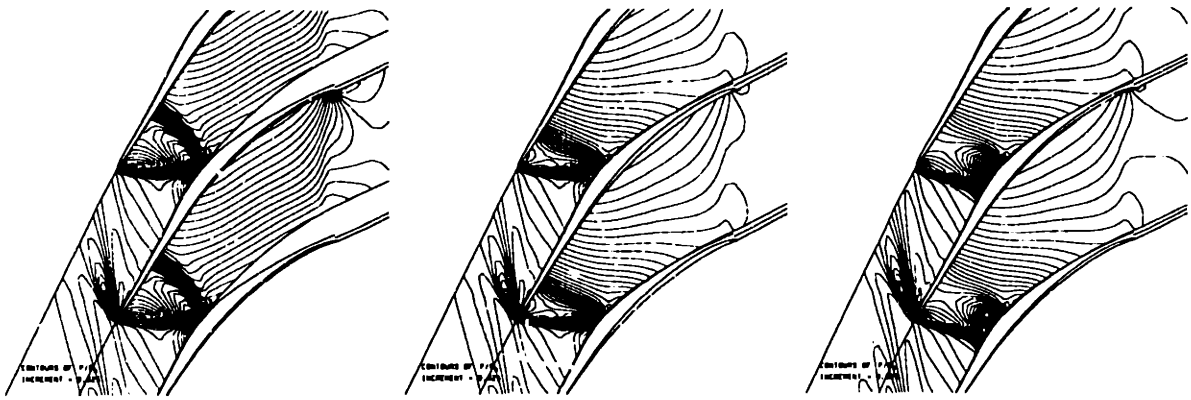

Figure 5-10: Change in shock structure at choked, peak, and spilled conditions.

sure rise there is only a strong oblique shock. At design conditions the passage shock is in the diverging part of the passage ensuring that the shock will be stable. Beyond the peak pressure rise the passage shock will move upstream of the leading edge and the cascade will unchoke. It is interesting to note that the boundary layer stays well attached even after the passage shock moves significantly upstream of the throat. This also suggests that the difficulty of establishing supersonic started flow encountered in conventional blades due to boundary layer separation may be virtually eliminated in aspirated blades.

The location of the maximum thickness $(t/c)_{max}$ forward or aft of this point is not optimal due to the following reason. If $(t/c)_{max}$ location is moved aft then at peak pressure rise the passage shock will be deeper in the blade passage whereas the oblique shock will impinge upstream of $(t/c)_{max}$ location. The boundary layer has to negotiate two shock impingement points most likely increasing the suction requirement. Moving $(t/c)_{max}$ aft

will also decrease the length of the subsonic region available for pressure recovery and turning. Moving the $(t/c)_{max}$ location upstream of the optimal location will decrease the throat area, increase the pre-compression, and the entrance region wedge angle.

The minimum passage area at the throat of the cascade must be large enough to pass the design mass flow with total pressure loss due the shock system. The minimum area ratio required to establish started supersonic flow is A_t^*/A_i^* the area ratio at sonic conditions at the inlet and throat. Design criteria of Kantrowitz [24] are the accepted method used in fixing the starting area ratios on conventional supersonic blades. The two-dimensional throat area depends only on the geometry of the cascade but the total flow area for a quasi-3D calculation also includes the streamtube contraction, AVDR, which adds an element of uncertainty to the calculation of the starting area ratio. The blockage due to the boundary layers can be accounted for in the cascade calculation but the accurate prediction of AVDR depends entirely on the results of the through-flow calculation. For the designs in this thesis, the AVDR in the final converged solution was used to verify the starting area ratio requirement combined with the shock losses predicted by the MISES calculation.

5.3.3 Pressure Recovery Region

The development of the boundary layer from the suction slot at the start of the pressure recovery region up to the trailing edge for a given exit pressure depends entirely on the shaping of the pressure distribution in this region. The pressure recovery region is designed to achieve the smallest possible displacement and momentum thickness at the trailing edge. The design process is illustrated using a transonic stator cascade with a fairly large turning angle of 57°. Figure 5-11 shows the pressure distribution and shape parameter distribution of the original cascade. Downstream of the suction slot, the pressure decreases linearly up to 80% chord where the boundary layer rapidly separates. Although boundary layer separation is delayed due to suction, this example shows that suction is not sufficient to ensure a well attached boundary layer up to the trailing edge. The shape of the pressure recovery region seen on this stator is typical of profile families such as the double circular arc and multiple circular arc cascades. Figure 5-12 shows the redesigned pressure recovery and

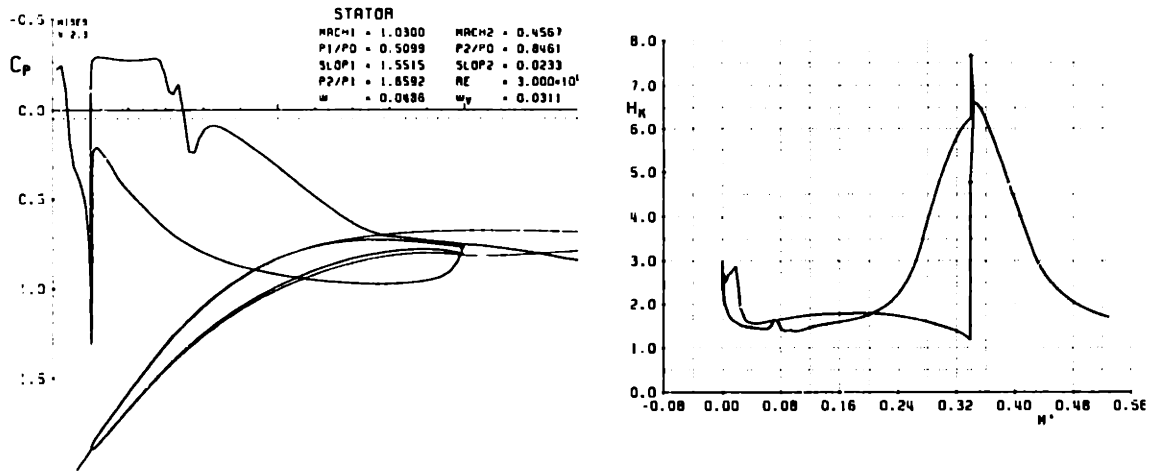

(a) Pressure Coefficient **(b)** Shape Parameter

Figure 5-11: Stator cascade

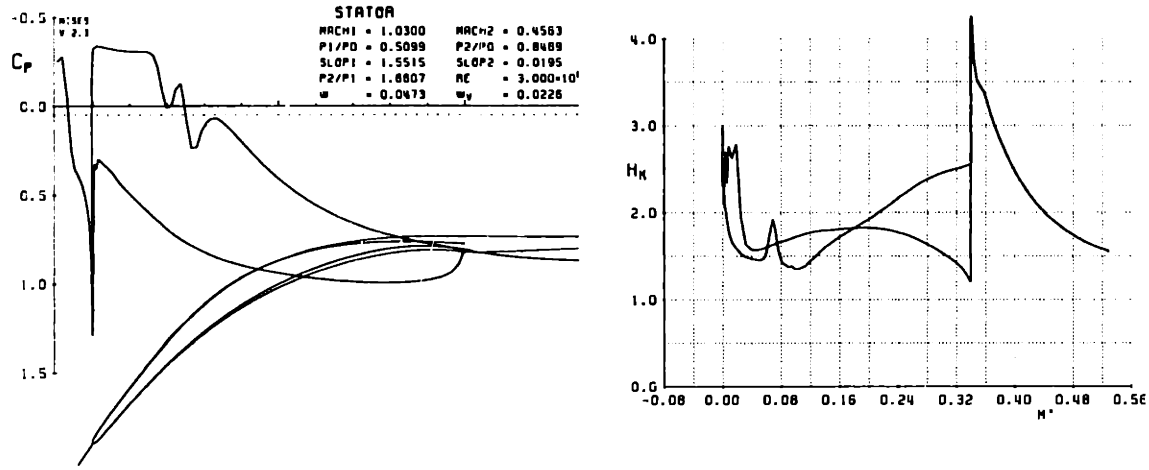

(a) Pressure Coefficient **(b)** Shape Parameter

Figure 5-12: Stator cascade redesigned pressure recovery.

corresponding shape parameter distribution. The pressure distribution is designed so that the pressure gradient is continuously decreasing ($d^2p/dx^2 < 0$), and the resulting effect on the boundary layer is an almost linear increase in the shape parameter to a maximum value of 2.5 at the trailing edge compared to 6 for the original blade shape. As the pressure gradient becomes more adverse, the initial deceleration is more severe and the overall shape of the pressure distribution becomes more concave. The redesigned cascade shows a

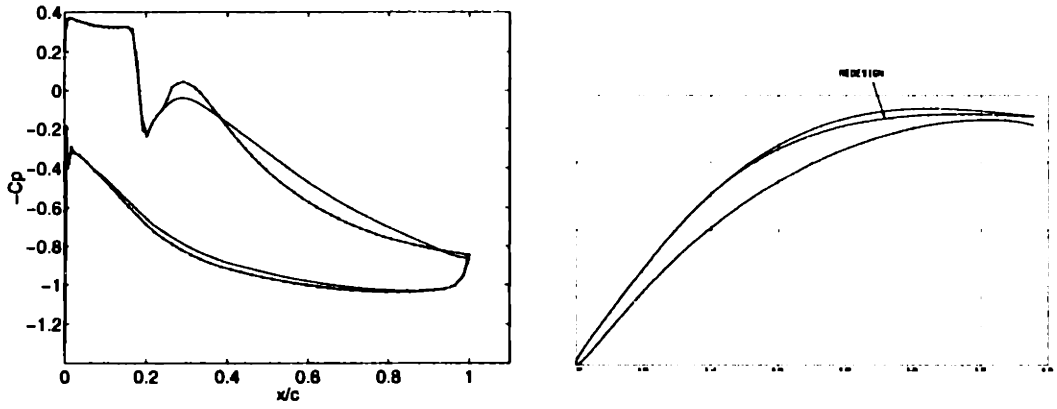

(a) Pressure Coefficient

(b) Blade Modification

Figure 5-13: Comparison of pressure distribution and blade shape.

30% decrease in viscous loss and 20% increase in turning. Figure 5-13 compares the shape of the inviscid pressure distribution and the corresponding change in the blade shape. The redesigned blade shows a significant decrease in thickness near 70% chord, and in some cases this limits the shaping of the pressure distribution in that region.

The design of pressure recovery regions has been studied in detail for low-speed and supercritical blades which have laminar roof top pressure distributions [19]. The pressure recovery region is designed to have a constant skin friction close to separation similar to that proposed by Stratford [51]. The rationale of this approach is that the skin friction drives the increase in momentum thickness. Consequently, the Stratford type pressure recovery shows a very steep initial deceleration followed by a mild deceleration where the skin friction is held close to zero. Examination of the integral momentum equation (3.4) reveals that the momentum thickness growth depends on the balance between the skin friction and the pressure gradient term, and is minimum when the sum of these two contributions is minimized [9]. This can also be seen by eliminating the skin friction from the momentum equation using the kinetic energy equation (4.29) giving

$$\frac{d\theta}{ds} = \frac{2C_D}{H^*} - \frac{3\theta}{u_e}\frac{du_e}{ds} - \frac{\theta}{H^*}\frac{dH^*}{ds}. \tag{5.2}$$

All the terms in the above equation contribute to the growth of θ, but the turbulent dissipation term is minimum at $H \sim 1.5$, which indicates that $d\theta/ds$ will be a minimum, not close to separation $H \sim 3$, but for a modest $H \sim 2$ or so. The pressure recovery on the aspirated blades is designed for a smaller average shape parameter over the pressure recovery region in order to ensure some margin for three-dimensional effects. A smaller shape parameter/displacement thickness translates to lower blockage and smaller deviation in the exit angle from the blade metal angle which has a significant impact on the pressure rise for blades with large turning.

5.3.4 Diverging Trailing Edge

The boundary layer on the blade suction side undergoes a strong deceleration in the pressure recovery region, and cusping the trailing edge can be used to relax pressure gradient preventing the peeling off of the boundary layer near the trailing edge. The cusped shape may however lead to virtually zero thickness and is traditionally fixed by thickening the trailing edge and closing the gap with a circle. An extension of a cusped trailing edge is the diverging trailing edge shown in Figure 5-14. The diverging trailing edge (DTE) concept was used by Korn [30] on supercritical compressor cascades and has also been studied by

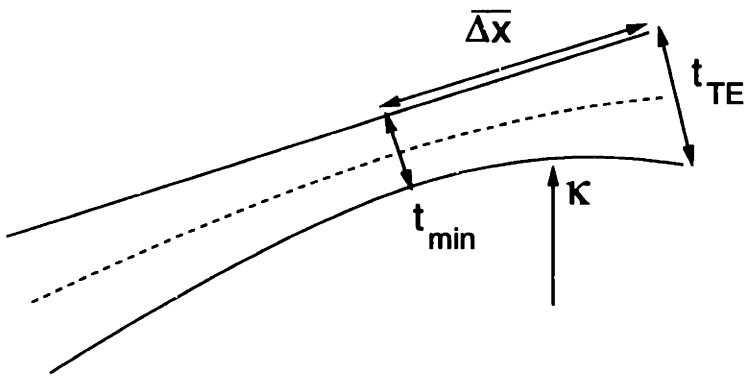

Figure 5-14: Diverging Trailing Edge

Henne [16] for supercritical aircraft airfoils. A primitive version called the Gurney flap is often used on race car wings. The trailing edge has a finite thickness with the slope diverging from the suction surface resulting in a negative trailing edge angle. The shape of the pressure surface near the trailing edge region, assuming a smoothly varying surface, can

be controlled by effectively three parameters: the trailing edge thickness, the minimum thickness, and location of the minimum thickness as shown in Figure 5-14.

The diverging pressure surface can be used to achieve a high aft loading by increasing the pressure surface curvature as shown in Figure 5-15. The ability to support a large positive

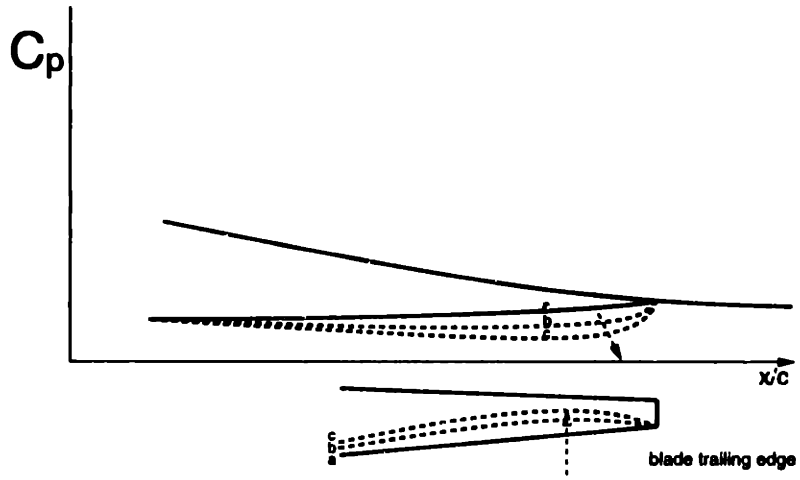

Figure 5-15: Aft-loading due to pressure surface curvature.

C_p depends on the curvature of the pressure surface near the trailing edge [11]. The trailing edge thickness is an important parameter which controls the pressure side curvature near the minimum thickness location and also influences the total pressure loss downstream of the blade. The increase in aft loading can be related to the curvature of the pressure surface near the trailing edge via the normal momentum equation

$$\frac{\partial p}{\partial n} = \kappa \rho u^2 .$$

For small curvature,$\kappa \simeq \Delta n/\Delta x^2$, where $\Delta n = t_{\text{te}} - t_{\text{min}}$. Substituting in the normal momentum equation gives

$$\Delta p \simeq \left(\frac{t_{\text{te}} - t_{\text{min}}}{\Delta x}\right)^2 \rho u^2$$

which shows that the increase in pressure scales as t_{te}^2. The corresponding increase in the blade loading is $\Delta l \simeq \Delta p \Delta x$. The effect of trailing edge thickness on the total pressure loss can be obtained by performing a mixed out analysis of the flow downstream of the trailing

edge. The total pressure loss, assuming incompressible flow, is given by

$$\frac{P_{0te} - P_{0\infty}}{\frac{1}{2}\rho U_\infty^2} = \frac{\left(\frac{t_{te}}{s}\right) C_{pb} + \frac{2}{H}\frac{\delta^*_{te}}{s} + \left(\frac{t_{te}}{s} + \frac{\delta^*_{te}}{s}\right)^2}{\left(1 - \frac{t_{te}}{s} + \frac{\delta^*_{te}}{s}\right)^2} \tag{5.3}$$

where C_{pb} is the negative base pressure coefficient, s is the blade pitch, and infinity refers to mixed-out values. The first contribution to the total pressure loss is due to the negative base pressure, the second is due to the profile drag, and the third is due to area blockage resulting from the blade thickness and boundary layer displacement thickness at the trailing edge. The base pressure coefficient increases almost linearly for moderate trailing edge thicknesses indicated by the data of Nash [36] and Hoerner [20] which shows that the base pressure contribution to the loss scales as t_{te}^2. The third term due to the blockage also scales as t_{te}^2. The loss contribution due to the second term however is proportional to δ^*_{te}. From this it can be deduced that if the trailing edge thickness is not much larger than δ^*_{te} the penalty of a thick trailing edge will be small compared to the benefit of increased aft loading.

The criterion for fixing the trailing edge thickness is that the boundary layer remain attached up to the trailing edge. If the boundary layer separates before the trailing edge, then the blade is ended and the boundary layer is shed as wake. Once the trailing edge thickness is fixed the pressure surface can be designed to increase the aft loading. The primary constraint on the amount of pressure surface curvature is the minimum thickness which must meet structural requirements, and for the same reason the location of the minimum thickness cannot be located too far forward. The other constraint on the pressure surface curvature is that the boundary layer will be subjected to an adverse pressure gradient upstream of the minimum thickness which acts to relieve the aft loading and may lead to separation of the pressure surface boundary layer.

An integral boundary layer formulation for modeling blunt trailing edges was developed by Drela [8] and is incorporated in MISES.

5.3.5 Pressure Surface

The pressure surface, although usually fairly straightforward to design, requires some attention in the case of aspirated blades where the large turning combined with relatively high inlet Mach numbers leads to severe adverse pressure gradients up to mid-chord. For choked cascades, the passage shock impinges on the pressure surface further exacerbating

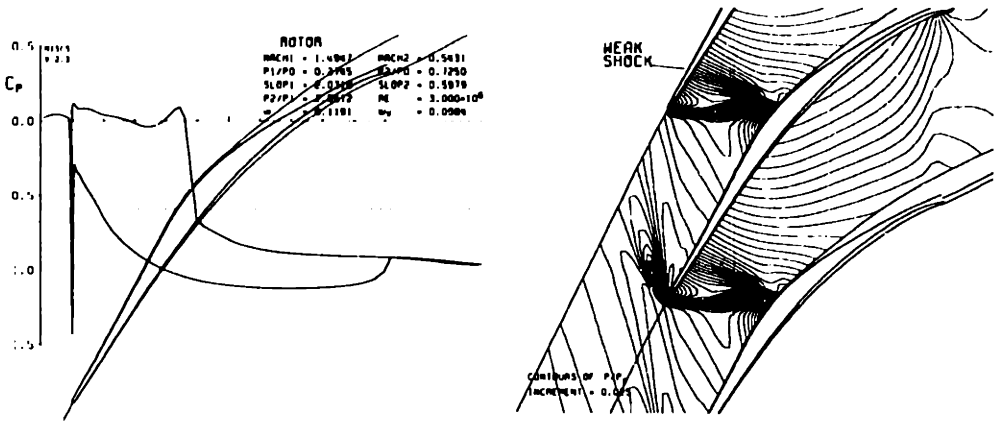

(a) Pressure Coefficient **(b)** Pressure Contours

Figure 5-16: Example of blade pressure surface design.

the condition of the boundary layer. A thicker pressure side boundary layer will decrease in the curvature of the streamlines near the minimum thickness location close to the trailing edge resulting in a decrease the increment in blade loading due to the diverging trailing edge.

Figure 5-16 shows the pressure distribution and pressure contours illustrating the design of the blade pressure side. The shape of the pressure side distribution is similar to the concave pressure recovery region on the suction side described above. The shape parameter attains a maximum value at mid-chord, and the boundary layer may separate around mid-chord if the passage shock is strong or if the pressure distribution is not well designed. The pressure contours in Figure 5-16 (b) show the weakened passage shock due to shaping of the pressure surface.

Chapter 6

Low-Speed Stage

The low-speed stage was designed to examine the feasibility of lowering the rotor blade speed from supersonic to subsonic while maintaining a given pressure ratio and isentropic efficiency. The immediate advantage of lowering the blade speed is the reduction in shock losses which in turn almost eliminates the possibility of boundary layer separation due to interaction with the shock. Large noise reduction and lower structural stresses are also expected. The boundary layer growth in the high turning subsonic region is controlled by judicious use of suction.

This chapter discusses the low-speed stage design in detail. The important stage design parameters are presented, followed by a brief description of the suction configuration. The quasi 3-D blade section calculations are discussed next followed by results of the 3-D inviscid and viscous calculations.

6.1 Stage Design Parameters

A summary of the low-speed stage design parameters are presented in Table 6.1. The total pressure ratios across the rotor and stage are spanwise averages calculated from mixed out flow conditions from each quasi 3-D streamsurface solution. The suction requirement for both rotor and stator are based on the stage inlet mass flow. The area used to report

Tip Speed U (ft/s)	750
Rotor Pressure Ratio	1.65
Stage Pressure Ratio	1.60
Mass Flow/Area (lbm/ft^2/s)	44.8
Rotor face Axial Mach Number	0.62
Stator Exit Mach Number	0.70
Rotor Tip Rel. Mach Number	0.95
Stator Hub Abs. Mach Number	1.15
Rotor Hub/Tip Ratio	0.63
Suction Mass %	0.5/0.5
Max. Diffusion Factor	0.56/0.54
Rotor Tip Solidity	1.4
Stator Hub Solidity	2.1
Rotor Isentropic Efficiency	0.97
Stage Isentropic Efficiency	0.94
Tip Blade Loading $\left(\Delta H/U_{\text{tip}}^2\right)$	0.86

Table 6.1: Low-Speed Stage Design Parameters

the mass flow is based on the rotor face $r_{\text{hub}}/r_{\text{tip}}$. The diffusion factors are calculated using Equation (2.6), and the solidities are based on blade chord in the $m' - \theta$ plane. The isentropic efficiencies reflect only the losses in the blade wakes.

6.2 Suction Configuration

Suction is applied through spanwise slots on the blade surface and circumferential slots on the flowpath. The location and suction mass flow of the blade slot was an outcome of the quasi 3-D design process whereas the suction requirement on the flowpath was determined from the 3-D viscous calculation. Table 6.2 summarizes the slot locations and

	Blade	Hub	Tip
Rotor/Stator	0.5 / 0.5	-	-
Rotor Upstream	-	-	1.29
Inter-blade	-	0.5	1
Shock Location	-	0.5	0.5

Table 6.2: Low-Speed Stage Suction Configuration

suction mass flow coefficients. This suction configuration is used in experimental setup as described by Schuler [46].

6.3 Through-Flow Solution

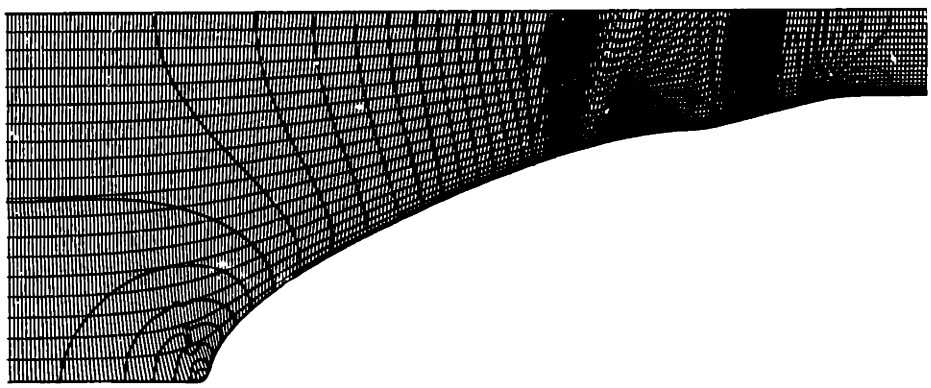

Figure 6-1: Low-speed stage through-flow solution pressure contours.

The cross section of the flowpath and through-flow solution pressure contours are shown in Figure 6-1. The inlet design mass flow is 63.22 lbs/s based on a 10.35" radius of the MIT Blowdown compressor facility. The rotor-stator spacing is approximately 50% of the rotor tip chord to accommodate instrumentation. The pressure contours show that most of the pressure rise occurs across the stator which is a consequence of the unusually low rotor speed.

6.4 Quasi 3-D Solutions

6.4.1 Rotor Hub

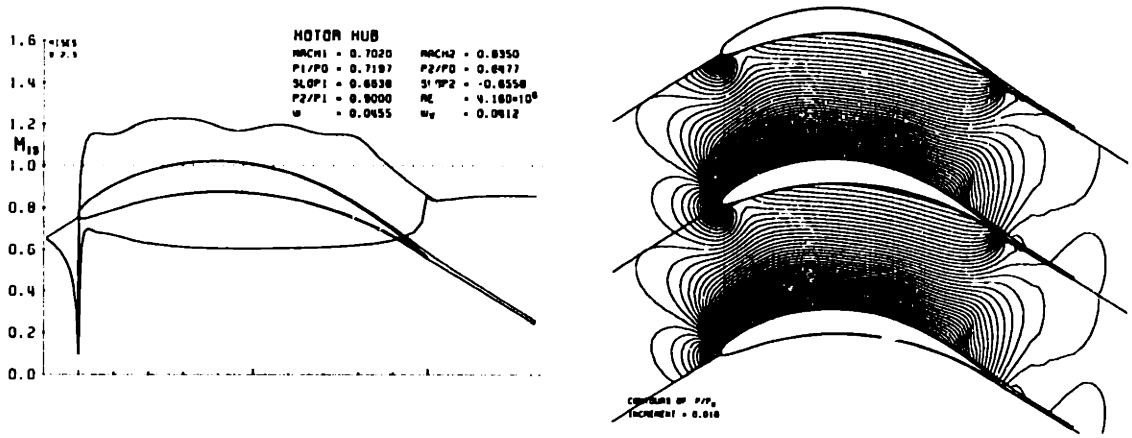

(a) Isentropic Mach Number

(b) Contours of Pressure

Figure 6-2: Low-speed stage rotor hub.

Figure 6-2 shows the rotor hub blade surface isentropic Mach number distribution and blade to blade pressure contours. This section has negative reaction indicated by the static pressure ratio of 0.9. A Mach number of 1.2 is maintained over most of the suction surface with pressure recovery beginning at 80% chord. The pressure surface shows an almost constant Mach number of 0.6, and almost uniform blade loading is maintained up to the trailing edge as a result of the diverging trailing edge shape. The total loss is mainly due to viscous profile loss associated with the thin boundary layer. The pressure contours show a shock-free uniform blade loading along the chord. Suction was not required at this section.

6.4.2 Rotor Mid-Span

Figure 6-3 shows the rotor mid-span blade surface isentropic Mach number distribution and blade to blade pressure contours. The suction surface shows a weak shock at 15% chord followed by a pressure spike due to the suction slot. A relatively mild subsonic pressure recovery begins just downstream of the suction slot. The pressure surface shows

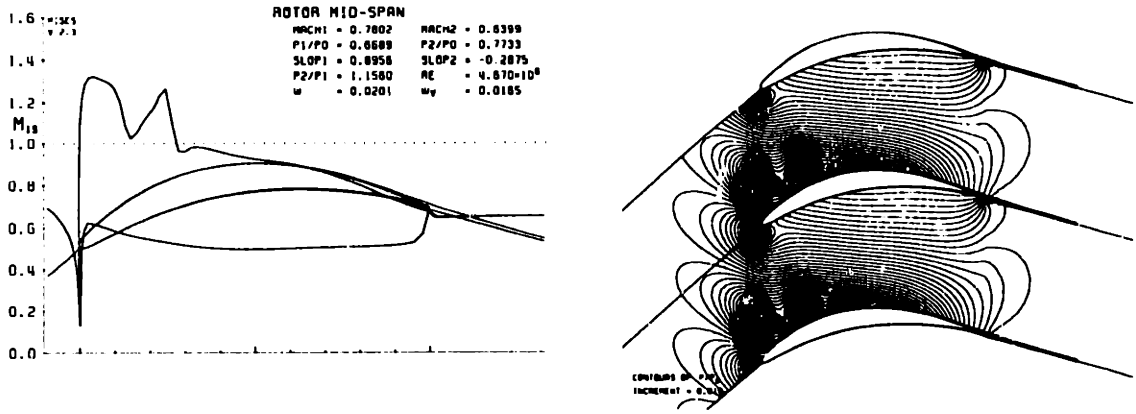

(a) Isentropic Mach Number

(b) Contours of Pressure

Figure 6-3: Low-speed stage rotor mid-span.

an almost constant Mach number of 0.5 which is maintained up to the trailing edge. The viscous loss contribution is lower than the hub but still 75% of the total loss. The weak shock and effect of the suction slot are seen in the blade to blade pressure contours. The effect of the diverging trailing edge is seen in the concentration of pressure contours on the pressure side near the trailing edge.

6.4.3 Rotor Tip

Figure 6-4 shows the rotor tip blade surface isentropic Mach number distribution and blade to blade pressure contours. Pre-compression of the flow is seen on the suction surface up to 30% chord followed by a weak shock and the effect of the suction slot. The pressure recovery region is more concave in shape compared to the mid-span due to the higher diffusion requirement. A mild adverse pressure gradient is seen on the pressure side up to mid-chord followed by an almost constant Mach number up to the trailing edge. The aft loading effect of the diverging trailing edge is clearly seen. The blade to blade pressure contours show the extent of the shock and the effect of the suction slot downstream. The diffusion factor is 0.56 – the highest for the stage. The total loss is equally split between the shock loss and viscous profile loss.

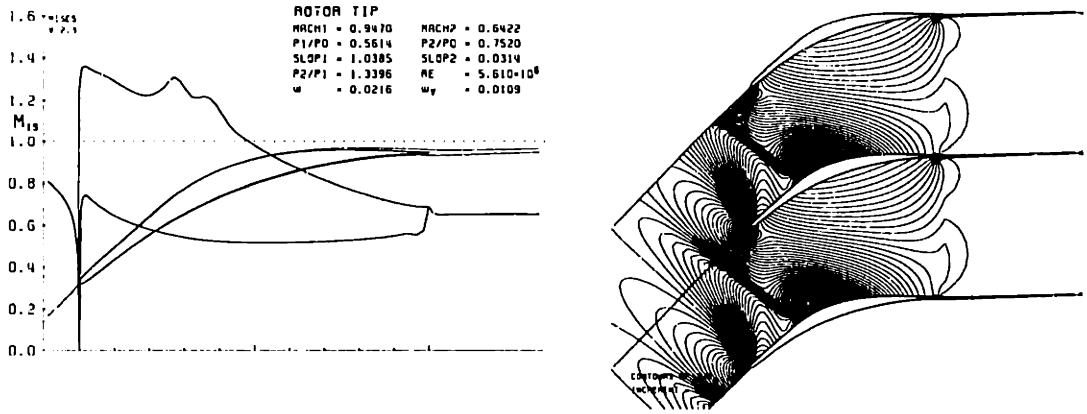

(a) Isentropic Mach Number

(b) Contours of Pressure

Figure 6-4: Low-speed stage rotor tip.

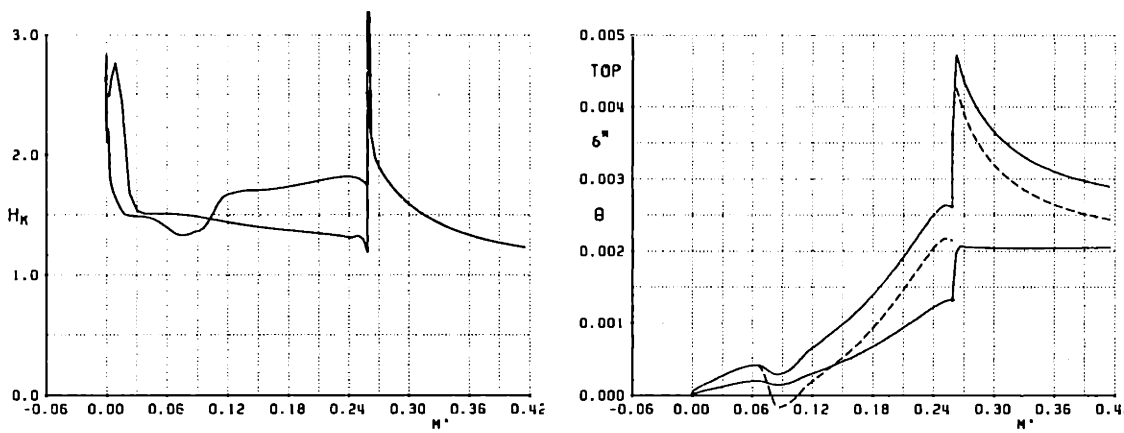

(a) Kinematic Shape Parameter

(b) Suction Side δ^* and θ

Figure 6-5: Low-speed stage rotor tip boundary layer profiles. Dashed line is $\delta^* - \dot{m}_{\text{suct}}/\rho_e u_e$ (removed streamtube height).

Figure 6-5 shows the boundary layer growth on the suction side. The effect of the suction is seen in the H_k decrease at 30% chord, and the overall increase in shape parameter is small up to the trailing edge. The difference between the solid δ^* line and the dashed line on the $\delta^* - \theta$ plot indicates the suction mass defect δ^*_{suct}, and $(\delta^*_{\text{suct}}/\delta^*_1) \sim 1$.

6.4.4 Stator Hub

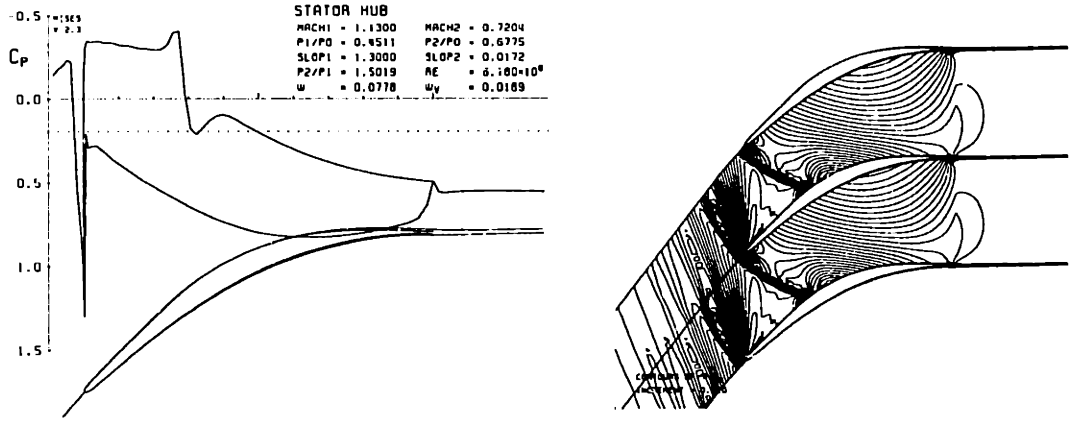

(a) Isentropic Mach Number

(b) Contours of Pressure

Figure 6-6: Low-speed stage stator hub.

Figure 6-6 shows the stator hub blade surface isentropic Mach number distribution and blade to blade pressure contours. The inlet Mach number is supersonic and the passage shock is significantly stronger than the rotor. The total loss is dominated by the shock loss. The flow is mildly pre-compressed before the shock followed by a small re-acceleration downstream of the shock into a concave pressure recovery region. The adverse pressure gradient on the pressure surface is stronger and extends beyond mid-chord. The loading on the pressure surface is maintained up to the trailing edge. Note the high static pressure ratio since none of the pressure rise occurs in the rotor hub. The flow turning required to axial direction is 50°. The blade to blade pressure contours show the bow shock and stronger passage shock. The diffusion factor is 0.54, and is lower than the rotor tip, despite the stronger shock and more turning due to the higher blade solidity and streamtube contraction.

Figure 6-7 shows the shape parameter distribution and boundary layer growth on the suction side. The shape parameter is 1.5 over most of the suction side except near the shock location. The discontinuous rise in shape parameter at the trailing edge is due to the trailing edge gap, which was larger than necessary to account for the anticipated effects of the endwall boundary layer and secondary flow near the hub. The $\delta^* - \theta$ plot shows the rapid

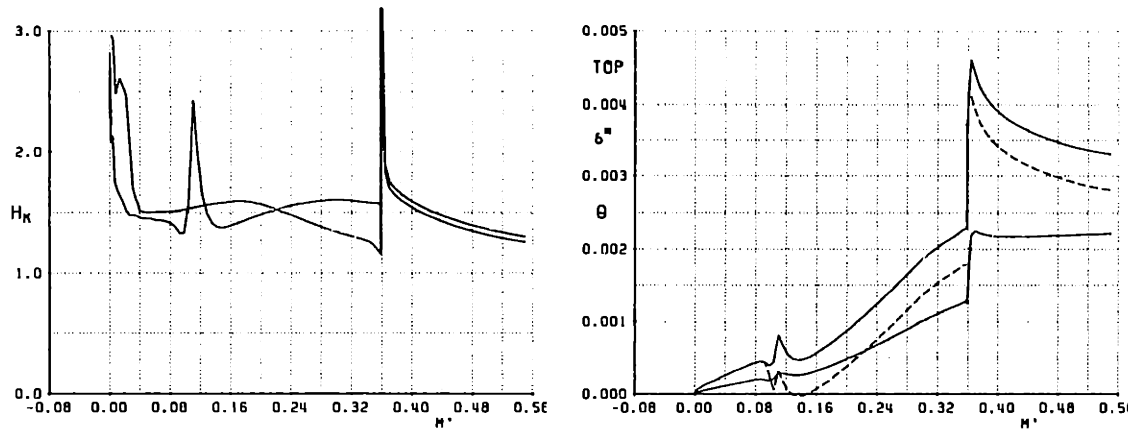

(a) Kinematic Shape Parameter

(b) Suction Side δ^* and θ

Figure 6-7: Low-speed stage stator hub boundary layer profiles. Dashed line is $\delta^* - \dot{m}_{\text{suct}}/\rho_e u_e$ (removed streamtube height).

growth of δ^* near the shock and also the effect of suction. The suction mass defect ratio $(\delta^*_{\text{suct}}/\delta^*_1) \sim 1$.

6.4.5 Stator Mid-Span

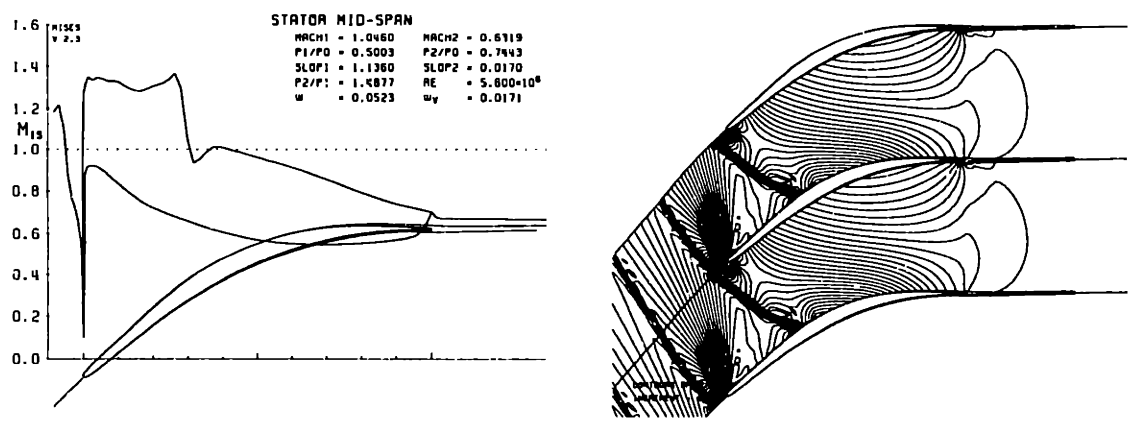

(a) Isentropic Mach Number

(b) Contours of Pressure

Figure 6-8: Low-speed stage stator mid-span.

Figure 6-8 shows the stator mid-span blade surface isentropic Mach number distribution

and blade to blade pressure contours. The overall shape of the pressure distribution is very similar to the stator hub. The shock is weaker and very little pre-compression is used upstream of the shock. The blade to blade pressure contours show the shock strength and location.

6.4.6 Stator Tip

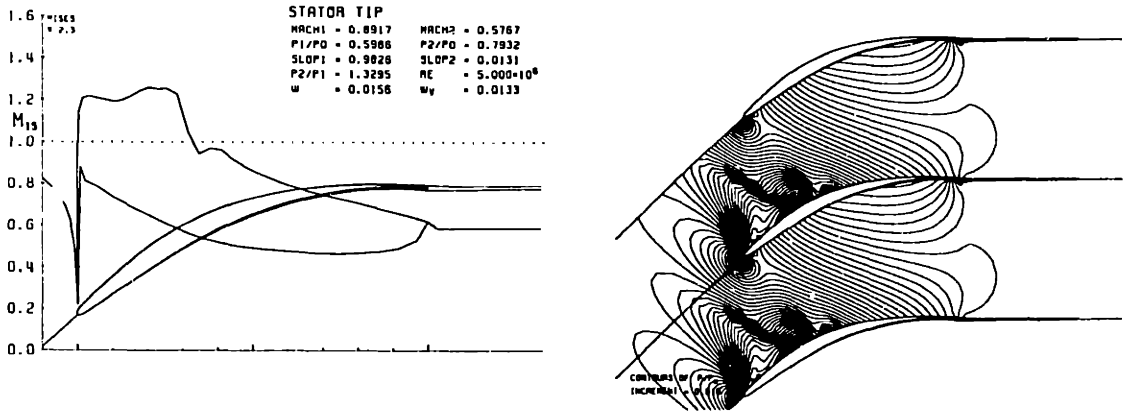

(a) Isentropic Mach Number

(b) Contours of Pressure

Figure 6-9: Low-speed stage stator tip.

Figure 6-9 shows the stator tip blade surface isentropic Mach number distribution and blade to blade pressure contours. The inlet Mach number is subsonic and the shock is much weaker than lower span locations. This is seen clearly in the blade to blade pressure contours. The viscous loss is 80% of the total loss.

6.5 3-D Euler Solution

The Euler calculation was performed at the design mass flow. A tetrahedral grid with 34200 element and 67000 points was used for the rotor calculation and 270000 elements and 53000 points for the stator calculation. The effect of suction was not modeled in the calculation. Both rotor and stator calculations were performed in isolation with a matching

of only the mass flow and mass averaged tangential and meridional flow angles at the interface.

6.5.1 Rotor

Figure 6-10 (a) shows the pressure contours on the rotor suction side. The shock extends from 40% span up to the tip, and the extent and location of the shock is in good agreement with the quasi 3-D calculation. A re-expansion of the flow followed by a weak shock is also seen downstream of the first shock. The low pressure region near the hub trailing

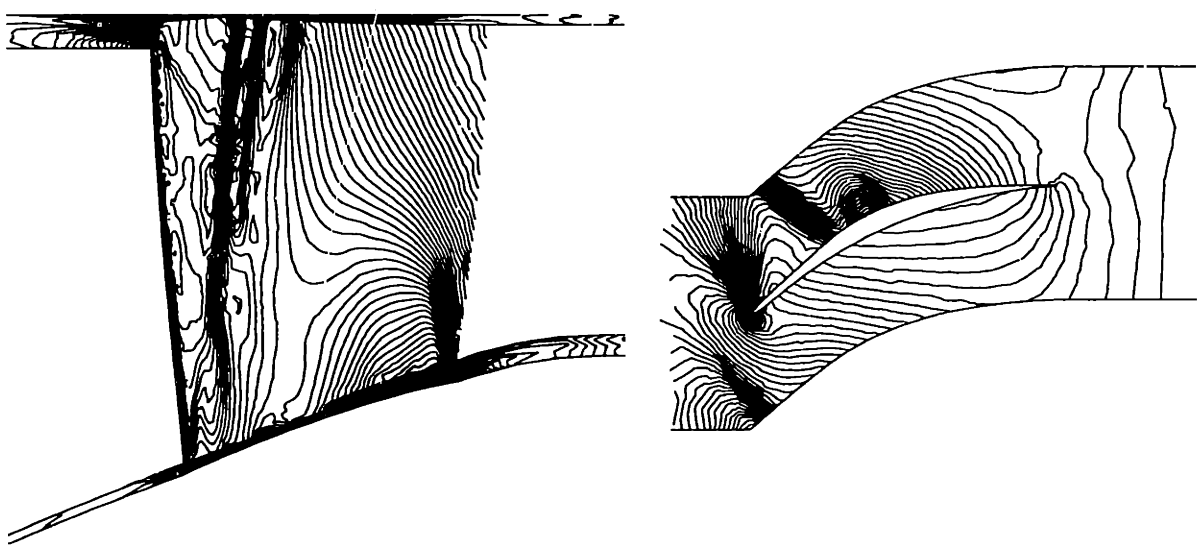

(a) Suction Side Contours of Pressure

(b) Rotor Tip Contours of Pressure

Figure 6-10: Low-speed stage rotor 3-D Euler solution.

edge is due to the blending of the flowpath with the constant radius section required to calculate the rotor in isolation. The pressure contours also indicate the decreasing diffusion level from tip to hub consistent with the decreasing exit angle. Figure 6-10 (b) shows the blade passage contours near the tip. The shock location matches well with the quasi 3-D calculation shown in Figure 6-4 (b) although the solution is more diffused due to the lower grid resolution. Good overall agreement is seen with the quasi 3-D calculation.

6.5.2 Stator

Figure 6-11 (a) shows the pressure contours on the stator suction side. The mass flow and mass averaged rotor exit angles were prescribed as inlet conditions for this calculation. No loss or blockage were included. The shock extends along the entire span and is signifi-

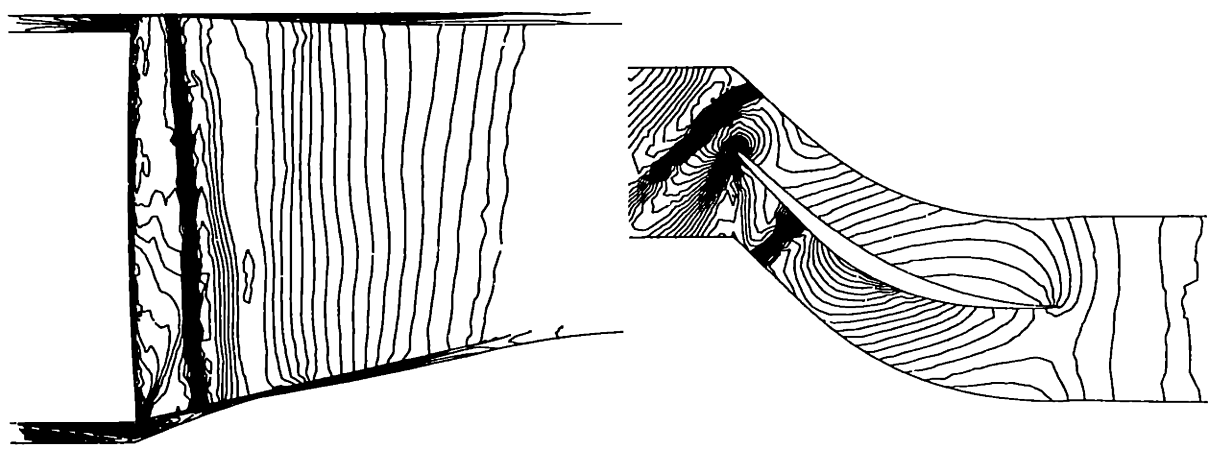

(a) Suction Side Contours of Pressure **(b)** Rotor Tip Contours of Pressure

Figure 6-11: Low-speed stage stator 3-D Euler solution.

cantly stronger than the rotor. The almost vertical pressure contours indicate a uniform diffusion of the flow downstream of the shock along the entire span. Figure 6-11 (b) shows the blade passage pressure contours near the hub. Good agreement is seen in the shock location and overall flow features with the quasi 3-D calculation shown in Figure 6-6 (b).

6.6 3-D Viscous Solution

The results of the 3-D viscous analysis presented in this section were calculated using the APNASA code, described in section 4.7, by Adamczyk and Celestina. The grid used for the calculation has 255 axial, 51 circumferential, and 51 spanwise points. The design suction slot location was not matched exactly in the viscous calculation because the code requires the slot to be specified along a constant spanwise grid line. The slot location was

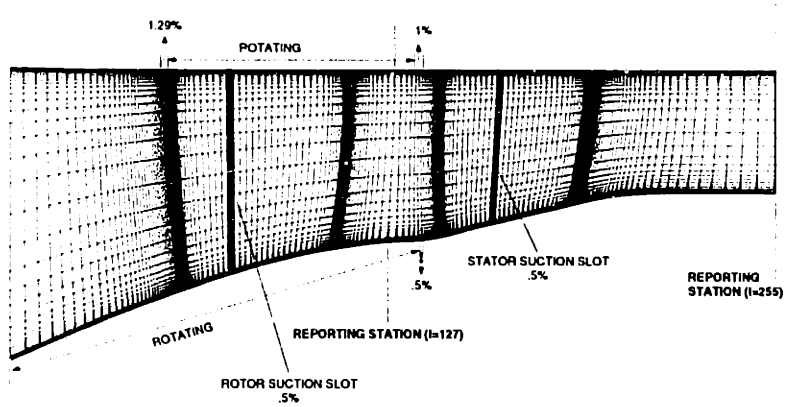

Figure 6-12: Low-speed stage 3-D viscous calculation suction configuration.

matched in an average sense by selecting a grid line that resulted in the least deviation from the prescribed slot location. The blade geometry was altered by fitting leading edge and trailing circles to meet grid generation constraints. The diverging trailing edge was not completely resolved because the grid required pairs of suction and pressure side points with the same axial location.

6.6.1 Design Point Solution

The case presented below was calculated at an inlet mass flow of 63.9 lbs/s. This solution was found to have the best overall performance and was designated as the design point. The stage pressure ratio is 1.595 with an isentropic efficiency of 89.3%. A total suction of 3.79% was prescribed in the calculation and the distribution at various locations is shown in Figure 6-12. The shock impingement suction on the hub and casing were not included in any of the viscous calculations.

6.6.1.1 Rotor Hub

Figure 6-13 shows the relative Mach contours at the rotor hub. The effect of the suction slot is visible at 40% chord on the blade suction side. The boundary layer is seen to thicken

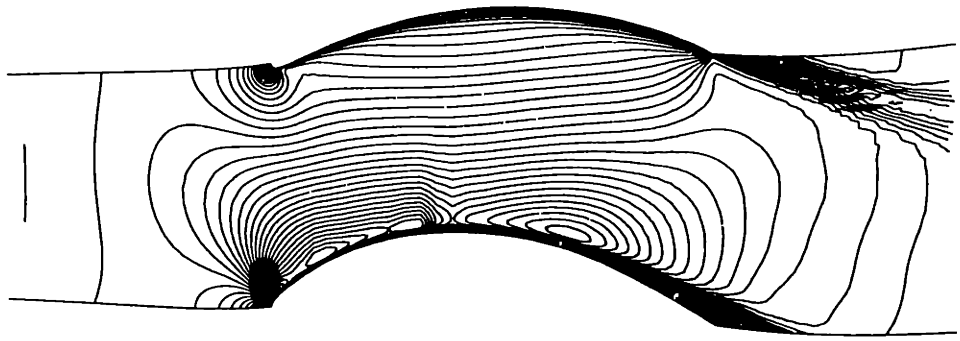

Figure 6-13: Low-speed stage rotor hub 3-D viscous relative Mach contours.

from 60% chord considerably more than the quasi 3-D solution, but is very similar to the quasi 3-D solution outside the viscous layer.

6.6.1.2 Rotor Mid-Span

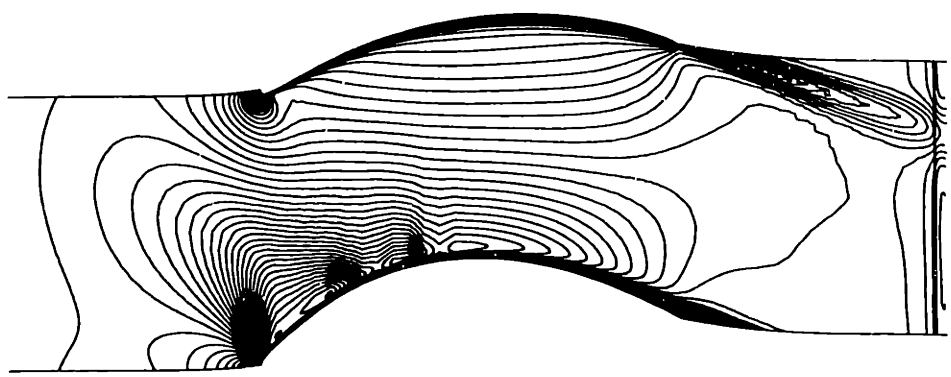

Figure 6-14: Low-speed stage rotor mid-span 3-D viscous relative Mach contours.

Figure 6-14 shows the relative Mach contours at rotor mid-span. The effect of the suction slot is visible at 40% chord on the blade suction side. A weak shock is observed at 20% chord consistent with the quasi 3-D calculation. The boundary layer at the trailing edge is

much thinner than that at the hub. The effect of the diverging trailing edge is seen in the converging Mach contours near the pressure side trailing edge. The effect of the diverging trailing edge is seen to be much weaker compared to the quasi 3-D calculation.

6.6.1.3 Rotor Tip

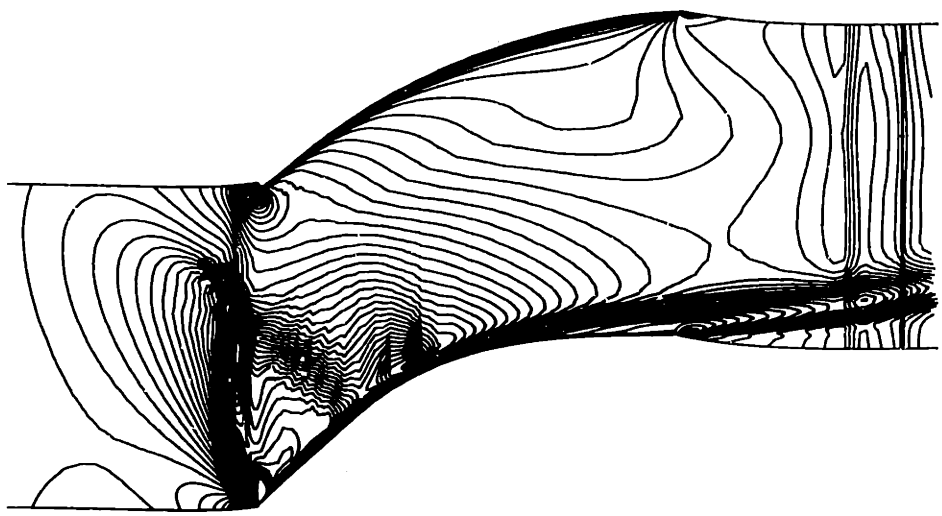

Figure 6-15: Low-speed stage rotor tip 3-D viscous relative Mach contours.

Figure 6-15 shows the relative Mach contours at rotor tip. The effect of the suction slot is seen at 40% chord on the suction side. The shock is located further upstream than the shock location in the quasi 3-D calculation. The build up of contours upstream of the leading edge is due to the casing suction slot and the transition of the flow from the stationary casing to the rotating tip shroud. The direction of the wake with respect to the blade and the thickening of the boundary layer downstream of the slot indicate that the boundary layer is close to separation on the blade. The overall indication is that the blade is operating at a higher incidence than the design intent. The effect of the diverging trailing edge is seen on the pressure side near the trailing edge but is not as strong as the quasi 3-D calculation. The vertical contours downstream of the rotor trailing edge are due to the transition from the rotating shroud to the stationary casing.

6.6.1.4 Stator Tip

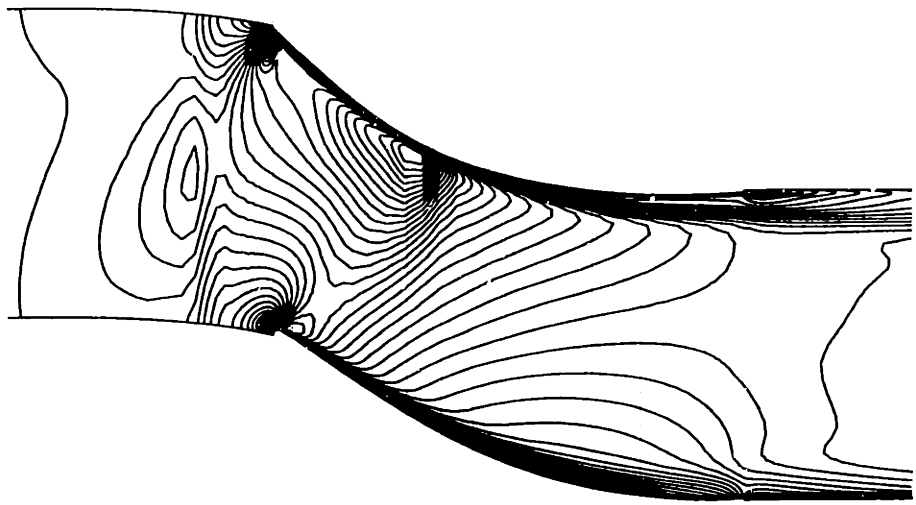

Figure 6-16: Low-speed stage stator tip 3-D viscous absolute Mach contours.

Figure 6-16 shows the absolute Mach contours at stator tip. The effect of suction is seen at 40% chord on the suction surface. The boundary layer on the suction surface is thin but the pressure side boundary layer is thicker indicating that the stator is operating at negative incidence. The effect of the casing suction is seen upstream of the stator.

6.6.1.5 Stator Mid-Span

Figure 6-17 shows the absolute Mach contours at stator mid-span. The effect of suction is seen at 40% chord on the suction surface. The average inlet Mach number is close to sonic which is lower than the quasi 3-D calculation at the same span location. The shock location is at 20% further upstream compared to the quasi 3-D calculation which indicates a higher than design incidence angle. The boundary layer growth is also significant from 70% chord.

6.6.1.6 Stator Hub

Figure 6-18 shows the absolute Mach contours at stator hub. The effect of suction is seen at 40% chord on the suction surface. The shock strength is not much greater than mid-

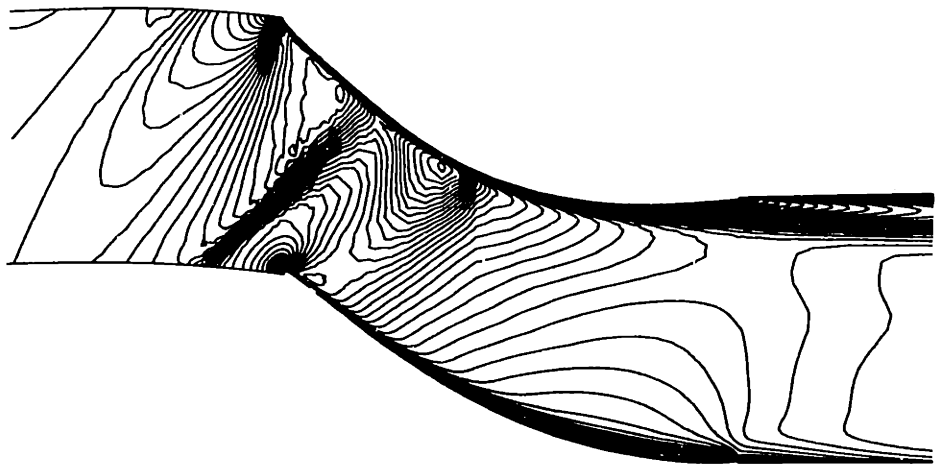

Figure 6-17: Low-speed stage stator mid-span 3-D viscous absolute Mach contours.

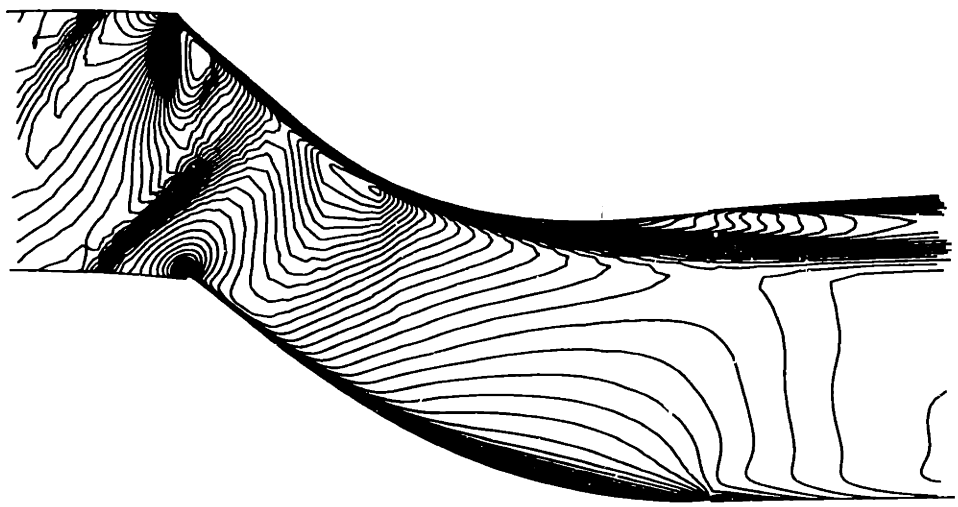

Figure 6-18: Low-speed stage stator hub 3-D viscous absolute Mach contours.

span but significant deviation of the boundary layer from the blade is seen. Once again the shock location is further forward than the design intent of the quasi 3-D calculation indicating a higher incidence angle.

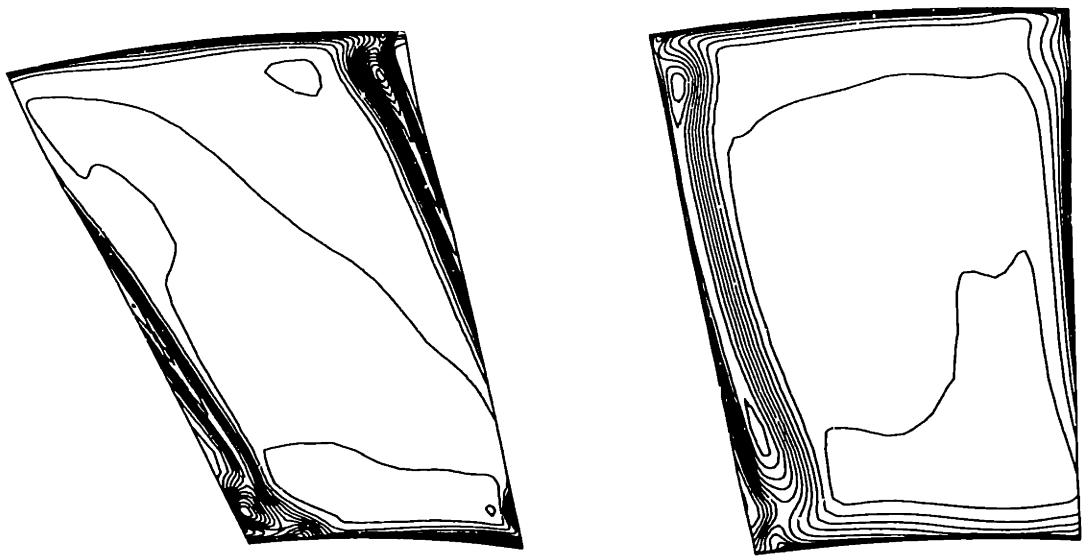

(a) Rotor Exit (b) Stator Exit

Figure 6-19: Low-speed stage rotor and stator wake axial velocity contours.

6.6.1.7 Rotor and Stator Exit Wakes

Figure 6-19 shows the rotor exit wake and the stator exit wake axial velocity contours. The rotor exit contours in the endwall region between the blades show well attached boundary layers on the hub and casing. An increase in the endwall boundary layer thickness is observed near the pressure side corner of the blade. The presence of secondary flow structures is clearly seen near the hub and tip on the blade suction side. The stator exit shows a qualitatively similar picture as the rotor exit. The stator wake is much thicker than the rotor and the secondary flow structures show radial migration and also occupy a larger fraction of the span. The stator exit hub boundary layer is thicker than the casing due to the larger turning and shock losses at the hub.

6.6.2 Averaged Profiles

A viscous through-flow solution was obtained by circumferentially averaging the three-dimensional flow field using equation (4.9). Figure 6-20 shows the spanwise variation

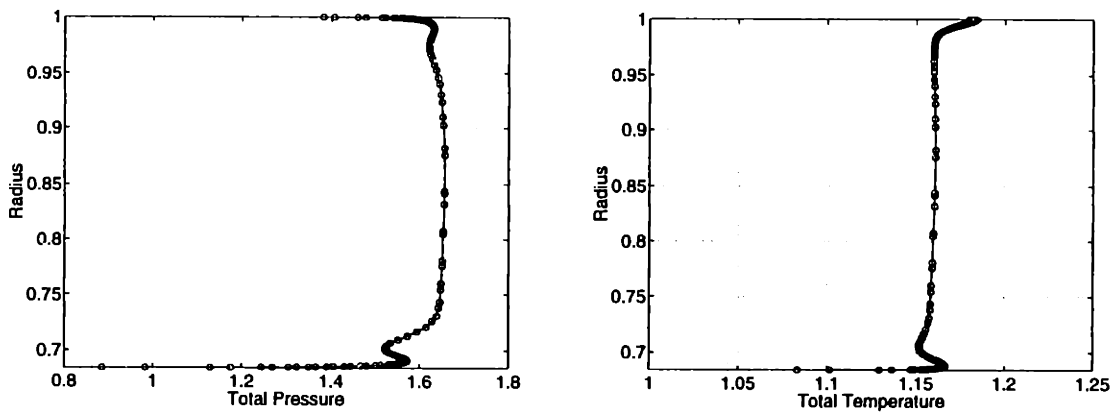

(a) Total Pressure

(b) Total Temperature

Figure 6-20: Low-speed stage rotor exit 3-D viscous mass averaged profiles.

of total pressure and temperature. The total pressure and total temperature profiles are almost constant along the span consistent with the free-vortex swirl distribution. The decrease in the profiles at 10% span from the hub is due to the secondary flow also seen in Figure 6-19. The presence of a weaker secondary flow is also observed near the tip as indicated by the slight reduction in pressure ratio at 95% span. The effect is smaller because of the thinner boundary layer due to circumferential casing suction slot upstream of the rotor. The total temperature increase at the tip is due to the swirl input by the rotating tip shroud.

Figure 6-21 shows the spanwise variation of the absolute Mach number and meridional Mach number. The absolute Mach number varies almost linearly except near the hub and tip where the endwall effects described above are present. A maximum Mach number of 1.1 is seen near the hub. The meridional Mach number is almost constant along the span. The blockage due to the secondary flow and boundary layer is clearly seen near the hub.

Figure 6-22 shows the spanwise variation of the rotor relative exit angle and loss. The exit angle shows an almost linear variation across the span except near the hub and casing where the effects of the endwall boundary layer and rotating shroud become significant. The crossover to negative flow angles occurs at 70% span. The loss profile, which is the entropy normalized by the freestream value, is almost uniform over most of the span and

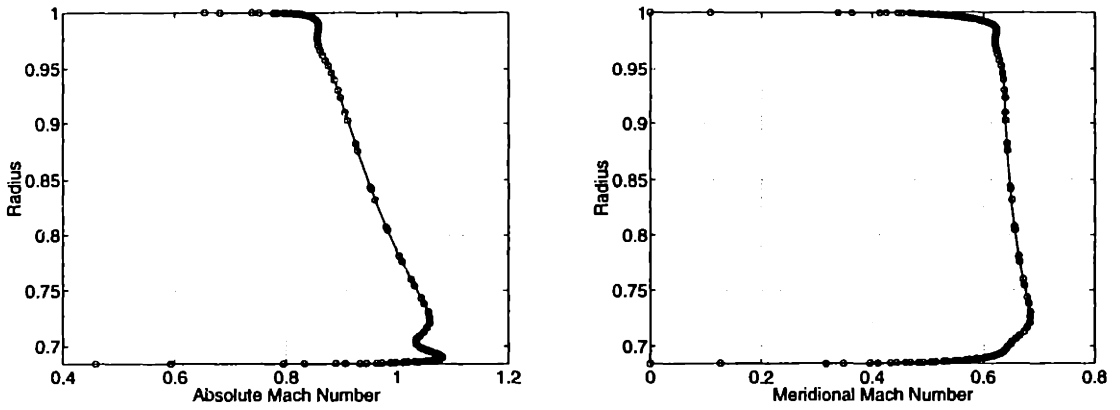

(a) Absolute Mach Number

(b) Meridional Mach Number

Figure 6-21: Low-speed stage rotor exit 3-D viscous mass averaged profiles.

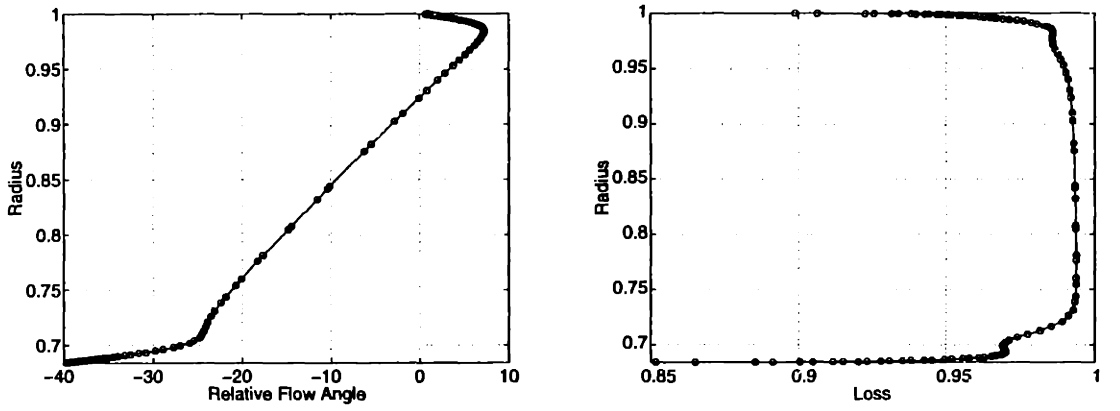

(a) Relative Flow Angle

(b) Loss

Figure 6-22: Low-speed stage rotor exit 3-D viscous mass averaged profiles.

is less than 4%. The hub shows a higher loss than the tip despite the presence of a strong shock near the tip.

Figure 6-23 shows the spanwise variation of total pressure and temperature at the stator exit. The total pressure profile between 50% and 70% span shows an almost uniform pressure ratio of 1.62. Between 10% and 50% span there is a decrease in pressure ratio which can be attributed to the secondary flow which persists and migrates radially through the

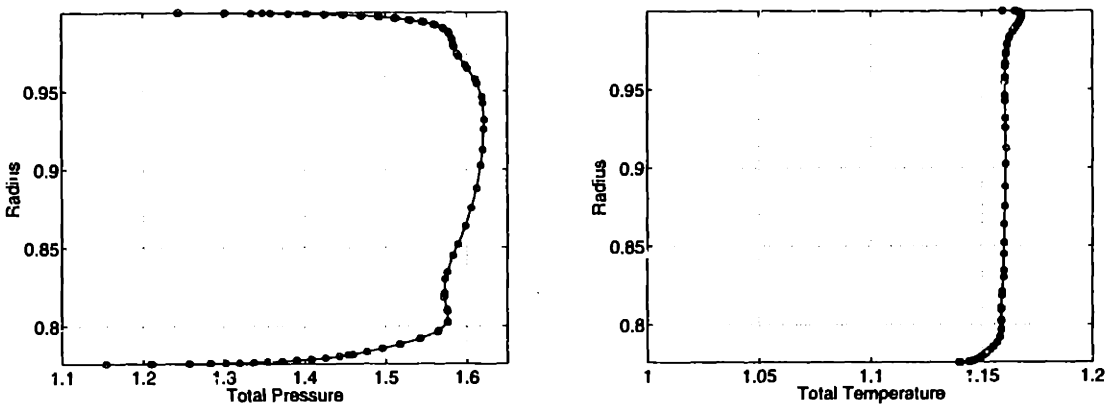

(a) Total Pressure

(b) Total Temperature

Figure 6-23: Low-speed stage stator exit 3-D viscous mass averaged profiles.

stator. Below 10% span the total pressure drops off rapidly indicating a high loss region due to the strong passage shock and subsequent thickening of the boundary layer. The absence of a circumferential suction slot contributes to the growth of the endwall boundary layer downstream of the passage shock. The decrease in total pressure near the tip can also be attributed to the endwall boundary layer, secondary flow, and shock losses. The total temperature spike at the tip due to the rotating shroud is seen to persist through the stator.

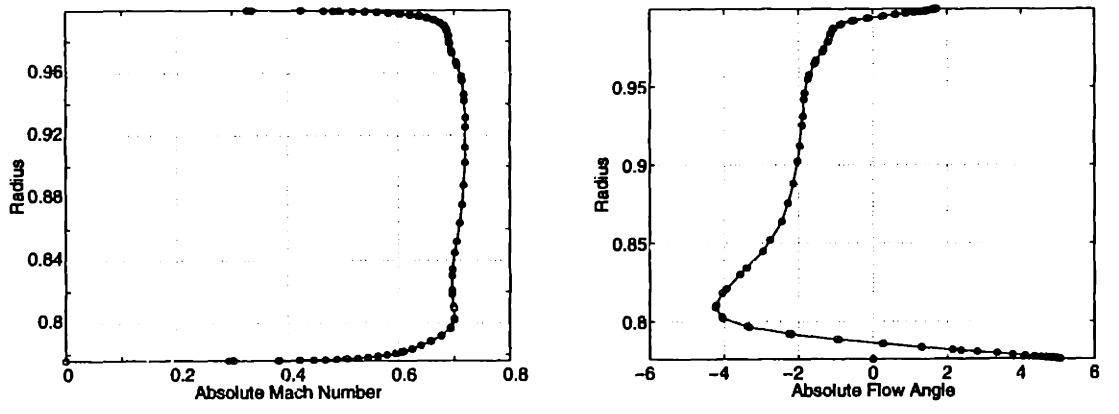

(a) Absolute Mach Number

(b) Absolute Flow Angle

Figure 6-24: Low-speed stage stator exit 3-D viscous mass averaged profiles.

Figure 6-24 shows the spanwise variation of the absolute Mach number and flow angle. The exit Mach number is almost constant at 0.7. The flow angle profile shows an under turning of the flow very close to the hub followed by a large overturning of $-4°$ at 10% span due to the secondary flow. An almost constant turning of $-2°$ is seen from 40% to 70% span followed by a slight decrease in turning due to separation. Finally, some underturning is seen in the tip endwall region.

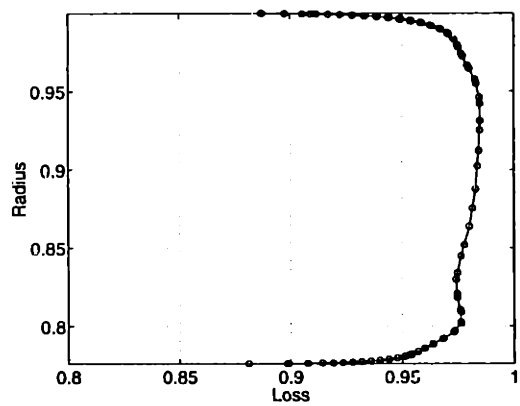

Figure 6-25: Low-speed stage stator exit 3-D viscous mass averaged loss profile.

Figure 6-25 shows the variation in loss along the span. The overall loss decrement is higher in the stator than the rotor, and the loss variation along the span is consistent with the endwall flow features described above.

6.6.3 Rotor and Stage Design Speed-Lines

Speed-lines calculated by NASA and P&W at design tip speed are shown in Figure 6-26. The P&W calculations were carried out by Saxena and Lord [44]. The NASA calculation shows a consistently higher pressure ratio than the P&W calculation. The stage shows a small mass flow range between choke and maximum pressure rise. This can be attributed mainly to the off-design operation and choking of the stator. The P&W calculation shows a much larger decrease in pressure ratio with decreasing mass flow than the NASA calculation. The decrease in pressure ratio past the peak pressure rise does not necessarily indicate that the stage has stalled because the high blade loading and turning past the ax-

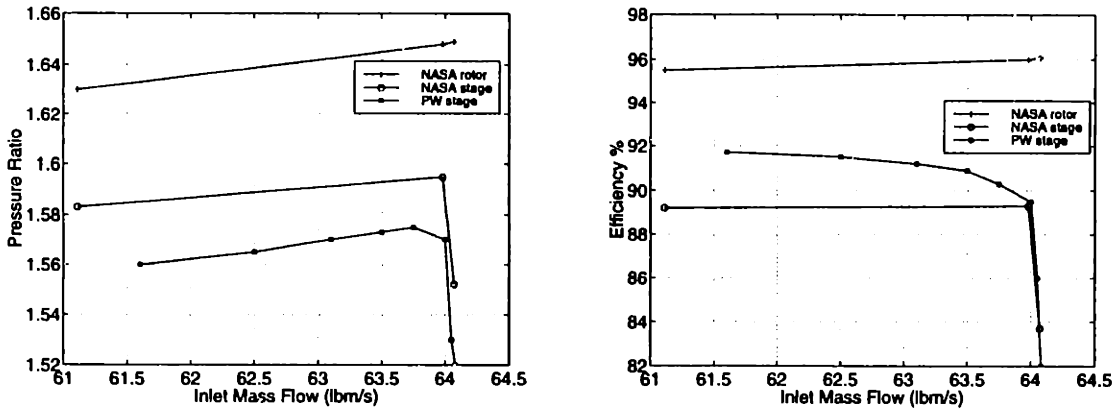

Figure 6-26: Low-speed stage speed-line

	Peak Pressure Ratio		Peak Efficiency	
	PR	η	PR	η
NASA	1.59	89.3	1.59	89.3
P&W	1.57	90.3	1.56	91.7

Table 6.3: Comparison of peak pressure ratios and efficiencies.

ial direction over 80% of the blade span. The efficiency shows a sharp increase up to the unchoke point and continues to increase despite the decrease in pressure rise. The efficiency begins to level of at a mass flow of 61 lbs/s indicating possible stall of the stage. The rotor total pressure rise curve shows a positive slope, as expected, and also shows an increase in efficiency with increasing mass flow rate. The rotor has a mass averaged pressure ratio of 1.65 and isentropic efficiency of 96% at a mass flow of 64 lbs/s which is in good agreement with the efficiency prediction from the quasi 3-D calculation. The stall and choke points of the rotor in isolation were not calculated. The stalling mass flow of the stage is expected to be close to 61 lbs/s. The maximum pressure ratios and efficiency from the speed lines is shown in Table 6.3. It is interesting to note that the peak pressure rise and peak efficiency in the NASA calculation are obtained at the same mass flow whereas the P&W calculation shows a peak efficiency at a much lower pressure ratio and mass flow.

The differences observed in the two calculations can be attributed to the differences in the solvers – primarily the type of grid, numerical scheme, and turbulence model. The simpler grid used by NASA required the suction slot to follow a fixed spanwise grid line resulting in a deviation of the slot location from the design intent. The P&W calculation utilized a more flexible grid generation procedure which resulted in a closer match with the intended slot location.

Chapter 7

High-Speed Stage

In contrast to the low-speed stage, the high-speed stage demonstrates the feasibility of increasing the pressure ratio by a factor of two at supersonic tip speeds. A unique feature of the high-speed stage is the location of the passage shock in the forward portion of the blade resulting in 50% to 60% chord length for subsonic diffusion. This design also demonstrates the possibility of controlling boundary layer behavior despite the presence of strong shocks with a feasible amount of suction.

This chapter discusses the high-speed stage design in detail. The important stage design parameters are presented followed by a brief description of the suction configuration. The quasi 3-D blade section calculations are discussed next followed by results of the 3-D inviscid and viscous calculations.

7.1 Stage Design Parameters

A summary of the high-speed stage design parameters are presented in Table 7.1. The total pressure ratios across the rotor and stage are spanwise averages calculated from mixed out flow conditions from each quasi-3D streamsurface solution. The suction requirement for both rotor and stator are based on the stage inlet mass flow. The area used to report the mass flow is based on the rotor face r_{hub}/r_{tip}. The diffusion factors are calculated

Tip Speed U(ft/s)	1500
Rotor Pressure Ratio	3.70
Stage Pressure Ratio	3.50
Mass Flow/Area (lbm/ft^2/s)	42.5
Rotor face Axial Mach Number	0.65
Stator Exit Mach Number	0.50
Rotor Tip Rel. Mach Number	1.50
Stator Hub Abs. Mach Number	1.41
Rotor Face (r_{hub}/r_{tip})	0.40
Suction Mass %	1.5/2.0
Max. Diffusion Factor (rot/stat)	0.76/0.78
Rotor Tip Solidity	2.14
Stator Hub Solidity	3.2
Rotor Isentropic Efficiency	94%
Stage Isentropic Efficiency	89%
Tip Blade Loading $\left(\Delta H/U_{tip}^2\right)$	0.7

Table 7.1: High-Speed Stage Design Parameters

using Equation (2.6), and the solidities are based on blade chord in the $m' - \theta$ plane. The isentropic efficiencies reflect only the losses in the blade wakes.

7.2 Suction Configuration

7.2.1 Quasi 3-D

In the quasi 3-D calculation, the rotor requires 1.5% suction on the spanwise blade slot starting at 40% span up to the tip. The stator requires 2.0% on the spanwise slot which extends from hub to tip. A suction coefficient of 2% was prescribed in the rotor and stator calculations for each streamsurface which required suction.

7.2.2 3-D Viscous

In the rotor viscous calculation, 1.3% suction was prescribed on the blade slot from 50% span up to the tip, 1% on the casing circumferential slot at the shock impingement location, and 1% on a chordwise slot extending from 70% – 90% chord located on the blade suction side near the tip shroud. The suction requirement and locations other than the spanwise blade suction prescribed by the quasi 3-D calculation were modified as required during the course of the various viscous calculations.

7.3 Through-Flow Solution

Through-flow solution pressure contours and meridional view of the flowpath are shown in Figure 7-1. The hub profile is approximately parabolic in shape upstream of the rotor and varies linearly across the rotor. The hub ramp angle is 33° across the rotor and 12° across the stator. A 5% reduction in flow area across the rotor is designed into the casing profile to lower the static pressure rise across the rotor, and also to control the excessive

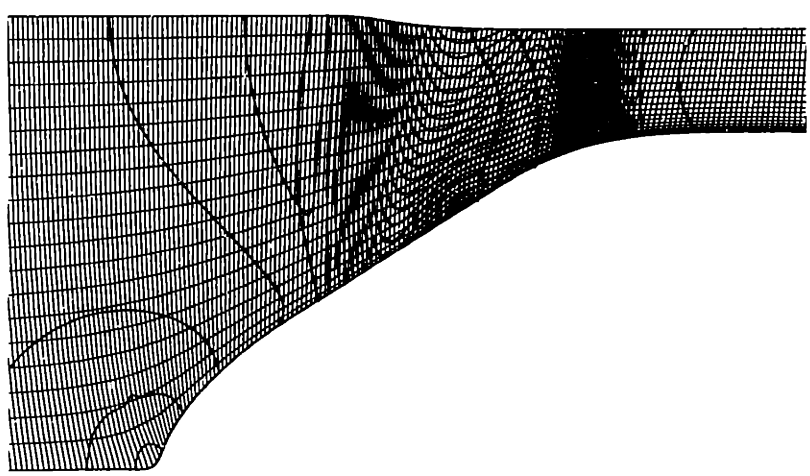

Figure 7-1: High-speed stage through-flow solution pressure contours.

growth of the tip shroud boundary layer. The tip flowpath profile is shaped to provide some pre-compression up to the shock impingement location. The minimum axial distance between rotor and stator is 0.65" based on a tip radius of 10.34". The axial distance was

fixed based on a suggested value by Pratt & Whitney and instrumentation requirement of the NASA compressor test facility. The high solidity of the stator at the hub and tip results in a leading edge contour which maintains an almost constant axial distance with the rotor along the entire span, and also provides sweep near the hub suitable for the supersonic conditions at the hub [58].

The pressure contours show the higher static pressure rise across the stator compared to the rotor. A region of low static pressure rise is seen from the rotor mid-chord up to stator mid-chord near the hub, which can be attributed to the low reaction in the hub region.

7.4 Quasi 3-D Solutions

7.4.1 Rotor Hub

The isentropic Mach number on the blade and blade to blade pressure at the rotor hub are

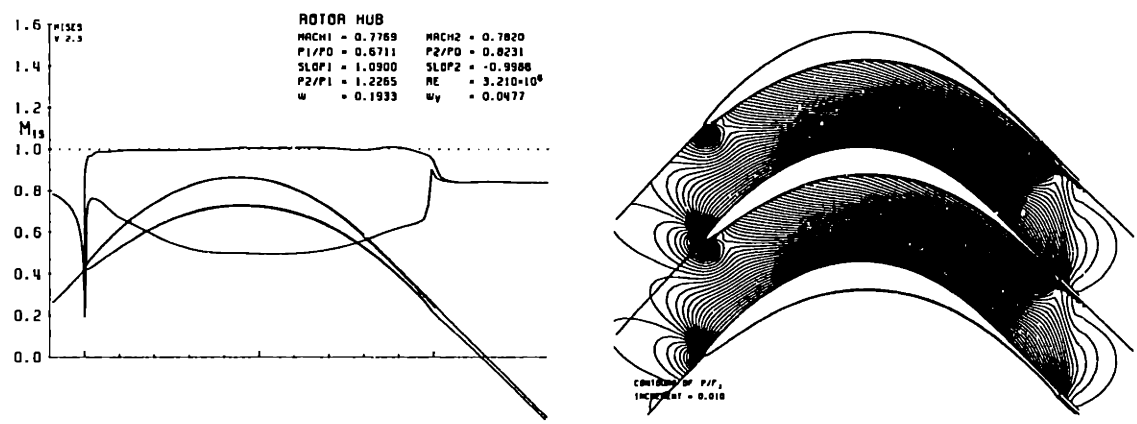

(a) Isentropic Mach Number

(b) Contours of Pressure

Figure 7-2: High-speed stage rotor hub.

shown in Figure 7-2. The static pressure ratio is 1.24. A sonic Mach number is maintained over most of the suction surface terminating in a very short pressure recovery region. Although the delay in pressure recovery leads to a larger profile loss, the possibility of separation due to interaction with the hub boundary layer and secondary flow features are

minimized by delaying the pressure recovery. The pressure side shows an adverse pressure gradient up to mid-chord and uniform blade loading up to the trailing edge. The large acceleration on the pressure side is due to the diverging trailing edge which is used in this instance mainly to relieve the adverse pressure gradient on the suction surface. The blade to blade pressure contours show a shock-free uniform blade loading along the chord, and also provides a view of the high solidity and large turning requirement.

7.4.2 Rotor 65% Span

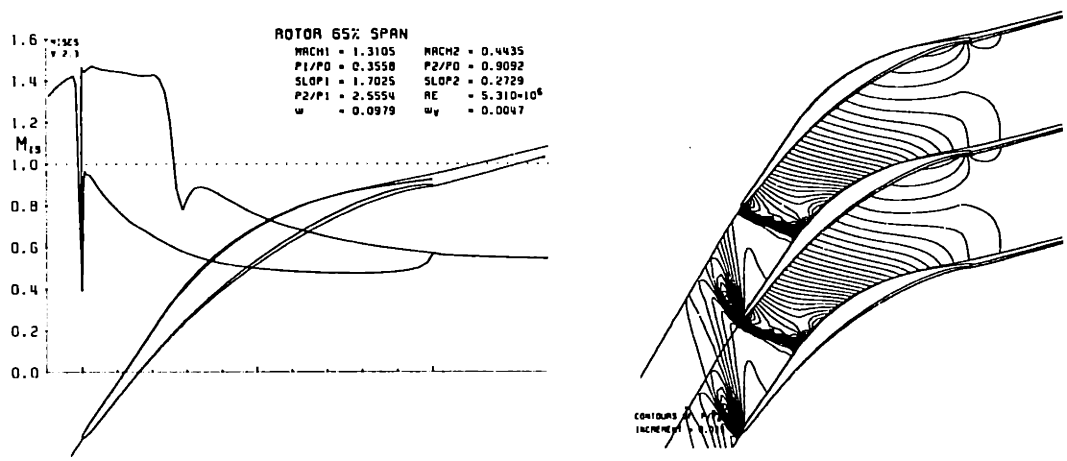

(a) Isentropic Mach Number

(b) Contours of Pressure

Figure 7-3: High-speed stage rotor 65% span.

Figure 7-3 shows the rotor 65% span section isentropic Mach number distribution and blade to blade pressure contours. This section illustrates the transition from the lower span shock-free sections to the high Mach number sections with a passage shock. The inlet relative Mach number is 1.31 and static pressure ratio is 2.55. The total loss is dominated by the losses due to the bow shock and passage shock. The Mach number distribution shows a weak compression leading to the passage shock. The effect of the suction is visible in the additional decrease in the Mach number at the foot of the shock. This is followed by a mildly concave pressure recovery region. The pressure side shows a relatively strong adverse pressure gradient up to mid-chord followed by a region of constant loading up

to the trailing edge. The blade shows a thick leading edge region and relatively large maximum thickness compared to conventional blade sections designed for the same inlet Mach number. The blade to blade pressure contours show the shock structure and the effect of the suction slot. The foot of the passage shock is drawn toward the suction slot. This affect is small for this section since the suction slot is close to the shock. The pressure contours also show the uniform pressure rise in the subsonic region.

7.4.3 Rotor Tip

Figure 7-4 shows the rotor tip section isentropic Mach number distribution and blade to blade pressure contours. The inlet relative Mach number is 1.5 and static pressure ratio is 2.75. The peak total pressure ratio for this section is 3.81. The shock loss is similar in

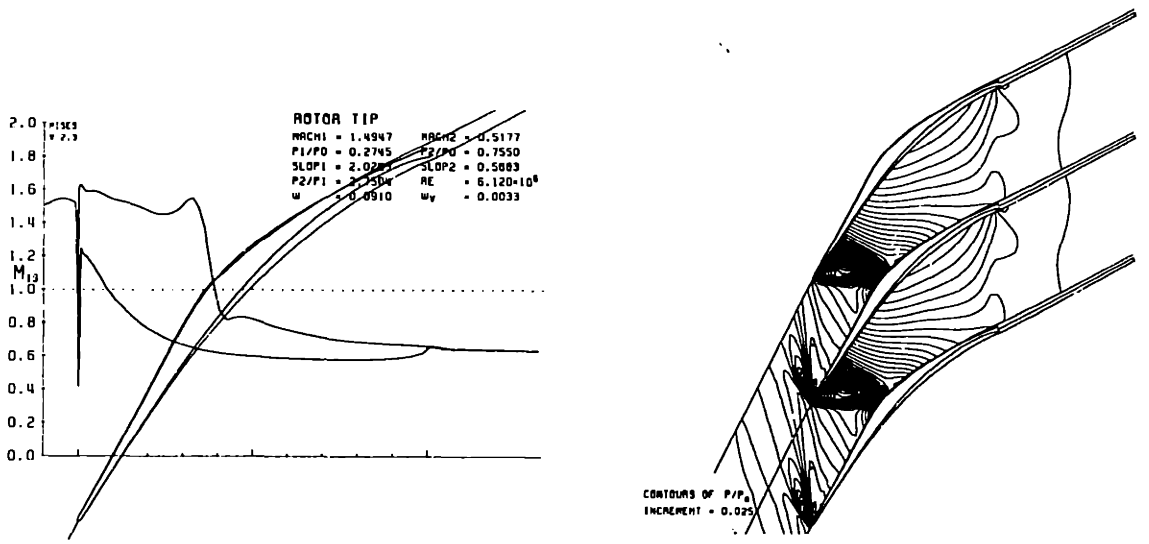

(a) Isentropic Mach Number

(b) Contours of Pressure

Figure 7-4: High-speed stage rotor tip.

magnitude to the 65% span section. The modest shock loss despite the higher inlet Mach number can be attributed to the stronger pre-compression. The diffusion factor is 0.76 and is the highest level for the entire rotor. The suction slot is located downstream of the shock and is followed by a relatively mild pressure recovery region. The pressure surface

shows a fairly strong adverse pressure gradient up to 40% chord followed by a constant Mach number section up to the trailing edge. The increase in loading due to the diverging trailing edge is diminished to the due to unusually thick pressure side boundary layer. The blade to blade pressure contours present a clear picture of the shock structure. The passage shock coalesces with the bow shock just downstream of the maximum thickness. The pressure surface is shaped to weaken the effect of the passage shock on the boundary layer. A significant portion of the blade is devoted to subsonic turning which in this case is 33°. The blade shape is considerably thicker than conventional supersonic blades design for the same inlet Mach number. The leading edge radius is small but the blade thickness increases in the pre-compression region.

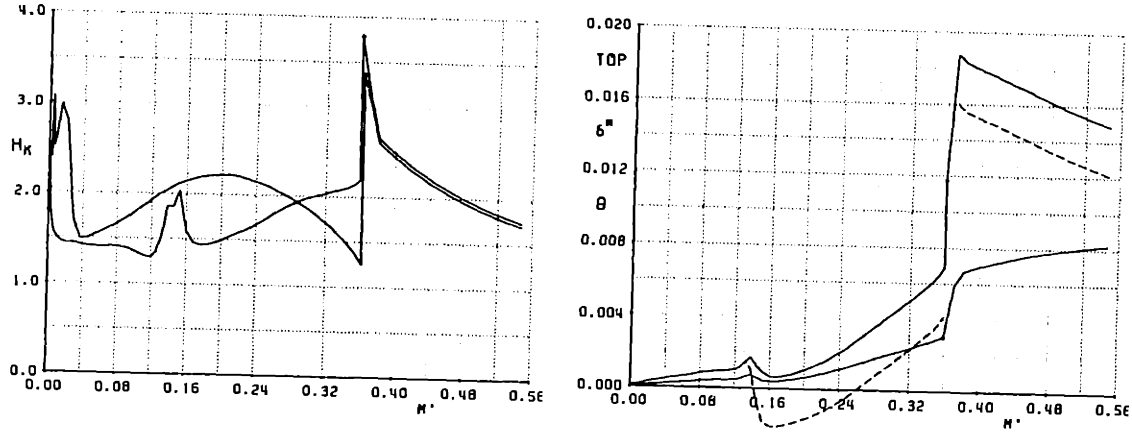

(a) Kinematic Shape Parameter

(b) Suction Side δ^* and θ

Figure 7-5: High-speed stage rotor tip boundary layer profiles. Dashed line is $\delta^* - \dot{m}_{\text{suct}}/\rho_e u_e$ (removed streamtube height).

Figure 7-5 shows the shape parameter H_k distribution and boundary layer profile on the suction surface. The shape parameter on the suction side is almost constant in the pre-compression region and undergoes an increase across the shock. The effect of suction in controlling the rapid increase in H_k is seen. The H_k growth is almost linear in the pressure recovery region. The pressure side H_k shows an increase due to the strong adverse pressure gradient and then begins decreasing in the almost zero pressure gradient section up to the trailing edge. The effect of suction in decreasing the displacement and momentum

thickness is clearly seen. The suction mass defect ratio $(\delta^*_{\text{suct}}/\delta^*_1) \sim 2$ – twice the requirement of the low-speed stage.

7.4.4 Stator Hub

Figure 7-6 shows the stator hub section isentropic Mach number distribution and blade to blade pressure contours. The absolute inlet Mach number is 1.45, static pressure ratio

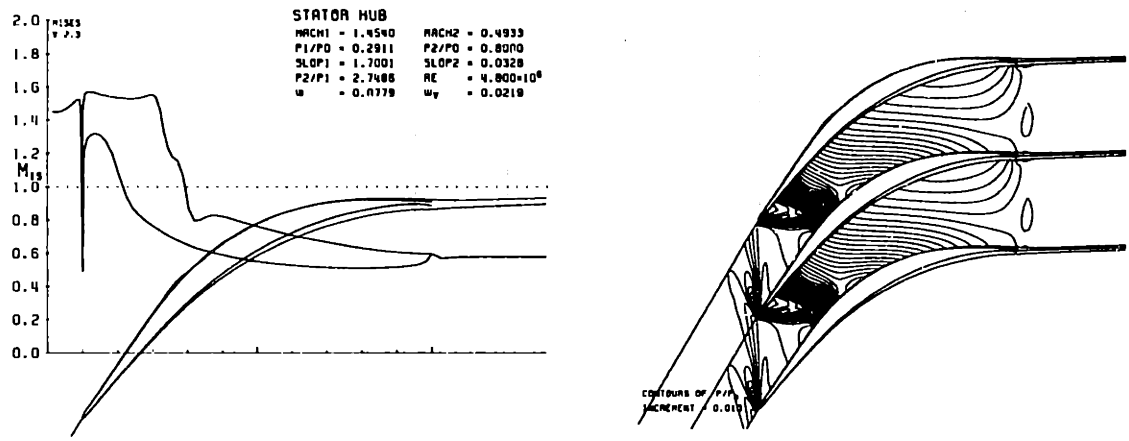

(a) Isentropic Mach Number

(b) Contours of Pressure

Figure 7-6: High-speed stage stator hub.

is 2.75, and turning angle is 59°. The static pressure ratio and losses are close to those of the rotor tip section, and this is partly due to the free vortex spanwise swirl profile. The diffusion factor is 0.72. The Mach number distribution shows a weak compression followed by the passage shock and suction downstream. The pressure recovery is fairly mild despite the large turning. This can be attributed to the large streamtube contraction (AVDR) across the stator. The Mach number distribution on the pressure side shows the effect of the passage shock impingement just downstream of the leading edge followed by an adverse pressure gradient up to 60% chord. A constant blade loading is maintained from there up to the trailing edge. The blade to blade pressure contours show the shock structure. The passage shock is well inside the blade passage and impinges strongly on

both suction and pressure sides. The foot of the passage shock is drawn toward the suction slot resulting in an inclination of the passage shock. The large turning and high blade solidity are also seen.

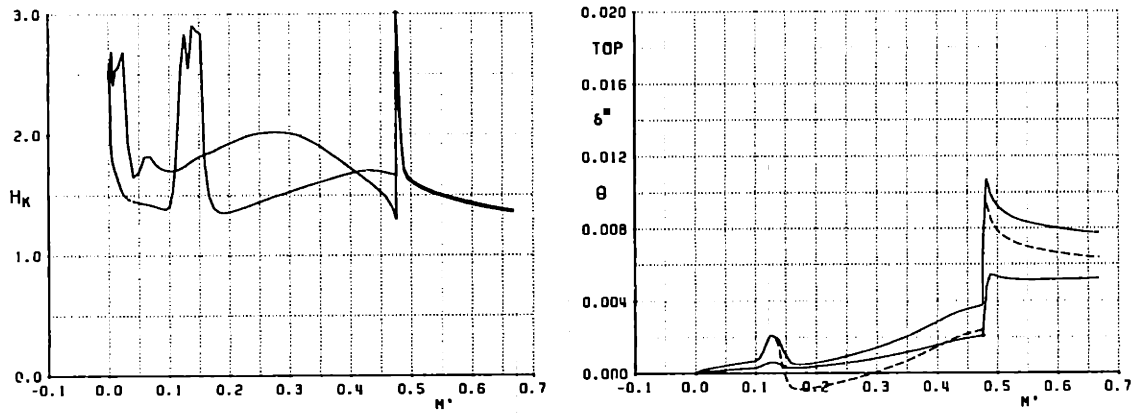

(a) Kinematic Shape Parameter

(b) Suction Side δ^* and θ

Figure 7-7: High-speed stage stator hub boundary layer profiles. Dashed line is $\delta^* - \dot{m}_{\text{suct}}/\rho_e u_e$ (removed streamtube height).

Figure 7-7 shows the shape parameter H_k distribution and boundary layer profile on the suction surface. The suction surface shape parameter shows a rapid increase at the shock impingement location, and excessive growth is prevented by the suction. The variation in H_k is almost linear downstream of the slot in the subsonic region. The pressure surface H_k shows a small increase near the passage shock impingement. This was considerably reduced by shaping the pressure surface. A small growth in H_k is observed in the adverse pressure gradient downstream of the shock. The effect of suction in decreasing the displacement and momentum thickness is clearly seen, and the suction mass defect ratio $(\delta^*_{\text{suct}}/\delta^*_1) \sim 2$.

7.4.5 Stator Mid-Span

The stator mid-span blade surface Mach number and blade to blade pressure contours are shown in Figure 7-8. A dramatic change is observed between the flow conditions at the

hub and the relatively benign conditions at mid-span. The absolute inlet Mach number is 1.18 and the static pressure ratio is close to 2. The shock strength is considerably lower and virtually no pre-compression is used upstream of the shock. The effect of the suction slot is seen downstream of the shock. In contrast to the hub section where the suction

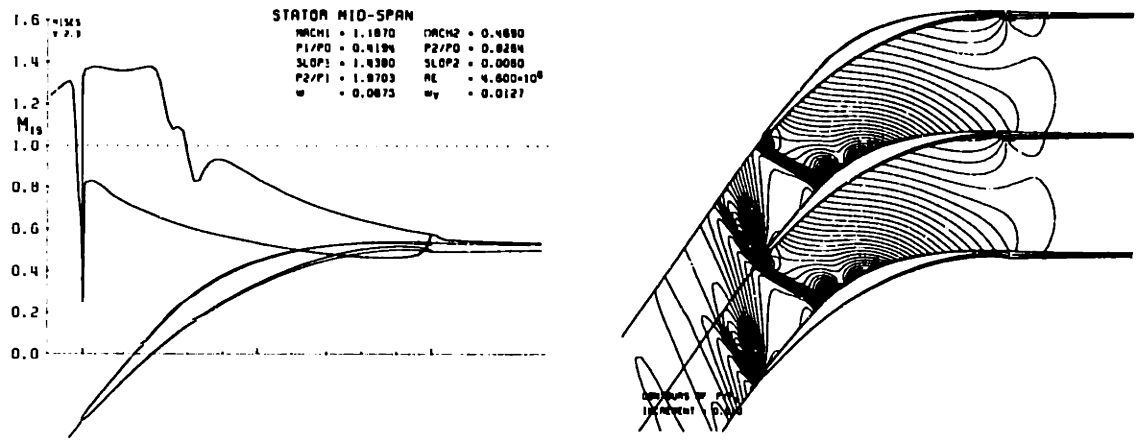

(a) Isentropic Mach Number

(b) Contours of Pressure

Figure 7-8: High-speed stage stator mid-span.

was used to prevent separation due to the shock, the weaker shock in this case allows the suction slot to be moved downstream from the shock to control the subsonic development of the boundary layer. The typical pressure recovery region is downstream of the suction slot. The pressure side shows a relatively mild adverse pressure gradient compared to the stator hub almost up to the trailing edge. The blade to blade pressure contours show the shock structure and the suction slot can be clearly seen downstream of the shock. This section shows a close resemblance with the rotor mid-span.

7.4.6 Stator Tip

Figure 7-9 shows the stator tip section isentropic Mach number distribution and blade to blade pressure contours. This is the most unusual section in the stage requiring as much turning as the stator hub. The high inlet angle is due to the large swirl contribution from

the rotor tip shroud. The inlet conditions for this section were taken from the 3-D viscous calculation. The effect of the rotating shroud is more pronounced than in the low-speed

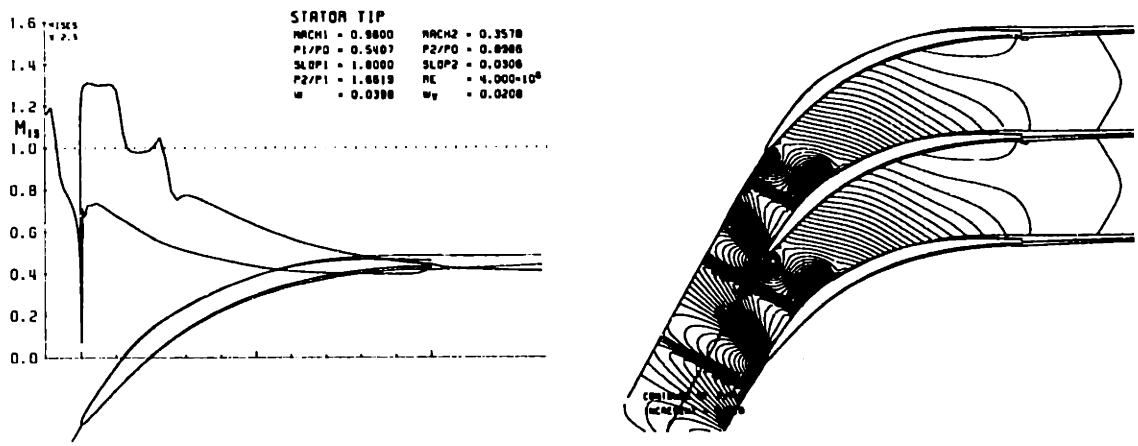

(a) Isentropic Mach Number

(b) Contours of Pressure

Figure 7-9: High-speed stage stator tip.

rotor due to larger exit angle and higher blade speed of the high-speed rotor. The absolute inlet Mach number is just below sonic and the pressure ratio is 1.66, and the exit Mach number is relatively low at 0.35. The diffusion factor is 0.78 – the highest for the stage. The suction side Mach number distribution shows a weak shock at 10% chord. The suction is another 10% chord downstream followed by a relatively long pressure recovery region. The pressure side shows a mild adverse pressure gradient up to the trailing edge. The blade to blade pressure contours show the shock and suction slot location. This section has a relatively low AVDR of 1.15 compared to 1.25 at mid-span which results in a higher solidity requirement despite the suction.

The shape parameter distribution and boundary layer growth on the suction side are shown in Figure 7-10. The suction side shape parameter shows a small increase across the shock, but mostly increases in the subsonic pressure recovery region. The pressure side shape parameter shows very little variation except for a small increase near mid-chord. The effect of suction in decreasing the displacement and momentum thickness is clearly seen, and the suction mass defect ratio $(\delta^*_{\text{suct}}/\delta^*_1) \sim 2$.

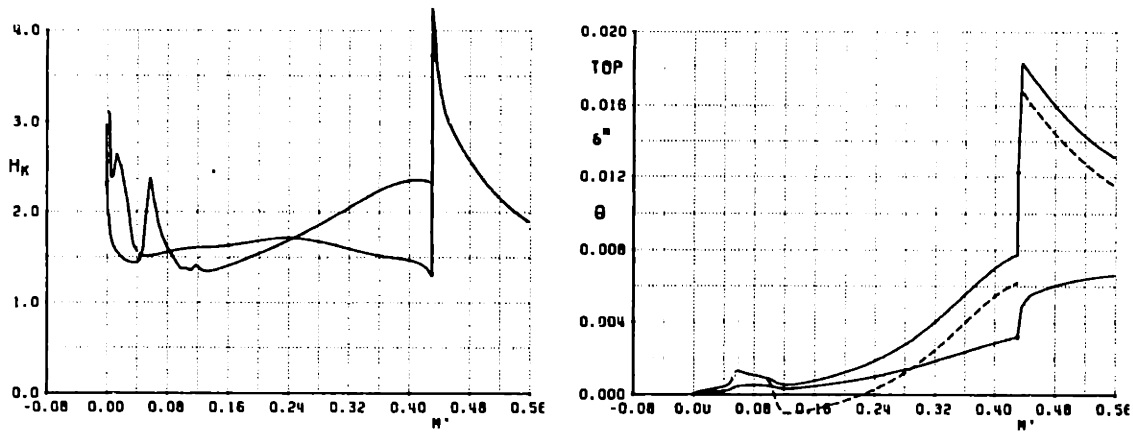

(a) Kinematic Shape Parameter

(b) Suction Side δ^* and θ

Figure 7-10: High-speed stage stator tip boundary layer profiles. Dashed line is $\delta^* - \dot{m}_{suct}/\rho_e u_e$ (removed streamtube height).

7.5 3-D Euler Rotor Solution

The rotor Euler calculation was performed at approximately the design back pressure. A tetrahedral grid with 83000 points and 430000 elements was used. The effect of suction was not modeled in the calculation. The back pressure was matched instead of the mass flow since the effect of blockage due to the blade boundary layers is not modeled in the inviscid calculation.

Figure 7-11 shows the pressure contours on the rotor suction and pressure sides. An interesting feature of this design is that the shock extends up to mid-span which is also the location where the rotor relative exit angle is zero. Very little forward sweep of the shock is observed which is mainly due to the contraction of the casing profile since the shock impingement must be normal to the casing. The shock is located downstream of the maximum thickness due to the absence of viscous effects. Downstream of the shock the pressure rise is uniform along most of the span. Acceleration of the flow near the hub mid-chord is seen. This is not observed in the quasi 3-D calculation shown in Figure 7-2 and may be attributed again to the different level of blockage. The contours on the pressure side show the impingement of the passage which weakens below 70% span. Downstream

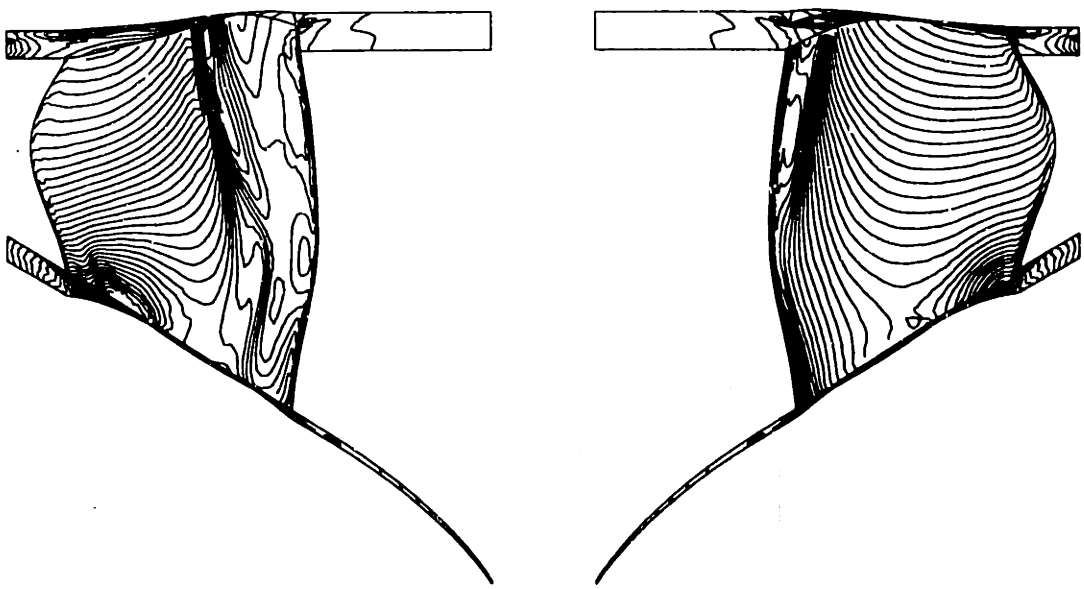

(a) Suction Side Contours of Pressure (b) Pressure Side Contours of Pressure

Figure 7-11: High-speed stage rotor 3-D Euler solution.

of the shock the pressure contours show the uniform loading also observed on the quasi 3-D sections. Acceleration of the flow is seen near the trailing edge in the hub region.

Figure 7-12 compares the flow features between the 3-D Euler calculation and an inviscid quasi 3-D calculation of the rotor tip section. A good overall agreement is seen in the shock location and pressure contours. The bow shock is not well resolved due to the coarse grid in the passage. The diverging trailing edge is closed in the 3-D Euler calculation. The 3-D Euler solution shows reflections of pressure waves from the exit boundary which is less than 1 chord downstream in order to prevent choking at the exit plane. This did not affect the convergence rate or overall solution in any manner.

7.6 3-D Viscous Rotor Solution

The results of the rotor 3-D viscous analysis presented in this section were calculated using the APNASA code, described in section 4.7, by Adamczyk and Celestina. The grid used

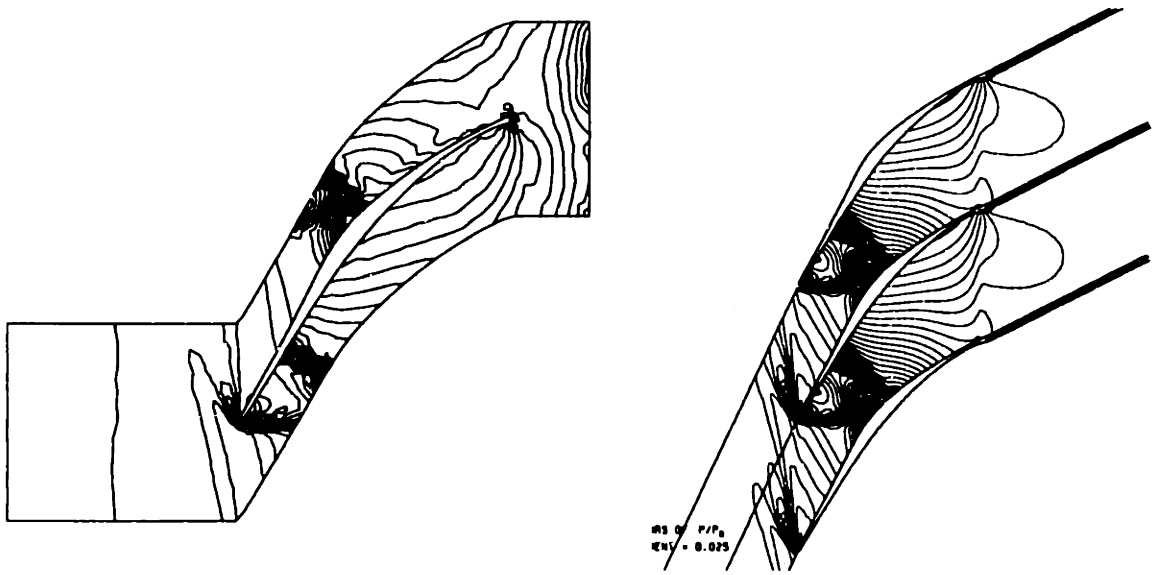

(a) 3-D Euler Contours of Pressure

(b) Inviscid quasi 3-D Contours of Pressure

Figure 7-12: High-speed stage rotor tip inviscid quasi 3-D Euler comparison.

for the calculation has 199 axial, 51 circumferential, and 51 spanwise points. The design suction slot location was not matched exactly in the viscous calculation because the code requires the slot to be specified along a constant spanwise grid line. The slot location was matched exactly at the tip and followed the specified grid line up to 50% span. Similar to the low-speed stage, the blade geometry was altered by fitting leading edge and trailing circles to meet grid generation constraints, and the diverging trailing edge was not completely resolved.

7.6.1 Design Point Solution

The solution presented below, designated as the design point, was calculated at an inlet mass flow of 80.9 lbs/s and showed the highest pressure rise and efficiency. The mass averaged pressure ratio is 3.67 with an isentropic efficiency of 94%. A total suction of 3.3% of the inlet mass flow was prescribed on the blade and casing as described in section 7.2.

7.6.1.1 Rotor Hub

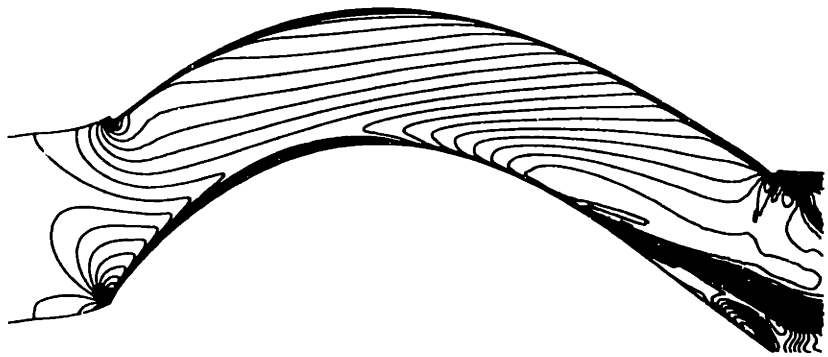

Figure 7-13: High-speed stage rotor hub 3-D viscous relative Mach contours.

Figure 7-13 shows the relative Mach number contours at the rotor hub. A region of supersonic flow is seen in the forward portion of the blade up to 15% chord. This indicates that the incidence is higher than the design intent and may be attributed to the hub boundary layer which is absent in the quasi 3-D calculation. The contours also clearly show a region of separation starting at 80% which is due to the exacerbation of the blade and hub boundary layers in the large acute angle between the blade suction surface and the hub. This can be seen in the rotor exit wake Figure 7-17. The contours indicate a thin boundary layer on the remaining length of the suction side and all of the pressure side.

7.6.1.2 Rotor 65% Span

Figure 7-14 shows the rotor relative Mach number contours at 65% span. The location of the passage shock indicates that the blade is unchoked at this span location. The shock location is in good agreement with the quasi 3-D calculation shown in Figure 7-3. The effect of suction is seen downstream of the shock and the slot is located further downstream than the quasi 3-D calculation. The boundary layer on the suction surface shows excessive growth downstream of the suction slot compared to the quasi 3-D calculation. This growth will decrease if the slot is moved closer to the shock as intended in the quasi 3-D design calculation. The build up of contours near the pressure side trailing edge show the effect of the diverging trailing edge.

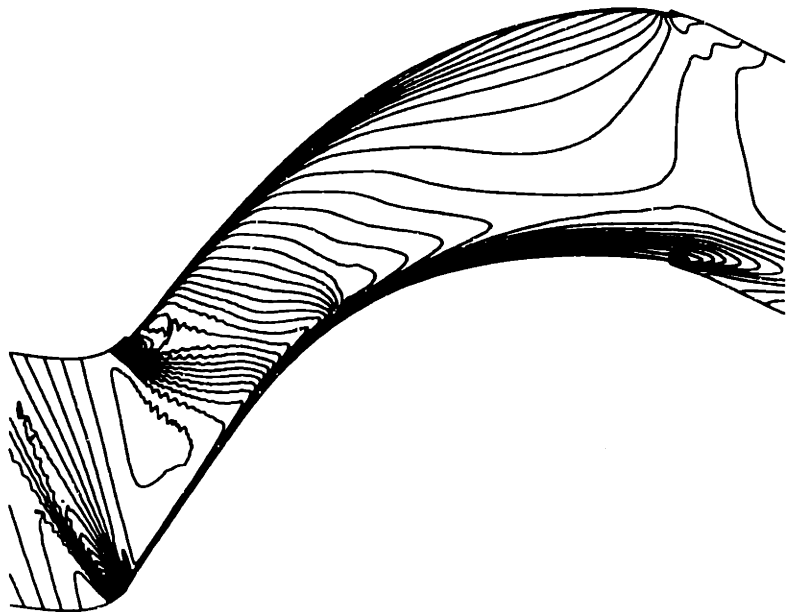

Figure 7-14: High-speed stage rotor 65% span 3-D viscous relative Mach contours.

7.6.1.3 Rotor Tip

Figure 7-15 shows the relative Mach number contours near the rotor tip approximately outside the influence of the casing boundary layer. The passage shock location coincides with the location of the suction slot similar to the quasi 3-D calculation shown in Figure 7-4. The interaction of the bow shock with the passage shock is also seen. The boundary layer on the suction side shows moderate growth whereas the boundary layer on the pressure side is relatively thicker due to the impingement of the passage shock on the pressure surface. This was also observed in the quasi 3-D calculation at lower than design back pressures. The passage shock in the 3-D calculation is deeper in the blade passage than the quasi 3-D calculation. The chordwise suction slot near the tip also plays an important role in preventing separation of the suction side boundary layer.

An interesting comparison is presented between the tip flow field at design conditions and close to stall in Figure 7-16. Close to stall the shock has moved out of the passage and the blade is unchoked, but the suction side boundary layer remains well attached.

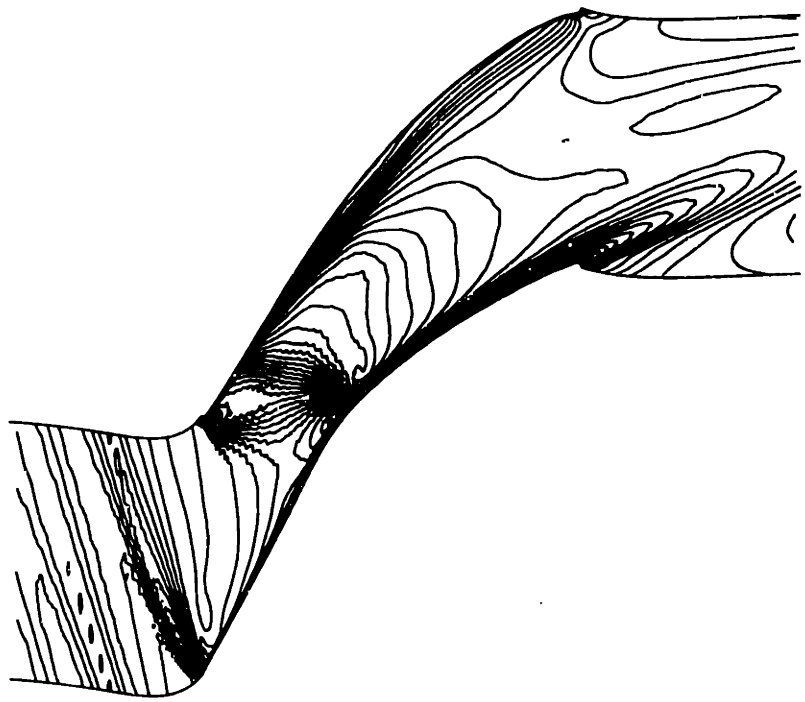

Figure 7-15: High-speed stage rotor tip 3-D viscous relative Mach contours.

The location of the suction slot can also be clearly seen. The pressure side boundary layer also shows improvement over the design condition. The APNASA code prescribes an exit pressure boundary condition, and the solution close to stall was calculated at a higher static pressure ratio than the design point. This indicates the possibility of the rotor operating satisfactorily even after it unchokes. Since the static pressure ratio characteristic has a negative slope with the passage shock upstream of the blade minimum area, the shock can be swallowed by decreasing the back pressure. This condition is necessary to establish started supersonic flow.

7.6.1.4 Rotor Wake

Figure 7-17 show the axial velocity contours at the rotor exit. The middle of the passage near the hub shows the separation from the blade suction side corner which migrates to the center of the passage. The rotor wake is fairly narrow up to 90% span. The casing

(a) Inlet Mass Flow = 80.90 lbs/s

(b) Inlet Mass Flow = 77.95 lbs/s

Figure 7-16: High-speed stage 3-D viscous suction rotor tip relative Mach contours.

boundary layer shows a significant growth due to the relatively high static pressure ratio of 2.75 across the tip. No separation, or regions of negative axial velocity are seen in the wake.

7.6.2 Averaged Profiles

A viscous through-flow solution was obtained by circumferentially averaging the three-dimensional flow field using equation (4.9). Figure 7-18 shows the spanwise variation of total pressure and temperature. The total pressure profile is almost constant at 3.68 over most of the span. The decrease near the hub is due to the separation of the suction side boundary layer. The rapid increase in pressure ratio close to the tip is due to the large tangential velocity imparted to the flow by the rotor shroud. This is also seen in the very large temperature ratio which is close to 1.65 predicted by Euler's equation. The total temperature profile is constant over most of the span and decreases below 10% span due to the lower turning as a result of the hub separation.

Figure 7-19 shows the spanwise variation of the absolute Mach number and meridional

Figure 7-17: High-speed stage rotor wake axial velocity contours.

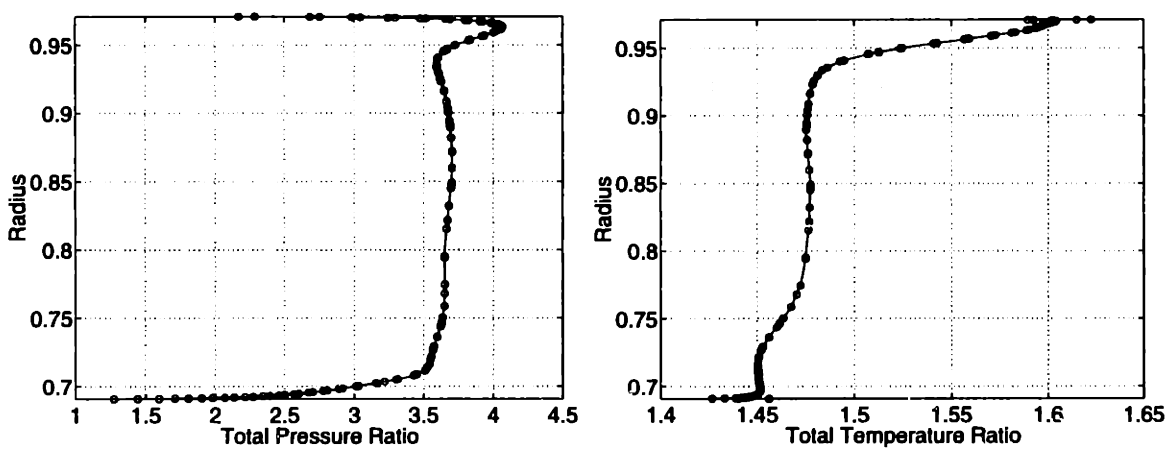

(a) Total Pressure

(b) Total Temperature

Figure 7-18: High-speed stage rotor exit 3-D viscous mass averaged profiles.

Mach number. The absolute Mach number peaks at 1.33 near the hub and decreases linearly up to 90% span. The increase in absolute Mach number near the tip is due to the large tangential velocity imparted by the shroud. The Mach number is also supersonic over the entire span, though the quasi 3-D calculation indicates that stator is choked from

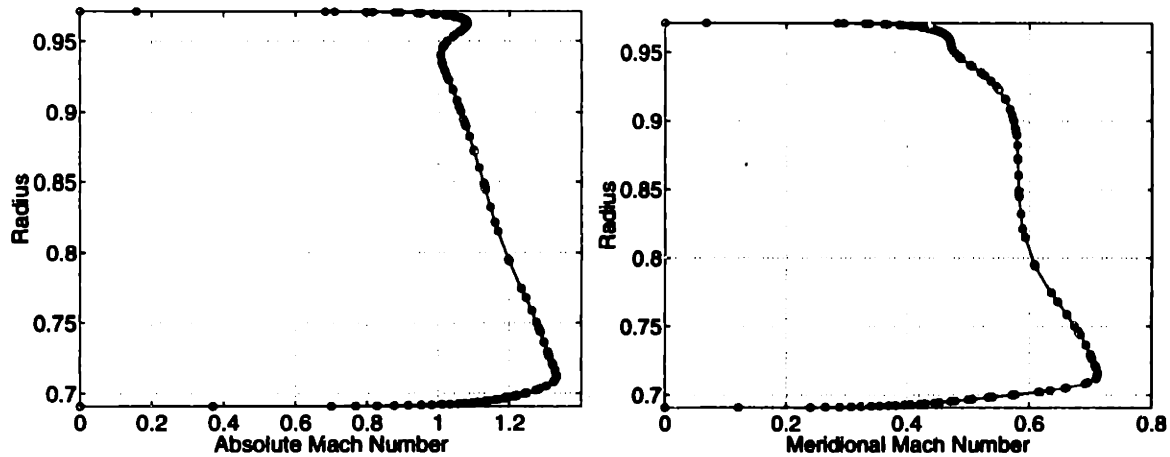

(a) Absolute Mach Number

(b) Meridional Mach Number

Figure 7-19: High-speed stage rotor exit 3-D viscous mass averaged profiles.

the hub up to approximately 30% span. The meridional Mach number shows a decrease at 45% span which coincides with the location where the flow angle is zero. This is purely a coincidence. The decrease in meridional Mach number can be attributed to thickening of the boundary layer since the blade slot is not extended below 50% span as in the quasi 3-D calculation. The lower meridional velocity in the tip region indicates the higher level of diffusion.

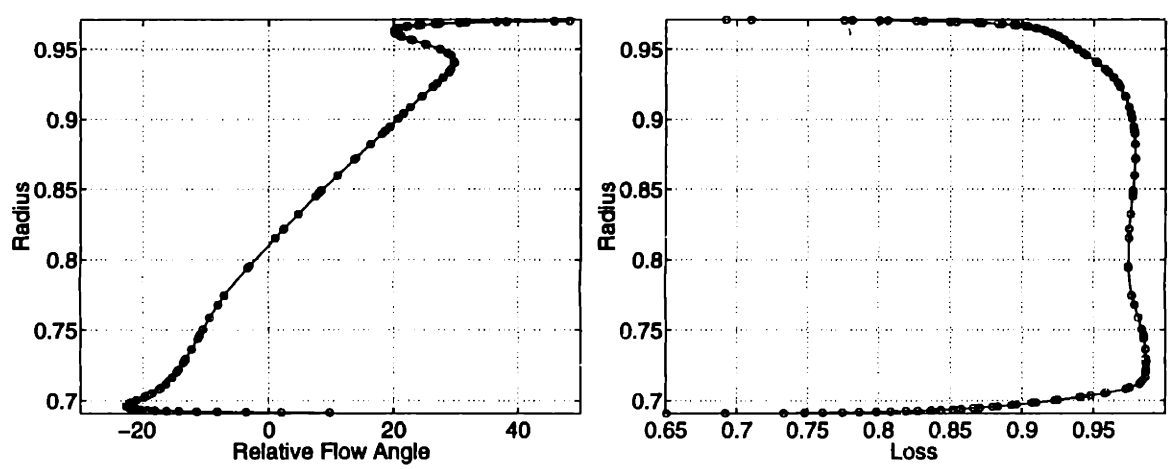

(a) Relative Flow Angle

(b) Loss

Figure 7-20: High-speed stage rotor exit 3-D viscous mass averaged profiles.

Figure 7-20 shows the spanwise variation of the rotor relative exit angle and loss. The exit angle shows an almost linear variation across the span except near the hub and casing where the effects of the endwall boundary layer and rotating shroud become significant. The cross-over to negative exit angles occurs at 45% span and a large negative flow angle of $-22°$ is observed near the hub. The loss profile is almost uniform over most of the span and is less than 4%. The loss increases significantly near the tip which can be attributed to the shock losses and large total temperature rise due to the work input by the rotating shroud.

7.6.3 Rotor Design Speed-Line

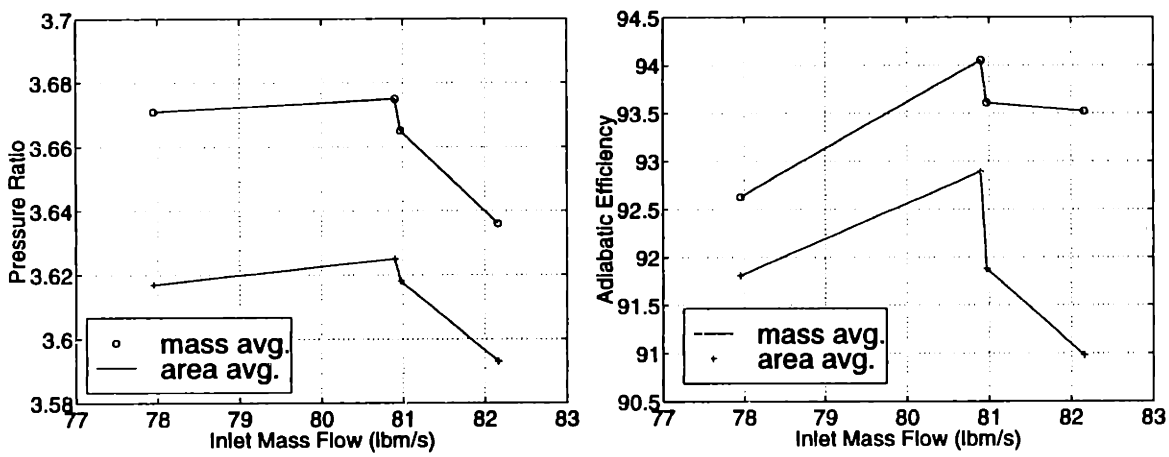

Figure 7-21: High-speed rotor speed-line

Figure 7-21 shows the rotor speed-line calculated at design blade speed. The pressure ratio achieves a maximum of 3.67 at a mass flow rate of 80.9 lbs/s. An almost constant difference is observed between the mass averaged and area averaged pressure ratio. The mass averaged adiabatic efficiency peaks at a maximum of 94% at 80.9 lbs/s, and stays above 90% at 82.16 lbs/s and close to stall. The difference between the mass averaged and area averaged efficiencies increases at the higher mass flow rate of 82.16 lbs/s can be attributed to the increase in separation or blockage, especially in the tip region. The peak efficiency predicted by the quasi 3-D calculation is in good agreement with the 3-

D viscous calculation although the mass flow rate of the 3-D calculation is lower. The efficiencies between the two calculations are close because the shock loss predicted by the quasi 3-D calculation is higher since it does not account for 3-D sweep of the shock across streamlines whereas the boundary layer losses in the 3-D calculation are higher than the quasi 3-D calculation. These two loss contributions balance each other between the two calculations.

Chapter 8

Conclusions and Recommendations

A methodology for the aerodynamic design of aspirated compressors has been developed and applied to the design of a low-speed and high-speed compressor stage. These stages produce twice the work of conventional compressor stages at a given tip speed, and as such demonstrate the validity of using aspiration as a means of increasing the compressor pressure ratio at a given tip speed.

8.1 Preliminary Design Study

The preliminary design study provided some essential insight into the potential of using aspiration on compressor stages. The design study showed that increasing the rotor pressure ratio, and consequently the blade loading, by a factor of two at a fixed blade speed could result in diffusion factors as high as 0.75. Adapting the diffusion factor concept to include the effects of suction, under the assumption that a new boundary layer originates downstream of the slot, indicates that the diffusion factor of 0.6 where the losses increase rapidly for conventional blades could be raised to 0.75 for aspirated blades. The rapid decrease in diffusion factor with flow coefficient suggests that lowering the tip speed and further increasing the blade loading should be investigated. Supersonic stator inlet Mach numbers will be inevitable for blade loading parameters above 0.7 expected in aspirated

compressor designs. The stator inlet Mach number could be lowered to some extent by the use of inlet guide vanes.

8.2 Boundary Layer Suction

The suction mass flow requirement was shown to be small, on the order of a few percent of the inlet mass flow. This is an important consideration from the systems perspective of integrating an aspirated compressor into an engine, and for meeting structural constraints since the suction mass flow requirement will determine the cross-sectional area of the suction passages within the blade. The suction mass flow was quantified in terms of the $(\delta^*_{suct}/\delta^*_1)$ ratio which is an intrinsic measure of the effectiveness of suction in decreasing the boundary layer displacement and momentum thicknesses at the slot. The suction coefficient depends on the state of the boundary layer upstream of the slot and the blade solidity for a fixed $(\delta^*_{suct}/\delta^*_1)$ ratio. The effectiveness of suction was shown to diminish with increasing suction mass flow. The different magnification of the momentum thickness change for well attached and close to separation conditions show that not only the suction mass flow but also the location of the suction slot is very critical for effectively controlling the boundary layer.

8.3 Design System and Methodology

The through-flow code MTFLOW combines the features of an axisymmetric Euler solver with the flexibility of a streamline grid resulting in a far superior method of calculating through-flow solutions than the traditional streamline curvature method. The drawback of the MTFLOW streamline approach is that redesign of an existing blade geometry is cumbersome since there is no clear approach to prescribing parameter distributions which are locked to the streamlines in the design phase but depend on the geometry during subsequent redesign iterations. Also, updating the intersection of the streamlines with the blade geometry is computationally expensive. The fixed grid through-flow solver on the

other hand had the advantage of calculating the swirl using the blade camber line, and was used to augment the MTFLOW calculations.

The cascade plane code MISES provided the means to analyze and design the blade sections along quasi 3-D streamsurfaces. The streamline grid coupled with an integral boundary layer formulation and solved implicitly using the Newton method results in unsurpassed computational speed and solution accuracy. The inverse design features provided unprecedented flexibility in designing the blade shapes. A robust suction model was implemented in the code which allowed rapid changes in suction mass flow and slot location, and also resulted in the integration of the suction calculation with the design procedure.

The 3-D Euler solver FELISA was successfully modified to calculate inviscid solutions of the low-speed and high-speed stages. The modified from of the Euler equations, where relative solid body rotation has been subtracted, are more suitable for numerical implementation. The artificial viscosity and wall boundary conditions have to be suitably modified consistent with the modified form of the Euler equations. The tetrahedral grid provided accurate representation of the blade geometry, and the finite element scheme stabilized with matrix dissipation resulted in crisp shock capturing and high overall solution accuracy.

The design procedure to build the three-dimensional blade consisted of loosely coupled iterations between MTFLOW and MISES. Streamsurface and flow conditions from MTFLOW were used as inputs to the MISES blade section calculations, and blockage and losses from MISES were supplied to the MTFLOW through-flow calculation. The advantage of this approach is its simplicity and low computational cost which results in a very quick convergence to the initial design.

However, as the design is refined the quality of the flow conditions input into MISES becomes more critical, and there are two main issues which are seen as limitations of this approach. One is the reliable prediction of blockage especially for supersonic blade rows where the design iterations are sensitive to changes in AVDR. With the reasonable prediction of blockage the flow conditions away from the endwalls were better predicted, however this was found to be insufficient to obtain reliable flow conditions for designing

the blade section affected by the endwall boundary layers and secondary flow features. One approach is to model the effects of the endwall boundary layers and also include spanwise mixing as suggested by Howard and Gallimore [22], and the other is to acquire these directly from the averaging of the 3-D dimensional solution as used by Adamczyk for modeling multi-stage flows [2]. The latter however defeats the purpose of using a through-flow code as part of a computationally inexpensive design system. The second issue is the loss of geometric information between MTFLOW and MISES and is reflected in the uncertainty involved in stacking the blade sections to form the 3-D geometry. The only geometric input to MTLFOW is the axial extent of the blade row required to prescribe the work, loss, and blockage distributions. Information about the axial location of the blade sections is lost once the streamlines are extracted from MTFLOW, and it is difficult to maintain an error free stacking from one design iteration to the next. Blade stacking has an impact on the 3-D features mainly the spanwise shock structure.

The information from the 3-D calculations was outside the primary design iteration loop, and ideally this information should be coupled into the design process as the blade geometry is refined. Coupling a 3-D code with a quasi 3-D solver presents an efficient approach to combining the computational speed and inverse design flexibility of the quasi 3-D with the more accurate flow modeling of the 3-D solver. The coupling can be introduced through flow field sensitivities and geometry parameterization along streamsurfaces. The streamsurface concept should be retained since it is the most intuitive and physically meaningful two dimensional plane for carrying out inverse design.

8.4 Blade Design

The blade loading management design approach applied in this thesis integrates the concept of shock management, dominant in the design of supersonic blades, with boundary layer management dominant in low-speed high turning blades. This integration is an essential ingredient of the aspirated blade design which uses both deceleration through the passage shock as well as subsonic turning to various degrees in different flow regimes. The

blade loading levels achieved by combining aspiration with the new blade design method have not been matched by any other performance enhancement technology such as splitter vanes, tandem and slotted blades, and vortex generators.

Important design features of the aspirated blades are: (1) blended leading edges to prevent pressure spikes, (2) external shock precompression to lower the passage shock strength, (3) concave pressure recovery to obtain maximum subsonic turning, (4) diverging trailing edge to increase blade loading near the trailing edge, and (5) a well designed pressure surface to reduce boundary layer growth on the pressure side. In addition, greater overall blade thickness is maintained to accommodate suction channels and safely meet structural requirements. A unique feature of the aspirated blades is a clear subsonic diffusion and high turning region downstream of the suction slot regardless of the flow regime. In the supersonic aspirated blades this results in a shock structure restricted to the forward portion of the blade in contrast to conventional supersonic blades where the passage shock is located closer to the trailing edge.

The design requirements listed above cannot be accomplished by simple camber line manipulation with a fixed thickness distribution which is suitable for relatively thin supersonic blades. The thicker aspirated blades require a flexible surface parameterization and ability to modify suction and pressure surfaces individually by an optimization method or interactive inverse design method embodied in the MISES code.

8.5 Low-Speed Stage

The low-speed stage has successfully demonstrated the feasibility of significantly lowering the tip speed compared to a conventional stage while maintaining the same pressure ratio. The flow features in the quasi 3-D calculations were in good agreement with the 3-D inviscid and viscous calculations, except in the endwall regions. The design pressure ratio, isentropic efficiency, and suction mass flow requirement predicted by the quasi 3-D calculation also agreed well with the 3-D viscous calculation. The design proved to be robust in the sense that differences in the slot location up to 5% chord and geometry alterations

near the leading and trailing edges in the 3-D viscous calculation did not affect the stage pressure rise or isentropic efficiency noticeably. The design speed line generated by the 3-D viscous calculation showed that the response of the stage to flow variations is similar to that observed in conventional stages.

8.6 High-Speed Stage

The high-speed stage has demonstrated the feasibility of increasing the blade loading by a factor of two at supersonic tip speeds despite the strong shocks. The quasi 3-D rotor calculation was in good overall agreement with the 3-D inviscid and viscous calculations except in the endwall regions. The design rotor pressure ratio, isentropic efficiency, and suction mass flow requirement predicted by the quasi 3-D calculation also agreed well with the 3-D viscous calculation. The 3-D viscous calculation showed that a mismatch between the prescribed slot location and the location in the viscous calculation has an affect on the rotor performance. This location should be better matched in future calculations. The large static pressure rise and strong shock impingement on the tip shroud results in a rapid growth of the endwall boundary layer despite the use of suction and has a significant impact on the pressure ratio near the tip. The use of suction and shaping of the tip profile needs to be studied further to effectively manage the tip endwall boundary layer. The tip clearance effects were eliminated by the use of a rotating shroud. However, the rotating shroud combined with the high tip stagger angle and high blade speed introduced large tangential velocity gradients in the tip region. This resulted in a lowering of the isentropic efficiency in the tip region and also increased the turning requirement of the stator tip section. Three-dimensional viscous calculations of the rotor along the design speed line showed an acceptable range in inlet mass flow between choke and stall, and high pressure ratios and isentropic efficiencies were maintained up to stall.

A preliminary stator design has been completed at the quasi 3-D level. This needs to be incorporated into a 3-D viscous stage calculation to examine the behavior of the stage as a whole.

Bibliography

[1] J.J. Adamczyk. Model equation for simulating flows in multistage turbomachines. ASME 85-GT-226, 1985.

[2] J.J. Adamczyk, M.L. Celestina, and R.A. Mulac. A model for closing the inviscid form of the average-passage equation system. *Journal of Turbomachinery*, 108:180–186, October 1986.

[3] M.L. Celestina. *Segmented Domain Decomposition Multigrid for 3-D Turbomachinery Flows*. PhD thesis, University of Cincinatti, 1999.

[4] J.W.R. Creagh and J.F. Klapproth. Utilization of external-compression diffusion principle in design of shock-in-rotor supersonic compressor blading. research memorandum NACA-RM-E53F18, NACA, 1953.

[5] N.A. Cumpsty. *Compressor Aerodynamics*. Longman, England, 1989.

[6] S.V. Damle. Throughflow method for turbomachines using Euler solvers. AIAA 96-0010, 1996.

[7] M. Drela. XFOIL: An analysis and design system for low Reynolds number airfoils. In T.J. Mueller, editor, *Low Reynolds Number Aerodynamics*. Springer-Verlag, Jun 1989. Lecture Notes in Engineering, No. 54.

[8] M. Drela. An integral boundary layer formulation for blunt trailing edges. AIAA-89-2200, August 1989.

[9] M. Drela. Personal communication, May 1999.

[10] M. Drela and M.B. Giles. Viscous-inviscid analysis of transonic and low Reynolds number airfoils. *AIAA Journal*, 25(10):1347–1355, Oct 1987.

[11] M. Drela and M.A. Schafer. Experimental and computational investigation of divergent trailing edges. Report CFDL-TR-91-1, MIT CFD Laboratory, Jan 1991.

[12] M.B. Giles. Non-reflecting boundary conditions for the Euler equations. Technical Report CFDL TR-88-1, MIT, 1988.

[13] J.P. Gostelow. *Cascade Aerodynamics*. Pergamon Press, Oxford, 1984.

[14] E.M. Greitzer. REVIEW-Axial compressor stall phenomena. *Journal of Fluids Engineering*, 102:134–151, June 1980.

[15] Schreiber H.A. and H. Starken. Experimental investigation of a transonic compressor rotor blade section. *Journal of Engineering for Gas Turbines and Power*, 106:288–294, April 1984.

[16] P.A. Henne and R.D. Gregg. New airfoil design concept. AIAA-89-2201CP, 1989.

[17] C. Hirsch. *Numerical Computation of Internal and External Flows*, volume II. Wiley, England, 1994.

[18] C.H. Hirsch and R.P. Dring. Through flow models for mass and momentum averaged variables. ASME 87-GT-52, 1987.

[19] D. E. Hobbs and H.D. Weingold. Development of controlled diffusion aerofoils for multistage compressor applications. *Journal of Engineering for Gas Turbines and Power*, 106:271–278, 1984.

[20] S.F. Hoerner. *Fluid-Dynamic Drag*. Hoerner Fluid Dynamics, Vancouver, WA, 1951.

[21] J.H. Horlock. *Axial Flow Compressors*. Butterworths Publications, London, 1958.

[22] M.A. Howard and S.J. Gallimore. Viscous throughflow modeling for multistage compressor design. *Journal of Turbomachinery*, 115(2):296–304, April 1993.

[23] L. J. Jahnsen and M. J. Hartmann. Investigation of supersonic-compressor rotors designed with external precompression. Research Memorandum NACA-RM-E54G27a, NACA, 1954.

[24] A. Kantrowitz and duP.D. Coleman. Preliminary investigation of supersonic diffusers. Technical Report ACR No.L5D20, NACA, 1945.

[25] J.L. Kerrebrock. The MIT Blowdown Compressor Facility. Technical Report 108, MIT Gas Turbine Lab., September 1975.

[26] J.L. Kerrebrock. Dryden lecture: Flow in transonic compressors. AIAA 80-0124R, 1980.

[27] J.L. Kerrebrock, M. Drela, A. A. Merchant, and B. J. Schuler. A family of designs for aspirated compressors. ASME Paper 98-GT196, 1998.

[28] J.L. Kerrebrock, D.P. Reijnen, W.S. Ziminsky, and L.M. Smilg. Aspirated compressors. ASME Paper 97-GT525, 1997.

[29] C.C. Koch and L.H. Jr. Smith. Loss sources and magnitudes in axial flow compressors. *Journal of Engineering for Power*, pages 411–424, July 1976.

[30] D. Korn. Numerical design of transonic cascades. Technical Report C00-3077-72, ERDA Research and Development, 1975.

[31] C.H. Law and A.R. Wadia. Low aspect ratio transonic rotors: Part I – Baseline design and performance. *Journal of Turbomachinery*, 115(2):218–225, April 1993.

[32] S. Leiblein, F.C. Schwenk, and F.L. Broderick. Diffusion factor for estimating losses and limiting blade loadings in axial flow compressor blade elements. Technical Report RME53D01, NACA, 1953.

[33] P. Levine. The two dimensional inflow conditions for a supersonic compressor with curved blades. Technical Report WADC TR 55-387, 1956.

[34] R.J. Loughery, R.A. Horn, and P.C. Tramm. Single-stage experimental evaluation of boundary layer blowing and bleed techniques for high lift stator blades. Contractor Report 54573, NASA, March 1971. 71N18749.

[35] A.A. Merchant. Design and analysis of supercritical airfoils with boundary layer suction. Master's thesis, MIT, June 1996.

[36] J.F. Nash. A review of research on two-dimensional base flow. Technical report, British ARC, 1963.

[37] R. Neubert. Preliminary 3.5 pressure ratio aspirated fan stage system study. Technical report, Pratt & Whitney, Hartford, CT, January 1999.

[38] J. Peraire, J. Peiro, and K. Morgan. Finite element multigrid solution of Euler flows past installed aero-engines. *Computational Mechanics*, 11:433–451, 1993.

[39] J. Peraire, J. Peiro, and K. Morgan. Multigrid solution of the 3D compressible Euler equations on unstructured tetrahedral grids. *Int. J. for Num. Meth. in Eng.*, 36:1029–1044, 1993.

[40] K. Pierpont. Investigation of suction-slot shapes for controlling a turbulent boundary layer. Technical Note 1292, NACA, June 1947.

[41] D. P. Reijnen. *Experimental Study of Boundary Layer Suction in a Transonic Compressor*. PhD thesis, MIT, Cambridge, MA, January 1997.

[42] Y. Saad. SPARSKIT: A basic tool kit for sparse matrix computations, user guide and documentation. (unpublished), 1990.

[43] Y. Saad and M.H. Schultz. GMRES: A generalized minimal residual algorithm for solving nonsymmetric linear systems. DCS Report RR-254, Yale University, August 1983.

[44] V. Saxena, W. Lord, and O. Sharma. 3-D aero analysis of the MIT Aspirated Fan. Pratt & Whitney, 1998.

[45] W. Schneider. Aspirated compressors propulsion system study and benefit analysis. Final Report 21-10487, Allied Signal Aerospace, Phoenix, AZ, January 1999.

[46] B.J. Schuler. Mechanical design of an experimental aspirated compressor. Master's thesis, MIT, Cambridge, MA, 1997.

[47] L.M. Smilg. Design of a high pressure ratio fan stage to take advantage of boundary layer suction. Master's thesis, MIT, Cambridge, MA, 1994.

[48] H. Starken. Incidence angle rules in supersonic cascades. In *Transonic Compressors*, volume 1, Von Karman Institute, Brussels, Belgium, February 1988. VKI-LS-1988-03.

[49] H. Starken. Design criteria for optimal blading design. In *Blading Design for Axial Turbomachines*, 1989. AGARD-LS-167.

[50] P. Stow. Blading design for multi-stage hp compressors. In *Blading Design for Axial Turbomachines*, 1989. AGARD-LS-167.

[51] B. Stratford. Flow in the laminar boundary layer near separation. R & M Report 3002, Aeronautical Research Council, HMSO, London, 1954.

[52] J. Syberg and J.L. Kocsek. Bleed system design technology for supersonic inlets. AIAA-72-1138, 1972.

[53] P. C. Tramm and G. D. Huffman. Airfoil design for high tip speed compressors. AIAA-73-1248, 1973.

[54] T.L. Tweedt, H.A. Schreiber, and H. Starken. Experimental investigation of the performance of a supersonic compressor cascade. ASME 88-GT-306, 1988.

[55] K.L. Tzuoo, S.S. Hingorani, and A.K. Sehra. Design methodology for splittered axial compressor rotors. ASME 90-GT-66, 1990.

[56] Y. Wada and M. Liou. A flux splitting scheme with high-resolution and robustness for discontinuities. Technical Memorandum NASA TM-106452, NASA, January 1994.

[57] A.R. Wadia, P.N. Szucs, and D.W. Crall. Inner workings of aerodynamic sweep. *Journal of Turbomachinery*, 120:671–682, October 1998.

[58] A. J. Wennerstrom. Experimental study of a high-throughflow transonic axial compressor stage. *Journal of Engineering for Gas Turbines and Power*, 106:552–559, July 1984.

[59] A. J. Wennerstrom. Some experiments with a supersonic axial compressor stage. *Journal of Turbomachinery*, 109:388–397, 1987.

[60] A. J. Wennerstrom. Transonic and supersonic compressor blading design. In *Blading Design for Axial Turbomachines*, 1989. AGARD-LS-167.

[61] A. J. Wennerstrom. Highly loaded axial flow compressors: History and current development. *Journal of Turbomachinery*, 112:567–578, October 1990.

[62] A. J. Wennerstrom. Design of highly loaded axial-flow fans & compressors. Technical report, WennCo, 1998.

[63] R.E. York and H.S. Woodard. Supersonic compressor cascades-An analysis of the entrance region flow field containing detached shock waves. ASME 75-GT-33, 1975.

[64] H.H. Youngren. Analysis and design of transonic cascades with splitter vanes. Report 203, MIT Gas Turbine Laboratory, Cambridge, MA, 1991.

[65] H.H. Youngren and M. Drela. Viscous/inviscid method for preliminary design of transonic cascades. AIAA-91-2364, 1991.

[66] W.S. Ziminsky. Design of a high pressure ratio transonic compressor stage with active boundary layer control. Master's thesis, MIT, Cambridge, MA, 1996.

Appendix A

Stability Analysis

The stable operation of a compression system comprised of a compressor stage operating in a duct with a throttle will depend on the variation of the compressor static pressure rise with mass flow. The stability condition is illustrated in Figure A-1 is expressed as

$$\frac{\partial(P_{exit} - P_{0inl})}{\partial \dot{m}} < 0. \tag{A.1}$$

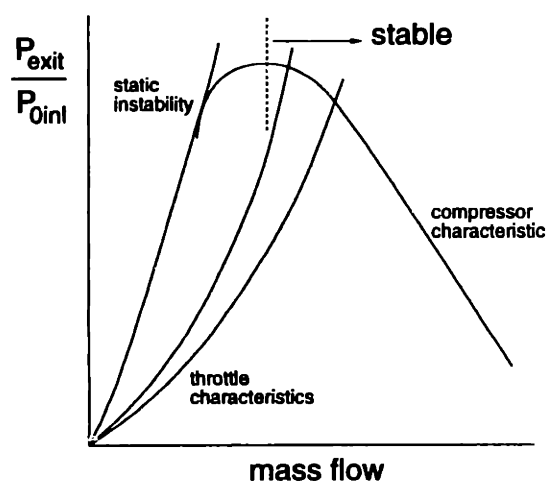

Figure A-1: Compressor and throttle characteristics

When the slope of the static pressure rise characteristic vanishes or becomes positive, small

perturbations in the flow will grow resulting in eventual instability of the flow [5, 14, 21]. The limiting stability is reached when slopes of the compressor and throttle characteristic are tangent, and any further decrease in the mass flow will result in an instability termed static instability. Thus, stable operation is possible only when the static pressure rise characteristic has a negative slope. This is a necessary but not a sufficient condition to establish the stable operation of the stage.

The relatively high blade loading of the aspirated compressor results in a turning of the flow past the axial direction over a large portion of the rotor span. The negative flow angle from the rotor results in a positive slope of total pressure rise with mass flow. This does not imply unstable behavior but raises the question of the effect of negative rotor exit angles on the slope of the static pressure rise characteristic. The stability condition (A.1) is examined first for an isolated rotor and single stage in incompressible flow by deriving equations for the static pressure rise. Next, the effect of compressibility on the stability condition is examined by deriving the compressible form of the pressure rise equation. In the following analysis, zero swirl at the stage inlet and exit is assumed in order to simplify the equations and interpretation of the results relevant to this thesis.

A.1 Incompressible Analysis

A.1.1 Isolated Rotor

Referring to Figure 2-1, the total pressure rise for an incompressible flow through a rotor is given by

$$\Delta p_0 = \rho U_b V_{\theta 2} \left(\frac{r_2}{r_1}\right) \tag{A.2}$$

where the inlet flow has no swirl and may undergo a radius change through the rotor. The static pressure downstream of the rotor can be related to the total pressure via Bernoulli's equation. Substituting the static pressure in equation (A.2) and simplifying gives

$$\frac{p_2 - p_{01}}{\rho U_b^2} = \left(\frac{r_2}{r_1}\right)\left(\frac{V_{\theta 2}}{U_b}\right) - \frac{1}{2}\left(\left(\frac{V_{x2}}{U_b}\right)^2 + \left(\frac{V_{\theta 2}}{U_b}\right)^2\right) \tag{A.3}$$

The tangential velocity can be expressed in terms of the exit flow angle and the axial velocity in terms of the flow coefficient to give

$$\begin{aligned} \frac{V_{\theta 2}}{U_b} &= 1 - \mathrm{AVR}_{\mathrm{rot}}\phi \tan\beta_2 \\ \frac{V_{x2}}{U_b} &= \mathrm{AVR}_{\mathrm{rot}}\phi \end{aligned} \tag{A.4}$$

where $\mathrm{AVR}_{\mathrm{rot}}$ is V_{x2}/V_{x1}, the flow coefficient ϕ is V_{x1}/U_b, β_2 is the rotor relative exit angle. Substituting these relationships in equation (A.3) gives

$$\frac{p_2 - p_{01}}{\rho U_b^2} = \left(\frac{r_2}{r_1} - \frac{1}{2}\right) + \frac{\phi}{\mathrm{AVR}_{\mathrm{rot}}}\left[\tan\beta_2\left(1 - \frac{r_2}{r_1}\right) - \frac{1}{2}\frac{\phi}{\mathrm{AVR}_{\mathrm{rot}}}(1 + \tan^2\beta_2)\right]. \tag{A.5}$$

The stability condition is obtained by differentiating equation (A.5) with respect to ϕ:

$$\frac{\partial}{\partial\phi}\left(\frac{p_2 - p_{01}}{\rho U_b^2}\right) = \left[\tan\beta_2\left(1 - \frac{r_2}{r_1}\right) - \frac{\phi}{\mathrm{AVR}_{\mathrm{rot}}}(1 + \tan^2\beta_2)\right]\frac{1}{\mathrm{AVR}_{\mathrm{rot}}} < 0. \tag{A.6}$$

The above equation is always less than zero indicating unconditional stability of an isolated rotor for any exit angle.

A.1.2 Stage

Equation (A.5) can be extended to a complete stage by applying Bernoulli's equation across the stator, assuming an ideal flow and zero swirl at the exit, to obtain an expression for the static pressure p_3 at the stator exit.

$$\frac{p_3 - p_2}{\rho U_b^2} = \frac{1}{2}\left[\left(\frac{V_{x2}}{U_b}\right)^2 + \left(\frac{V_{\theta 2}}{U_b}\right)^2 - \left(\frac{V_{x3}}{U_b}\right)^2\right] \tag{A.7}$$

The rotor exit conditions from equation (A.3) can be substituted in the above equation to relate the stator exit pressure p_3 with the inlet conditions

$$\frac{p_3 - p_{01}}{\rho U_b^2} = \left(\frac{r_2}{r_1}\right)\left(\frac{V_{\theta 2}}{U_b}\right) - \frac{1}{2}\left(\frac{V_{x3}}{U_b}\right)^2. \tag{A.8}$$

Finally, $V_{\theta 2}$ can be replaced with the flow angle relation and V_{x3} can be related to V_{x1} via axial velocity ratios to give

$$\frac{p_3 - p_{01}}{\rho U_b^2} = \left(\frac{r_2}{r_1}\right)(1 - \mathrm{AVR_{rot}}\phi \tan\beta_2) - \frac{1}{2}(\mathrm{AVR_{rot}}\mathrm{AVR_{sta}}\phi)^2 \,. \tag{A.9}$$

The stability condition is obtained by differentiating equation (A.9) with respect to ϕ giving

$$\frac{\partial}{\partial\phi}\left(\frac{p_3 - p_{01}}{\rho U_b^2}\right) = -\left(\frac{r_2}{r_1}\right)\mathrm{AVR_{rot}}\tan\beta_2 - \phi(\mathrm{AVR_{rot}}\mathrm{AVR_{sta}})^2 < 0 \tag{A.10}$$

$$\Rightarrow \tan\beta_2 > -\phi\,\mathrm{AVR_{rot}}\mathrm{AVR_{sta}}^2\left(\frac{r_2}{r_1}\right) .$$

Thus, the exit angle is limited by the inlet flow coefficient and further by the ramp angle across the rotor. The radius change across the stator also effects the limiting condition indirectly through the axial velocity ratio across the stator.

The limiting condition on the flow angle can be explained by examining the contribution of the swirl input and axial velocity in equation (A.8) to the static pressure rise across the stage. The static pressure rise due to the swirl input will increase with mass flow for negative flow angles. The contribution from axial velocity term on the other hand will always decrease the static pressure with increase in mass flow. If the pressure rise from the swirl contribution is larger than decrease due to the axial velocity, the static pressure will increase with increasing mass flow resulting in a positive slope of the pressure rise characteristic and violation of the stability condition.

A.2 Compressible Analysis

A.2.1 Isolated Rotor

The total enthalpy rise along a rotor streamsurface with adiabatic flow is given by the Euler equation

$$\Delta H = U_b V_{\theta 2}\left(\frac{r_2}{r_1}\right) \tag{A.11}$$

where the inlet flow has no swirl and may undergo a radius change across the rotor. Using the definition of total enthalpy and isentropic relations the above equation can be written as

$$\left(\frac{a_2}{a_{01}}\right)^2 = 1 + (\gamma - 1)M_{b0}^2\left[\left(\frac{r_2}{r_1}\right)\left(\frac{V_{\theta 2}}{U_b}\right) - \frac{1}{2}\left(\frac{V_{x2}^2}{U_b^2} + \frac{V_{\theta 2}^2}{U_b^2}\right)\right] \tag{A.12}$$

where a_2 is the local sonic velocity, a_{01} is the rotor inlet stagnation sonic velocity, and M_{b0} is the blade Mach number based on a_{01}. The term multiplying M_{b0}^2 is simply the incompressible pressure rise equation (A.5) which can be substituted in the above equation to give

$$\left(\frac{a_2}{a_{01}}\right)^2 = 1 + (\gamma - 1)M_{b0}^2\,\psi_{R\text{inc}}\,. \tag{A.13}$$

$$\text{where} \qquad \psi_{R\text{inc}} = \frac{p_2 - p_{01}}{\rho U_b^2}$$

is used for convenience. Continuity across the rotor combined with isentropic relations can be used to express the left hand side of equation (A.13) in terms of the pressure rise giving

$$\left(\frac{a_2}{a_{01}}\right)^2 = \text{AVR}_{\text{rot}}\left(\frac{A_2}{A_1}\right)\left(\frac{p_2}{p_{01}}\right)\left(\frac{T_{01}}{T_1}\right)^{\frac{1}{\gamma-1}} \tag{A.14}$$

where (A_2/A_1) is the area ratio across the rotor. Finally, combining equations (A.13) and (A.14) the ratio of exit static pressure to inlet total pressure for the rotor can be written as

$$\left(\frac{p_2}{p_{01}}\right) = \frac{1}{\text{AVR}_{\text{rot}}}\left(\frac{A_1}{A_2}\right)\left(1 + (\gamma - 1)M_{b0}^2\psi_{\text{inc}}\right)\left(1 - \frac{(\gamma - 1)}{2}M_{b0}^2\phi^2\right)^{\frac{1}{\gamma-1}}. \tag{A.15}$$

Differentiating the above equation with respect to ϕ gives

$$\begin{aligned}\frac{\partial}{\partial\phi}\left(\frac{p_2}{p_{01}}\right) &= \frac{1}{\text{AVR}_{\text{rot}}}\left(\frac{A_1}{A_2}\right)M_{b0}^2\left(1 - \frac{(\gamma-1)}{2}M_{b0}^2\phi^2\right)^{\frac{1}{\gamma-1}}\left[(\gamma-1)\frac{\partial\psi_{\text{inc}}}{\partial\phi}\right. \\ &- \left.\phi\left(1 + (\gamma-1)M_{b0}^2\psi_{\text{inc}}\right)\left(1 - \frac{(\gamma-1)}{2}M_{b0}^2\phi^2\right)^{2-\gamma}\right].\end{aligned} \tag{A.16}$$

This fairly complicated result shows that the isolated rotor is unconditionally stable even with compressibility effects. The first term outside the square brackets is always positive

whereas the terms inside the brackets are always negative resulting in a negative slope of the pressure rise characteristic for any exit flow angle.

A.2.2 Stage

The stagnation temperature being constant through the stator, the temperature ratio across the stator in terms of the local sonic velocities is given by

$$\left(\frac{a_3}{a_2}\right)^2 = 1 + \frac{(\gamma - 1)}{2} M_{b0}^2 \left(\frac{a_{01}}{a_2}\right)^2 \left[\left(\frac{V_{x2}}{U_b}\right)^2 + \left(\frac{V_{\theta 2}}{U_b}\right)^2 - \left(\frac{V_{x3}}{U_b}\right)^2\right] \tag{A.17}$$

where zero swirl at the stator exit is assumed. Substituting equation (A.12) in the above equation and simplifying gives

$$\left(\frac{a_3}{a_2}\right)^2 = \left(\frac{a_{01}}{a_2}\right)^2 \left[1 + (\gamma - 1) M_{b0}^2 \left(\left(\frac{r_2}{r_1}\right)\left(\frac{V_{\theta 2}}{U_b}\right) - \frac{1}{2}\left(\frac{V_{x3}}{U_b}\right)^2\right)\right]. \tag{A.18}$$

The term multiplying M_{b0} is the incompressible pressure rise equation (A.8). Continuity across the stator combined with isentropic relations can be used to relate the sonic velocity ratio to the static pressure ratio

$$\left(\frac{a_3}{a_2}\right)^2 = \mathrm{AVR_{sta}} \left(\frac{A_3}{A_2}\right)\left(\frac{p_3}{p_2}\right) \tag{A.19}$$

where (A_3/A_2) is the area ratio across the stator. The pressure rise across the stator can be written in terms of the incompressible pressure rise across the rotor given by equation (A.13) and stage given by equation (A.8).

$$\left(\frac{p_3}{p_2}\right) = \frac{1}{\mathrm{AVR_{sta}}} \left(\frac{A_2}{A_3}\right)\left(1 + (\gamma - 1) M_{b0}^2 \, \psi_{Rinc}\right)\left(1 + (\gamma - 1) M_{b0}^2 \, \psi_{Sinc}\right) \tag{A.20}$$

where

$$\begin{aligned} \psi_{Rinc} &= \frac{p_2 - p_{01}}{\rho U_b^2} \\ \psi_{Sinc} &= \frac{p_3 - p_{01}}{\rho U_b^2} \end{aligned} \tag{A.21}$$

are used to simplify the notation. The ratio of the static pressure at the exit to the inlet total pressure can be obtained via

$$\left(\frac{p_3}{p_{01}}\right) = \left(\frac{p_3}{p_2}\right)\left(\frac{p_2}{p_{01}}\right) \tag{A.22}$$

where p_2/p_{01} is given by equation (A.15). The stability condition can be derived by differentiating the above relation with respect to ϕ giving

$$\frac{\partial}{\partial\phi}\left(\frac{p_3}{p_{01}}\right) = \left(\frac{p_3}{p_2}\right)\frac{\partial}{\partial\phi}\left(\frac{p_2}{p_{01}}\right) + \left(\frac{p_2}{p_{01}}\right)\frac{\partial}{\partial\phi}\left(\frac{p_3}{p_2}\right) < 0 \tag{A.23}$$

where

$$\begin{aligned}\frac{\partial}{\partial\phi}\left(\frac{p_3}{p_2}\right) &= \frac{1}{\mathrm{AVR_{sta}}}\left(\frac{A_2}{A_3}\right)\left[\left(1+(\gamma-1)M_{b0}^2\,\psi_{Rinc}\right)\frac{\partial\psi_{Sinc}}{\partial\phi}\right. \\ &+ \left.\left(1+(\gamma-1)M_{b0}^2\,\psi_{Sinc}\right)\frac{\partial\psi_{Rinc}}{\partial\phi}\right].\end{aligned} \tag{A.24}$$

The compressible stability condition derived above cannot be simplified any further and a numerical approach must be used to test if a stage satisfies the stability condition. However, the various terms in equation (A.23) can be examined to obtain a qualitative understanding of the effect of compressibility on the stability condition. The first term in equation is always negative since $p_3/p_2 > 0$ and $\partial(p_2/p_{01})/\partial\phi < 0$ due to unconditional stability of the rotor. The first term will be especially large if the flow is turned past the axial direction since most of the pressure rise will occur across the stator which suggests that compressibility enhances stability. The second term, however, could be positive since $\partial(p_3/p_2)/\partial\phi$ depends on the sign of $\partial\psi_{Sinc}/\partial\phi$ which may be positive as shown earlier . The overall conclusion that can be drawn from the compressible analysis is that compressibility relaxes the condition on stability imposed by the incompressible case, and satisfying the incompressible stability condition will ensure stability in the compressible case.